Search for the SM Higgs Boson in the Channel WH $\rightarrow l\nu b\bar{b}$ with the ATLAS Experiment at the LHC

Dissertation der Fakultät für Physik
der
Ludwig-Maximilians-Universität München

vorgelegt von
Jonas Zacharias Will
geboren in München

München, den 11.10.2012

Erstgutachterin:	Prof. Dr. Dorothee Schaile
Zweitgutachter:	Prof. Dr. Wolfgang Dünnweber

Tag der mündlichen Prüfung: 26.11.2012

Thanks, nature!

Fabiola Gianotti, 4.7.2012

Zusammenfassung

Eine der größten wissenschaftlichen Herausforderungen von ATLAS und CMS, Universaldetektoren am Large Hadron Collider (LHC) des Forschungszentrums CERN, ist der Nachweis oder Ausschluss des seit fast fünfzig Jahren vorhergesagten Standardmodell-Higgs-Bosons. Im Sommer diesen Jahres wurde sowohl von ATLAS als auch von CMS ein neues Teilchen entdeckt. Die von ATLAS bestimmte Masse dieses Teilchens liegt bei 126.0 ± 0.4 (stat) $\pm$ 0.4 (sys) GeV, die von CMS bestimmte bei 125.3 ± 0.4 (stat) $\pm$ 0.5 (sys) GeV [1, 2]. Die weiteren bisher bekannten Eigenschaften dieses Teilchens sind konsistent mit den vorhergesagten Eigenschaften eines Standardmodell-Higgs-Bosons innerhalb von großen Fehlergrenzen. Neben den sensitiven, bosonischen Zerfallskanälen des Higgs, $H \to \gamma\gamma$, $H \to ZZ$ und $H \to WW$, haben auch die fermionischen Kanäle $H \to \tau\tau$ und $H \to b\bar{b}$ zu den statistischen Ausschlussgrenzen eines Higgs-Bosons mit einer Masse unterhalb des beobachteten Überschusses beigetragen. Darüber hinaus sind diese Zerfallskanäle notwendig, um die Kopplungen des neu entdeckten Teilchens an Fermionen zu messen.

In der vorliegenden Analyse wird die assoziierte Higgs Produktion WH in Kombination mit dem Higgs-Zerfallskanal $H \to b\bar{b}$ studiert. Sie basiert auf einer integrierten Luminosität von 4.7 fb^{-1}, die ATLAS im Jahr 2011 bei einer Schwerpunktsenergie von 7 TeV gesammelt hat. Eine Schnitt-basierte Analyse wählt die Ereignisse mit folgender Signatur aus: Sie umfasst ein Lepton (Elektron oder Myon), fehlende transversale Energie und zwei b-Jets. Methoden zur Daten-gestützten Abschätzung des QCD-Untergrundes werden entwickelt, getestet und angewandt. Die unterschiedlichen Beiträge des W+jets Untergrundes, charakterisiert durch Jets aus b- oder c-Quarks, oder leichten Quarks/Gluonen, werden mit einer Daten-gestützten Methode abgeschätzt. Zudem werden die wichtigsten Komponenten des Untergrundes, der top und W+jets Untergrund, mit Hilfe von Kollisions-Daten normiert. Die invariante Masse der ausgewählten Jets $m_{b\bar{b}}$ wird für die Bestimmung von Ausschlussgrenzen auf die Higgs-Signalstärke σ/σ_{WH} verwendet. Dabei wird der Bereich 110 GeV $\leq m_H \leq$ 130 GeV der Higgs-Masse betrachtet. Für eine hypo-

thetische Higgs-Masse von 110 GeV kann die Signalstärke für alle Werte oberhalb von 4,8 auf einem Confidence Level von 95 % ausgeschlossen werden.

Abstract

One of the most important scientific challenges of ATLAS and CMS, multi-purpose detectors at CERN's Large Hadron Collider (LHC), is the discovery or exclusion of the longly sought standard model Higgs boson predicted almost fifty years ago. In summer 2012, both ATLAS and CMS discovered a new particle. Its mass is determined to be 126.0 ± 0.4 (stat) $\pm$ 0.4 (sys) GeV (ATLAS) and 125.3 ± 0.4 (stat) $\pm$ 0.5 (sys) GeV (CMS) [1, 2]. Its further properties are so far consistent with the predicted properties of a standard model Higgs boson within large uncertainties. Besides the Higgs search in the sensitive bosonic channels, $H \to \gamma\gamma$, $H \to ZZ$, and $H \to WW$, the fermionic channels $H \to \tau\tau$ and $H \to b\bar{b}$ contributed to the exclusion of a standard model Higgs boson below the observed excess and are essential for measuring the couplings of the new particle to fermions.

In the analysis presented here, the associated Higgs production WH in the Higgs decay channel $H \to b\bar{b}$ is studied on the collision data corresponding to an integrated luminosity of 4.7 fb^{-1} recorded by ATLAS in 2011 at a proton-proton centre-of-mass energy of 7 TeV. A cut-based analysis selects events with the signature of interest, consisting of one lepton (electron, muon), missing transverse energy, and two b jets. Techniques for a data-driven estimate of the multijet background are developed, validated and applied. The different contributions from heavy and light flavour jets to the W+jets background are estimated by a data-driven method. Furthermore, the large background components from top and W+jets are normalized using collision data. The invariant mass of the two selected jets $m_{b\bar{b}}$ is used for the determination of exclusion limits on the Higgs signal strength σ/σ_{WH} in the mass window 110 GeV $\leq m_H \leq$ 130 GeV. For a hypothesized Higgs mass of $m_H = 110$ GeV, the Higgs signal strength is excluded for values larger than 4.8 at a confidence level of 95 %.

Contents

1. Introduction

Since the 1970s, the standard model of particle physics (SM), described in the following Section 1.1, has evolved to the state of the art for the description of fundamental particles and their interactions. Its predictive power was successfully tested by measurements with a precision of at least $\mathcal{O}(10^{-3})$. One open question inside the SM is the mechanism that gives mass to the elementary particles. The so-called Higgs mechanism, developed by F. Englert, R. Brout, P. W. Higgs, G. S. Guralnik, C. R. Hagen, and T. W. B. Kibble, is the favoured model based on the concept of spontaneous symmetry breaking [3–5]. It is outlined in Section 1.2. In the minimal version, the Higgs mechanism predicts the existence of one scalar boson, the Higgs boson. The search for the Higgs boson together with the discovery of a Higgs-like particle at the LHC experiments ATLAS and CMS is presented in the Sections 1.3 and 1.4. Section 1.5 is finally devoted to the Higgs search in the channel $WH \to l\nu b\bar{b}$.

1.1. The Standard Model of Particle Physics

The standard model of particle physics is a consistent, renormalizable quantum field theory. It describes the interactions of the fundamental fermions which are the constituents of all ordinary matter. In this theory, forces between the fermions are transmitted by interaction particles, which obey the Bose-Einstein statistics. The elementary SM fermions comprise six quarks and six leptons, each falling into three generations with increasing mass, and their antiparticles [6].

Four fundamental interactions exist: the gravitation, the electromagnetism, the weak force and the strong force. The SM does not incorporate the gravitation due to its weakness compared to the other forces. Besides, there is no quantum theory for gravity yet. Table 1.1 depicts the three generations of fermions and their possible interactions. The forces are

Table 1.1.: The three generations of fundamental fermions of the SM and their interactions ("e.m." stands for electromagnetic). "+" ("−") symbolizes that the corresponding interaction does (not) exists for the considered fermion.

	quarks	e.m.	weak	strong	leptons	e.m.	weak	strong
1^{st}	u (up)	+	+	+	e^- (electron)	+	+	−
	d (down)	+	+	+	ν_e (electron neutrino)	−	+	−
2^{nd}	c (charm)	+	+	+	μ^- (muon)	+	+	−
	s (strange)	+	+	+	ν_μ (muon neutrino)	−	+	−
3^{rd}	t (top)	+	+	+	τ^- (tau)	+	+	−
	b (bottom)	+	+	+	ν_τ (tau neutrino)	−	+	−

described by two quantum field theories: the electroweak theory (EW) for electromagnetic and weak interactions, and quantum chromodynamics (QCD) for strong interactions. These quantum field theories are based on a common principle: to describe interactions between particles, the basic equations are required to be invariant under local gauge transformations, thereby introducing local symmetries in the theory. The SM is based on the following gauge symmetry: $U(1)_Y \otimes SU(2)_L \otimes SU(3)$, where $U(1)_Y \otimes SU(2)_L$ represents the symmetry group of the electroweak theory, and $SU(3)$, the symmetry group of QCD. Consequences of the symmetry are the emergence of spin-1 gauge bosons, the quantized mediators of the considered interaction, and the appearance of a conserved charge. The electromagnetic interactions are mediated by the (massless) photon γ, whereas the weak interactions are mediated by the (massive) $W^\pm$, and Z bosons. Strong interactions are mediated by eight (massless) gluons g. The corresponding charges are the electromagnetic charge Q (electromagentic interactions), the weak isospin T (weak interactions), and the colour charge C (strong interactions). Only particles carrying a particular charge can participate in the corresponding interaction. Due to the non-abelian symmetry of the weak and strong interactions, self couplings between γ, $W^\pm$, and Z, and between the gluons g occur. In contrast to electromagnetic and strong interactions, weak interactions violate parity: The weak gauge bosons $W^\pm$ couple merely to left-handed particles (right-handed anti-particles) and violate the parity maximally. This is indicated by the subscript L in the EW gauge group $U(1)_Y \otimes SU(2)_L$. The Z boson violates the parity partially and couples stronger to left-handed than to right-handed particles.The subscript Y in the electroweak symmetry group symbolizes the hypercharge Y and includes the electromagnetic charge Q. The introduction of Y is necessary to unify the electromagnetic and weak interactions. On the basis of the Langrange formalism in classical mechanics [7], the dynamics of elementary particles is described by a Lagrangian $\mathcal{L}(\Phi, \frac{\partial \Phi}{\partial x_\mu}, x_\mu)$ and the derived Euler-

Lagrange equation:

$$\frac{\partial}{\partial x_\mu}\Big(\frac{\partial \mathcal{L}}{\partial(\partial\Phi/\partial x_\mu)}\Big) - \frac{\partial \mathcal{L}}{\partial \Phi} = 0, \tag{1.1}$$

where Φ describes the considered field and x_μ the space-time four vector.
The Lagrangian $\mathcal{L}$ of the SM can be described by:

$$\mathcal{L}_{SM} = \mathcal{L}_{EW} + \mathcal{L}_{QCD}, \tag{1.2}$$

with

$$\mathcal{L}_{EW} = \overbrace{\overline{L} i\gamma^\mu D_\mu L + \overline{e}_R i\gamma^\mu D_\mu e_R}^{\mathcal{L}_{EW,F+FB}} - \overbrace{\frac{1}{4}B_{\mu\nu}B^{\mu\nu} - \frac{1}{4}\vec{W}_{\mu\nu}\vec{W}^{\mu\nu}}^{\mathcal{L}_{EW,B}}, \tag{1.3}$$

and

$$\mathcal{L}_{QCD} = \overbrace{\overline{\Psi} i\gamma^\mu D_\mu \Psi}^{\mathcal{L}_{QCD,F+FB}} - \overbrace{\frac{1}{4}\vec{G}_{\mu\nu}\vec{G}^{\mu\nu}}^{\mathcal{L}_{QCD,B}}. \tag{1.4}$$

The Langrangian $\mathcal{L}_{EW}$ and $\mathcal{L}_{QCD}$ denote the Lagrangian for the electroweak and strong interactions, respectively. L (e_R) describes a left-handed isospin doublet (right-handed isospin singlet) of fermions. $B_{\mu\nu}$ and $\vec{W}^{\mu\nu}$ denote the fields of the electroweak gauge bosons. They mix to the observable fields of γ, $W^\pm$, and Z boson. Ψ describes strongly interacting fermions and $\vec{G}^{\mu\nu}$ the gluons g. The subscripts F and B symbolize the free fermion and free boson terms of the Lagrangians, whereas $_{FB}$ describes the interaction term between fermions and bosons. The terms $\mathcal{L}_{EW,F+FB}$ and $\mathcal{L}_{QCD,F+FB}$ contain the covariant derivative D_μ, that describes the free fermion fields as well as the coupling between fermions and bosons in a manner that sustains the gauge invariance of the Lagrangian. γ^μ denote the Dirac matrices.
Unfortunately, the introduction of particle masses by a direct mass term destroys the gauge invariance of $\mathcal{L}$. Therefore, the Equations 1.3 and 1.4 ignore particles masses. The most popular approach to introduce mass but sustain the gauge invariance is the Higgs mechanism outlined in the next section.
In contrast to leptons, no free quarks (or gluons) have been observed up to now. They are confined in colourless hadrons, which are bound states of two (mesons) or three (baryons) quarks. As the strength of strong interactions increases with increasing distance between the interacting partners, no perturbation theory can be applied to this problem [6]. Therefore, one relies on models describing the hadronization, i.e. the transformation of quarks or gluons into hadrons which are detectable in high-energy particle collisions. The different existing models are based on an asymptotic approach: the high-energetic initial quark q_0 emits a pair of quarks $q_1\overline{q}_1$, such that $q_0\overline{q}_1$ builds a meson and q_1 is left. q_1 is later on

included in the meson $q_1\overline{q}_2$ of the produced pair $q_2\overline{q}_2$, and so on. The collimated stream of hadrons in the direction of the initial quark or gluon is called jet. Event generators, such as Pythia, rely on hadronizing models to describe the step between the interaction of fundamental quarks or gluons and the interaction of the produced hadrons with the detector material [8].

1.2. Introduction to the SM Higgs Mechanism

The basic concepts of the Higgs mechanism that induces massive gauge bosons $W^{\pm}$ and Z are outlined in the first section using the example of a $U(1)$ theory. It is followed by the incorporation of the mechanism into the SM. Finally, a model to describe the masses of fermions is presented.

1.2.1. The Higgs Mechanism for a U(1) Theory

The Higgs mechanism introduces a new, complex scalar field Φ with spin 0:

$$\Phi \equiv \Phi_1 + i\Phi_2 \tag{1.5}$$

The Klein-Gordon Lagrangian describes the dynamic of spinless particles with mass m:

$$\mathcal{L}_{Klein-Gordon} = \frac{1}{2}\left(\frac{\partial\Phi}{\partial x_\mu}\right)\left(\frac{\partial\Phi^*}{\partial x^\mu}\right) - \frac{1}{2}m^2\Phi^*\Phi. \tag{1.6}$$

Since a direct mass term destroys the gauge invariance, the new field Φ is described by a modified Klein-Gordon Lagrangian. Instead of the mass term $\frac{1}{2}m^2\Phi^*\Phi$, the "double well" potential $V(\Phi) = -\frac{1}{2}\mu^2(\Phi^*\Phi) + \frac{1}{4}\lambda^2(\Phi^*\Phi)^2$ is introduced. It consist of a second-order parabola with negative curvature and a fourth-order with positive curvature. Therefore, the minimum of $V(\Phi)$ is not located at $|\Phi| = 0$, but lies on a "circle" of radius $|\Phi| = \mu/\lambda$. The parameters μ and λ are free parameters of $V(\Phi)$. It embodies the principle of spontaneous symmetry breaking: The Lagrangian

$$\mathcal{L} = \frac{1}{2}\left(\frac{\partial\Phi}{\partial x_\mu}\right)\left(\frac{\partial\Phi^*}{\partial x^\mu}\right) - V(\Phi) \tag{1.7}$$

is invariant under global ($\Phi \rightarrow \Phi^{e^{i\Theta}}$) $U(1)$ gauge transformations. But for a certain ground state Φ_{min}, that lies somewhere on the circle of possible minima, this symmetry is broken. Since an arbitrary ground state is selected, the symmetry breaking is called "spontaneous". To achieve even local ($\Phi \rightarrow \Phi^{e^{i\Theta(x)}}$) $U(1)$ gauge symmetry a covariant derivative is built that couples a massless gauge field A^μ of spin 1 to the field Φ:

$$D_\mu = \partial_\mu + iqA_\mu \tag{1.8}$$

the notation ∂_μ is a short form of $\frac{\partial}{\partial x_\mu}$. Equation 1.7 now turns into

$$\mathcal{L} = \frac{1}{2}\Big[\Big(\partial_\mu - iqA_\mu\Big)\Phi\Big]\Big[\Big(\partial^\mu + iqA^\mu\Big)\Phi^*\Big] + \frac{1}{2}\mu^2(\Phi^*\Phi) - \frac{1}{4}\lambda^2(\Phi^*\Phi)^2 - \frac{1}{4}F^{\mu\nu}F_{\mu\nu} \tag{1.9}$$

The term $-\frac{1}{4}F^{\mu\nu}F_{\mu\nu}$ describes the free field A^μ.
Rewriting the field Φ under the assumption of fluctuations around the ground state $|\Phi| = \mu/\lambda$

$$\eta \equiv \Phi_1 - \mu/\lambda, \xi \equiv \Phi_2, \tag{1.10}$$

Equation 1.9 turns into:

$$\begin{aligned}
\mathcal{L} = &\Big[\frac{1}{2}(\partial_\mu\eta)(\partial^\mu\eta) - \mu^2\eta^2)\Big] + \Big[\frac{1}{2}(\partial_\mu\xi)(\partial^\mu\xi)\Big] \\
&+\Big[-\frac{1}{4}F^{\mu\nu}F_{\mu\nu} + \frac{1}{2}\Big(q\frac{\mu}{\lambda}\Big)^2 A_\mu A^\mu\Big] \\
&+\Big[q[\eta(\partial\xi) - \xi(\partial\eta)]A^\mu + \frac{\mu}{\lambda}q^2\eta(A_\mu A^\mu) + \frac{1}{2}q^2(\xi^2+\eta^2)(A_\mu A^\mu) \\
&-\lambda\mu(\eta^3 + \eta\xi^2) - \frac{1}{4}\lambda^2(\eta^4 + 2\eta^2\xi^2 + \xi^4)\Big] \\
&+\frac{\mu}{\lambda}q(\partial_\mu\xi)A^\mu + \Big(\frac{\mu^2}{2\lambda}\Big)^2
\end{aligned} \tag{1.11}$$

Equation 1.11 can be interpreted as follows:
The first line of Equation 1.11 corresponds to two Klein-Gordon Lagrangians (see Equation 1.6): the first one describes a spin-0 particle η with a mass $\sqrt{2}\mu$, the second one a massless spin-0 particle ξ.
The second line describes the field A^μ and a mass term that emerged by the interaction with Φ the mass $(q\mu/\lambda)$. This can be seen by comparing the second line with the Proca Langrangian, that describes a massive scalar particle with spin 1:

$$\mathcal{L}_{Proca} = -\frac{1}{4}F^{\mu\nu}F_{\mu\nu} + \frac{m^2}{2}A_\mu A^\mu \tag{1.12}$$

Out of the coupling terms between Φ and A^μ in the gauge invariant Equation 1.9 the mass term of the Proca Langrangian emerged by spontaneous symmetry breaking, i.e. by the constant ground state part μ/λ of η.
The third and fourth line in Equation 1.11 describe couplings of the fields η, ξ, and A^μ. The term $\frac{\mu}{\lambda}q(\partial_\mu\xi)A^\mu$ in the fifth line describes the (unphysical) change of ξ into A^μ. Moreover, a specific gauge transformation can be applied, that removes all terms including the ξ field. One finally gets:

$$\begin{aligned}\mathcal{L} = &\left[\frac{1}{2}(\partial_\mu\eta)(\partial^\mu\eta) - \mu^2\eta^2)\right] + \left[-\frac{1}{4}F^{\mu\nu}F_{\mu\nu} + \frac{1}{2}\left(q\frac{\mu}{\lambda}\right)^2 A_\mu A^\mu\right] \\ &+\left[\frac{\mu}{\lambda}q^2\eta(A_\mu A^\mu) + \frac{1}{2}q^2\eta^2(A_\mu A^\mu) - \lambda\mu\eta^3 - \frac{1}{4}\lambda^2\eta^4\right] + \left(\frac{\mu^2}{2\lambda}\right)^2\end{aligned} \tag{1.13}$$

In summary, by rewriting Equation 1.9 and applying a specific gauge transformation, one ends up with a new massive scalar spin-0 boson η, called the Higgs boson, and a massive gauge boson A^μ. The degree of freedom that was described by the massless boson ξ is now present in the massive gauge boson, that gained together with the mass a transverse polarisation degree of freedom. Equation 1.13 contains furthermore two interaction terms between the Higgs field η and the gauge boson A^μ besides two self-interaction terms of the Higgs field. The last term $(\mu^2/2\lambda)^2$ is a constant and therefore does not have any influence on the dynamics described by the Euler-Lagrange Equations [6].

1.2.2. The Higgs Mechanism in the Standard Model

To introduce masses to the gauge bosons in the electroweak theory, the $U(1)$ Higgs mechanism as outlined in Section 1.2.1 has to be adapted for the EW symmetry group $U(1)_Y \otimes SU(2)_L$. This can be achieved by replacing the complex field Φ (see 1.5) by a weak isospin doublet

$$\mathbf{\Phi} = \begin{pmatrix} \Phi^+ \\ \Phi^0 \end{pmatrix}, \tag{1.14}$$

and by replacing the covariant derivative D_μ in Equation 1.8 by the corresponding one of the EW theory:

$$D_\mu = \partial_\mu + \frac{1}{2}ig'YB_\mu + \frac{1}{2}ig\vec{\tau}\vec{W}_\mu \tag{1.15}$$

The coupling strength g' (g) belongs to the $U(1)_Y$ ($SU(2)_L$) part of the electroweak symmetry. The hypercharge Y is defined via the electromagnetic charge Q and the third component of the weak isospin T_3: $Y = 2(Q - T_3)$. The components of the vector $\vec{\tau}$ are

generators of the symmetry group $SU(2)$.
Inserting one Higgs doublet into the EW theory and requiring local gauge invariance under $U(1) \otimes SU(2)$ (as done in Section 1.2.1 for the $U(1)$ symmetry group), results in the following mass term $\mathcal{L}_{m,gauge}$ for the gauge bosons:

$$\mathcal{L}_{m,gauge} = \frac{1}{2}\left(\frac{\mu}{\lambda}\frac{g}{2}\right)^2 [|W_\mu^+|^2 + |W_\mu^-|^2] + \frac{1}{2}\left(\frac{\mu}{\lambda}\frac{g}{2}\right)^2 \left(\frac{1}{\cos\Theta_w}\right)^2 |Z_\mu|^2 \tag{1.16}$$

The mass of the $W^\pm$ boson is described by $m_{W^\pm} = (g\mu/2\lambda)$. It is connected via the Weinberg angle Θ_w to the mass of the Z boson: $m_z = (1/\cos\Theta_w)m_{W^\pm}$. The Weinberg angle is measured experimentally and not predicted by the EW theory. Its value is $\approx 30\,^\circ$. The mass of the photon field A_μ is correctly predicted to be zero. The mass of the Higgs boson is $m_H = \sqrt{2}\mu$, as in the $U(1)$ model. From the measured mass of the $W^\pm$ bosons and further measurements of electroweak observables, the ratio μ/λ is determined to $\mu/\lambda = 246$ GeV. Since m_H depends on μ and not on the ratio μ/λ, the Higgs mass is unknown [6].

1.2.3. The Introduction of Fermion Masses

The dynamic of fermions is described by the Dirac Lagrangian:

$$\mathcal{L}_{Dirac} = \overline{\Psi}(i\gamma^\mu D_\mu - m)\Psi \tag{1.17}$$

Fermions are described by Dirac spinors Ψ. In case of a covariant derivative D_μ that describes strong interactions, Equation 1.17 is invariant under local $SU(3)$ gauge transformations. Therefore, Equation 1.17 does not need the insertion of a Higgs field $\mathbf{\Phi}$ to account for the fermion mass. Since gluons are described as massless particles in QCD, both bosons and fermions do not need the Higgs mechanism to sustain the gauge invariance in QCD.
The situation is different for EW interactions: Equation 1.17 mixes mass and coupling terms between right- and left-handed fermions. Since fermions of different chirality transform differently under the EW gauge group $U(1)_Y \otimes SU(2)_L$, the gauge invariance is violated by the mass term in Equation 1.17. Gauge invariance can be maintained by replacing the simple mass term of the Dirac Langrangian by a Higgs-fermion coupling term:

$$\mathcal{L}_{Higgs,fermion} = -\tilde{g}_f[\,\overline{R}\mathbf{\Phi}^\dagger\mathbf{L} + \overline{\mathbf{L}}\mathbf{\Phi}R\,] \tag{1.18}$$

The multiplicative factor $\tilde{g}_f$ describes the coupling strength between the Higgs field and the fermions. The field R symbolizes a right-handed Dirac spinor. Due to the parity violation of the EW theory, it is described by an isospin singlet. The field $\mathbf{L}$ is an isospin doublet. The additional term $\mathcal{L}_{Higgs,fermion}$ results in a fermion mass $m_f = \tilde{g}_f \mu/\sqrt{2}\lambda$ and couplings between the fermion and the Higgs field [9].

1.3. Search for the Higgs Boson at LEP and the Tevatron

Since the mass of the Higgs boson is not predicted by theory, the search for the Higgs boson at the e^+e^- collider LEP (1989-2000) and the $p\overline{p}$ collider Tevatron (1983-2011) have been designed as scans over the Higgs mass m_H by using various production and decay channels. Besides these direct searches, the mass range of a possible Higgs can be constrained by electroweak precision measurements.

1.3.1. Contraints from Precision Measurements

The ratio of the masses of the $W^\pm$ bosons and the Z boson depends on the mass of the Higgs boson, since it contributes through loop corrections to the vacuum polarization of the $W^\pm$ and Z bosons. Therefore, m_H can be constrained by a fit to the measurements of electroweak observables as the $W^\pm$ and Z mass. By performing a fit to the data from LEP, the Tevatron and further experiments, the following constraint on m_H is achieved: m_H is supposed to lie in the mass range 94^{+29}_{-24} GeV (two-sided limit, $CL = 68$ %) and below 152 GeV (one-sided limit, $CL = 95$ %).

1.3.2. Direct Measurements at LEP and the Tevatron

- The direct Higgs search at **LEP** was dominated by the Higgs production mechanism $e^+e^- \to HZ$. It describes the annihilation of the e^+e^--pair to a Z boson that radiates a Higgs boson. LEP I operated with a centre-of-mass energy $\sqrt{s}$ in the range of the mass of the Z boson m_Z: $\sqrt{s} \approx m_Z$. Therefore, the Z boson before the Higgs radiation would be on the mass shell, whereas the final state Z boson would be virtual. Since LEP II ran with $\sqrt{s} > m_Z$, the intermediate Z would be

virtual. The dominant production mechanism constraints kinematically the Higgs production in dependence of m_H by an easy rule of thumb: if $m_H > \sqrt{s} - m_Z$, the Higgs production is suppressed by around one order of magnitude compared to the case $m_H < \sqrt{s} - m_Z$.
Due to the lower centre-of-mass energy at LEP I, only the range of very small Higgs masses could be studied. The detector signature of interest contained the decay of the virtual Z and the Higgs. The Z was reconstructed by a pair of leptons with a mass $m_{ll} < m_Z$. The search resulted in a lower bound of $m_H > 65$ GeV at 95 % confidence level. At LEP II, more decay modes of both the Z and the Higgs were studied. Due to the higher centre-of-mass energy, the mass range of the Higgs that could be studied, was significantly increased. As can be seen in Figure 1.1, light Higgs bosons are supposed to decay dominantly into the heaviest pair of fermions that is kinematically allowed. Therefore, especially the decay modes $H \to b\bar{b}$ and $H \to \tau^+\tau^-$ were studied. Since no significant excess was observed, a lower limit of $m_H > 114.4$ GeV was derived at 95 % confidence level [10].

- The Higgs production mechanism at the **Tevatron** (Run I:$\sqrt{s} = 1.8$ TeV, Run II:$\sqrt{s} = 1.96$ TeV), depicted in Figure 1.2, is driven by the gluon-gluon fusion via a fermion loop ($gg \to H$) and followed by the associated Higgs production of a $W^{\pm}$ boson (WH) or a Z boson (ZH). The most sensitive decay channel depends on the considered Higgs mass: For $m_H \lesssim 135$ GeV, the decay into a pair of b quarks ($H \to b\bar{b}$) is the most sensitive channel, whereas for higher Higgs masses the decay into a W^+W^- pair is preferred.
  For the search of a low-mass Higgs, the dominant production channel $gg \to H$ cannot be combined with the dominant decay channel $H \to b\bar{b}$ since the background, namely the strong production of $b\bar{b}$ pairs, is too large. Therefore the decay $H \to b\bar{b}$ is combined with the associated production via WH or ZH. The use of the leptonic decays of the W or Z boson represents an efficient mean for the suppression of the multijet background. Besides the decay into charged leptons, also the decay of the Z boson into a pair of neutrinos ($Z \to \nu\overline{\nu}$) is analysed. The neutrinos leave only an indirect signature in the detector by violating the energy balance of the detected particles in the transverse plane and giving rise to missing transverse energy $\not\!\!E_{\mathrm{T}}$ (defined in Section 3.1.4). By searching for events with $\not\!\!E_{\mathrm{T}}$ and a pair of b quarks, the analysis does not only account for $Z \to \nu\overline{\nu}$ events but also for $W \to l\nu$ events, where the charged lepton was not detected.

For higher mass, the $gg \to H$ production channel can be used, since one can use the leptonic decay of the $W^{\pm}$ boson in the dominant $H \to W^+W^-$ decay channel. But also the combination of the associated production WH with the $H \to W^+W^-$ decay is a sensitive search channel, since the final state ($W^{\pm}W^+W^-$) can contain three leptons including a pair of same-sign leptons resulting in a low background [10].
The latest results of the Tevatron after analysing up to 10 fb^{-1} yield two observed exclusion regions for the Higgs mass at 95 % confidence level: 100 GeV $< m_H <$ 103 GeV and 147 GeV $< m_H <$ 180 GeV. Besides, an access with the local significance of 3 σ was detected at $m_H \approx 120$ GeV. After accounting for the possibility of such an access in the full mass range (Look Elsewhere Effect LEE), the local significance of 3 σ decreases to a global significance of 2.5 σ [11].

Figure 1.1.: Branching ratios of a SM Higgs a function of the Higgs mass [10].

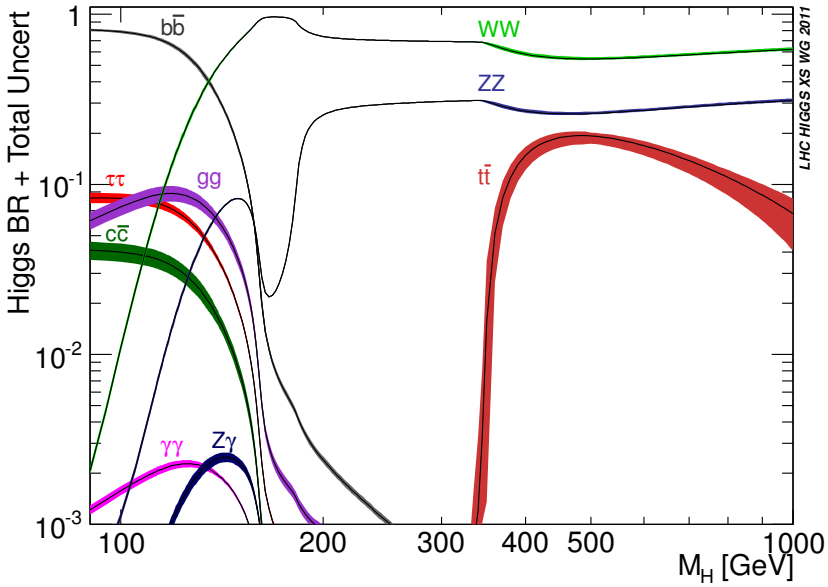

Figure 1.2.: Higgs production cross sections as function of the Higgs mass for $p\overline{p}$ collisions at $\sqrt{s} = 1.96$ TeV [10].

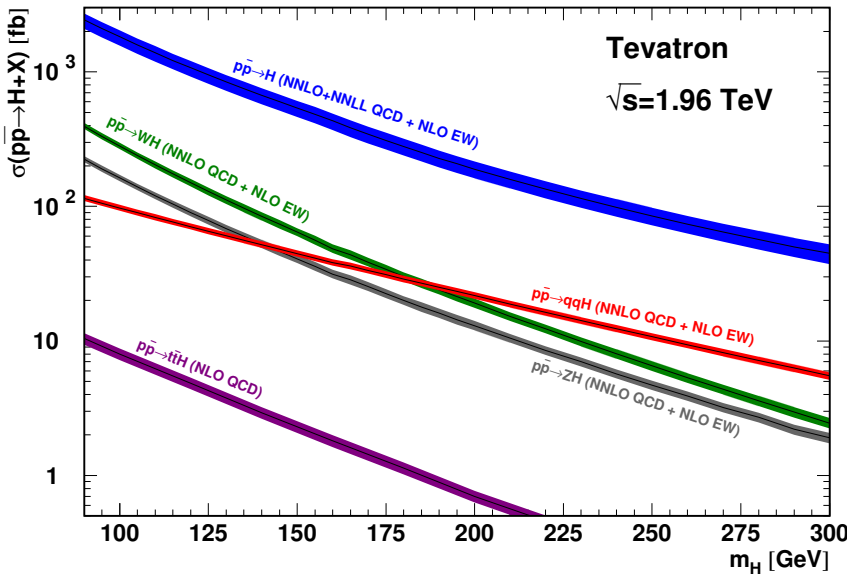

1.4. Higgs Hunting at the LHC Experiments and the Discovery of a Higgs-Like Particle

1.4.1. Search Channels for a SM Higgs Boson at the LHC

As can be seen from Figure 1.3, the main production channels at the LHC are the same as for the Tevatron: gluon-gluon fusion $gg \to H$, vector boson fusion VBF (qqH or $q\bar{q}H$) and the associated production (WH or ZH). The importance, though, of the various channels is different between the LHC and the Tevatron. It is influenced by the different centre-of-mass energy, which is $\sqrt{s} = 7$ TeV ($\sqrt{s} = 8$ TeV in 2012) at the LHC and therefore much larger than at the Tevatron. This leads to a larger gluon parton density at the LHC collisions, especially at low parton momentum fractions. Besides, the different production cross sections are different for pp collisions than for $p\overline{p}$ collisions. Also, a larger mass range of the Higgs boson can be studied at the LHC due to the large centre-of-mass energy.
Both LHC experiments that are involved in the search for the Higgs boson, ATLAS and CMS, analysed a variety of search channels. In the low-mass range $m_H < 120$ GeV, the $H \to \gamma\gamma$ channel is the most sensitive one. It is studied for the $gg \to H$ production mode, as well as the associated productions WH or ZH and the VBF channel. In the associated

decay modes only the hadronic decays of the W or Z are considered. Therefore, the $H \to \gamma\gamma$ can be classified according to the jet multiplicities. The $H \to b\bar{b}$ decay channel contributes as well to the low-mass Higgs search and was analysed by both experiments in combination with the associated production WH and ZH (see also Section 1.5). Although the cross section is enhanced compared to the Tevatron, this decay channel suffers in comparison from much more background and is therefore less sensitive than the $H \to \gamma\gamma$ channel. As a second fermionic decay channel, the $H \to \tau^+\tau^-$ decay is studied by CMS and ATLAS. In analogy to the $H \to \gamma\gamma$ channel, the $H \to \tau^+\tau^-$ can be divided into sub-channels according to the jet multiplicity, that depends on the Higgs production mode. The most important background in this channel are $Z \to \tau^+\tau^-$ decays. Additionally, the $WH \to l\nu\tau^+\tau^-$ channel is studied in CMS.
In the mass range $m_H > 130$ GeV, where the Higgs decay into massive gauge bosons becomes more likely (see Figure 1.1), the channels $H \to W^+W^- \to l^+\nu l^-\nu$ and $H \to ZZ \to l^+l^-l^+l^-$ are most sensitive. The most important background to the $H \to W^+W^-$ channel is the SM W^+W^- production. In ATLAS, the semi-leptonic channel of the $H \to W^+W^- \to l^+\nu q\overline{q'}$ is analysed besides the fully leptonic decay. CMS accounts furthermore for the associated production and studies the trileptonic channel $W^\pm H \to W^\pm W^+W^- \to l^\pm\nu l^+\nu l^-\nu$. The channel $H \to ZZ \to l^+l^-l^+l^-$ is called the "golden" channel, since it has only a very low background and is very well suited to reconstruct the mass of the

Figure 1.3.: Higgs production cross sections as function of the Higgs mass for pp collisions at $\sqrt{s} = 7$ TeV [10].

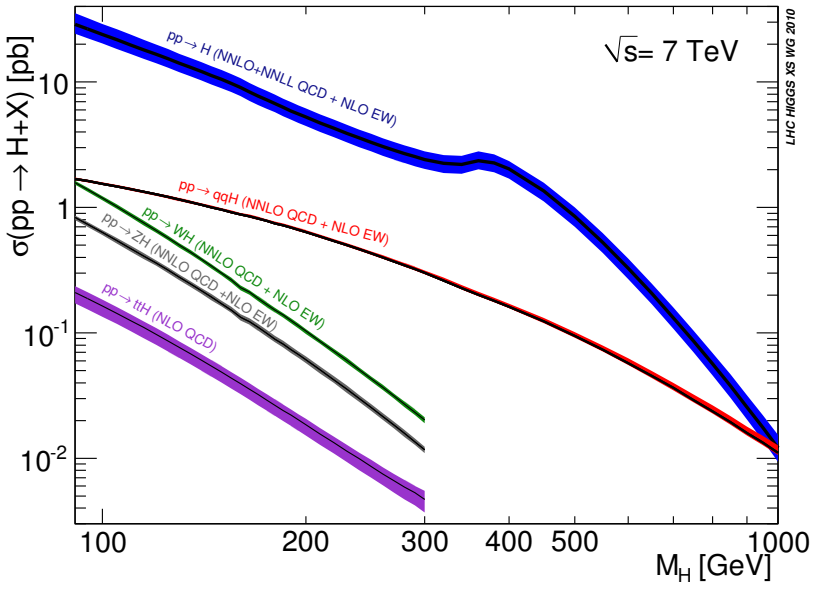

predicted Higgs boson. Besides the four lepton final state, the semileptonic final state including two quarks or two hadronically decaying tau leptons is analysed.

1.4.2. The Discovery of a Higgs-Like Boson at ATLAS and CMS

On July 4^{th}, 2012, the discovery of a new particle in the search for the Standard Model Higgs boson was announced by the ATLAS and the CMS collaborations [1, 2].
Both experiments analysed the various Higgs search channels in the full 2011 data sample at $\sqrt{s} = 7$ TeV that comprise an integrated luminosity of around 5 fb^{-1}. Besides, ATLAS studied the most sensitive Higgs channels for an integrated luminosity of ≈ 5.8 fb^{-1} of the 2012 run at $\sqrt{s} = 8$ TeV that was recorded between April and June 2012: $H \to ZZ \to l^+l^-l^+l^-$, $H \to \gamma\gamma$, and $H \to W^+W^- \to e^\pm\nu\mu^\mp\nu$. The CMS experiment considered furthermore the decays $H \to \tau^+\tau^-$ and $H \to b\bar{b}$ in their ≈ 5.3 fb^{-1} data sample of 2012. The results of the two experiments can be summarised as follows:

- By combining statistically the analyses of the 2011 and 2012 Higgs search channels, **ATLAS** can exclude the Higgs mass region 111 GeV $< m_H <$ 559 GeV at 95 % confidence level, except for the narrow range 122 GeV $< m_H <$ 131 GeV. Instead of an exclusion, a discovery of a new particle can be stated in this range with a local significance of 5.9 σ. After accounting for the Look Elsewhere Effect (LEE) in the mass range $110 - 600$ GeV, the local significance of 5.9 σ decrease to the global significance of 5.1 σ. The global significance is above the 5.0 σ threshold, that is commonly used to claim a discovery. The probability, that this excess of 5.1 σ can be observed assuming the absence of a Higgs signal in the region $110 - 600$ GeV is 1.7×10^{-7}.
  The excess is mainly driven by the channels $H \to ZZ \to l^+l^-l^+l^-$ and $H \to \gamma\gamma$. Since the final state of these channels does not contain any missing transverse energy $\not{E}_\mathrm{T}$ and the energy of the final state particles can be measured with good precision, they have the best mass resolution of the sensitive channels. A likelihood fit to the invariant mass of the final state particles in both channels determines the mass of the new particle to 126.0$\pm$0.4 (stat)$\pm$0.4 (sys) GeV. The systematic uncertainties on the mass are mainly due to the limited knowledge of the energy scale and resolution of electrons and photons.
  Figure 1.4 shows the combined analysis of the Higgs channels studied by ATLAS as

function of the hypothesised Higgs mass m_H: The top most plot shows the observed and expected upper limit on the signal strength μ, defined as the cross section normalized to the SM Higgs cross section $\mu = \frac{\sigma}{\sigma_H}$. The expected limit is derived under the assumption that the data would be purely background. Almost the full mass range can be excluded except for $m_H > 559$ GeV and the narrow region at around $m_H \approx 126$ GeV. It can be concluded from the expected limit, that it should be possible to exclude the full low mass range in the case of the absence of the Higgs. The middle plot illustrates the probability p_0 of the compatibility of the real data with the background-only hypothesis. It is locally less than 10^{-8} for $m_H \approx 126$ GeV. The p_0 value derived with the real data is compared to the one derived with simulated data consisting of background and signal with $\mu = 1$. The p_0 value of the real data is even smaller than for the simulated data. This can be understood with the lower most plot. It shows the best-fit value of the signal strength to the real data. For the discovery region at $m_H \approx 126$ GeV, it is 1.4 ± 0.3 and hence slightly above one.
Figure 1.5 gives an overview over the different channel that contribute to the ATLAS Higgs limits and the discovery of the new particle. Besides the combined limits, the observed and expected limits for all channels are shown separately.
The signal strength is still compatible with the SM Higgs boson ($\mu = 1$) within the uncertainty. Besides, the decay of the new particle into final states with a net electric charge of zero, indicates that it is a neutral particle. The decay of the new particle in a photon pair make the spin 1 option unlikely [1].

- The combination of the various Higgs search channels leads also in the **CMS** experiment to the discovery of a new particle. The Higgs boson is excluded at 95 % CL in the range 128 GeV $< m_H <$ 600 GeV and 110 GeV $< m_H <$ 121.5 GeV. In the intermediate region, a significant excess prevents the exclusion. It has a local significance of 5.0 σ at $m_H \approx 125$ GeV. Considering the LEE effect in the range 115 GeV $< m_H <$ 130 GeV leads to the reduced significance of 4.6 σ. By fitting the mass of the new particle to the invariant mass of the final state in the channels $H \to ZZ$ and $H \to \gamma\gamma$ results in the following mass: 125.3±0.4 (stat)±0.5 (sys) GeV. The best-fit parameter of μ for the combination of all channels is $\mu = 0.87 \pm 0.23$. This value is in perfect agreement with a SM Higgs boson [2].

The results from ATLAS and CMS are consistent within their uncertainties. Both experiment reveal a new particle that is compatible with a SM Higgs boson. But further data

and studies are needed for the exploration of its detailed nature. To learn more about the couplings between the Higgs-like particle and fermions, the challenging decay channels into a pair of fermions have to be done.

Figure 1.4.: The combination of the ATLAS Higgs search results obtained with 2011 and 2012 data. As function of the Higgs mass are depicted: (a) the observed (solid) as well as the expected (dashed) exclusion limit on the signal strength parameter μ (σ/σ_H) at 95 % CL. (b) the probability p_0 that the observed (solid) data as well as simulated data containing background and signal with $\mu = 1$ (dashed) is compatible with the background-only hypothesis. (c) the value of the signal strength μ fitted to the real data together with the $\approx$ 68 % confidence level around the fitted value [1].

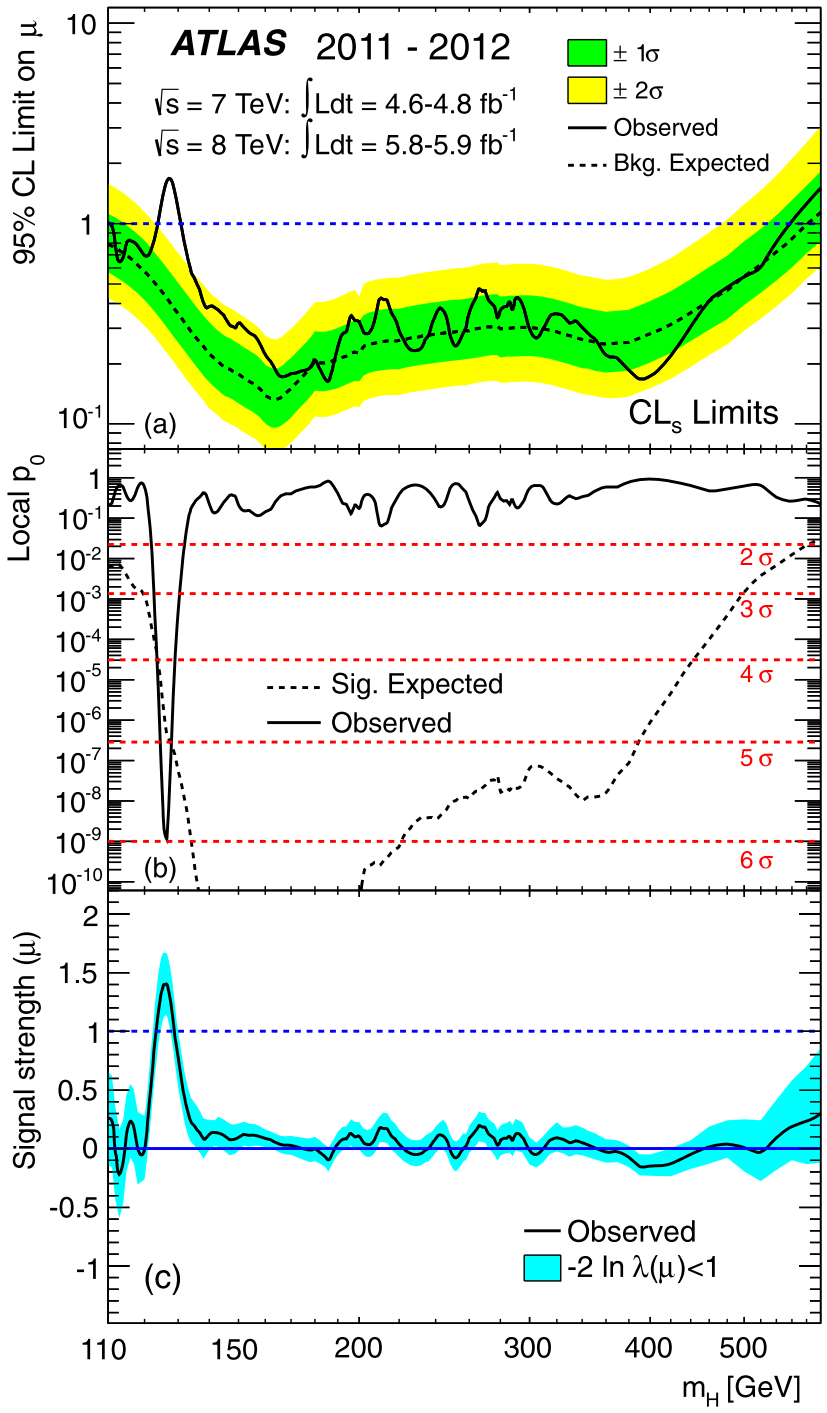

Figure 1.5.: The observed (solid) and expected (dashed) ATLAS exclusion limits of the signal strength σ/σ_H at 95 % CL as function of the Higgs mass m_H. The different Higgs search channels are depicted separately besides the combined limits. For visibility reasons, the important low-mass region is depicted again in detail. [1]:

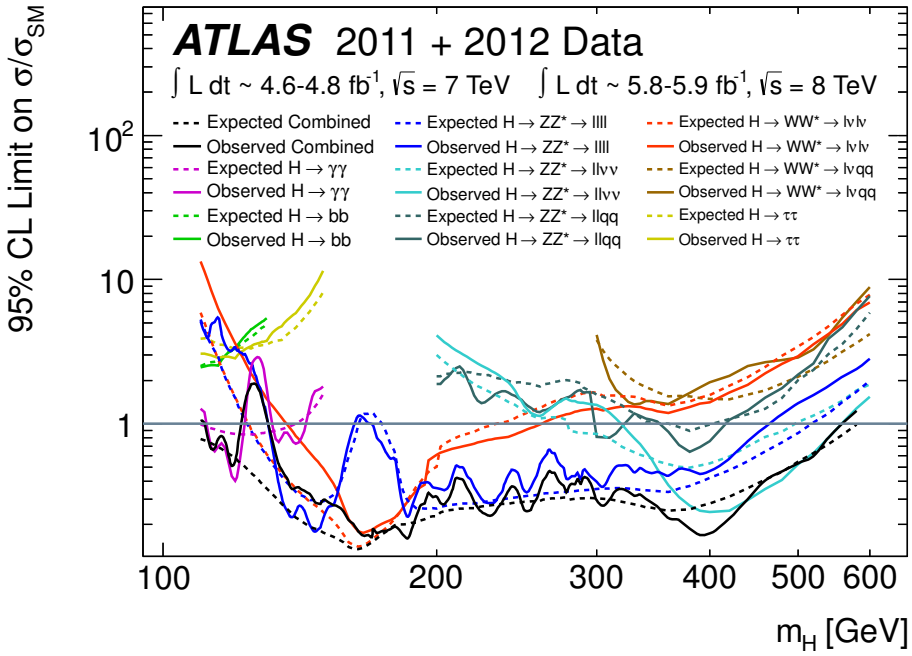

(a) for the full mass range of m_H.

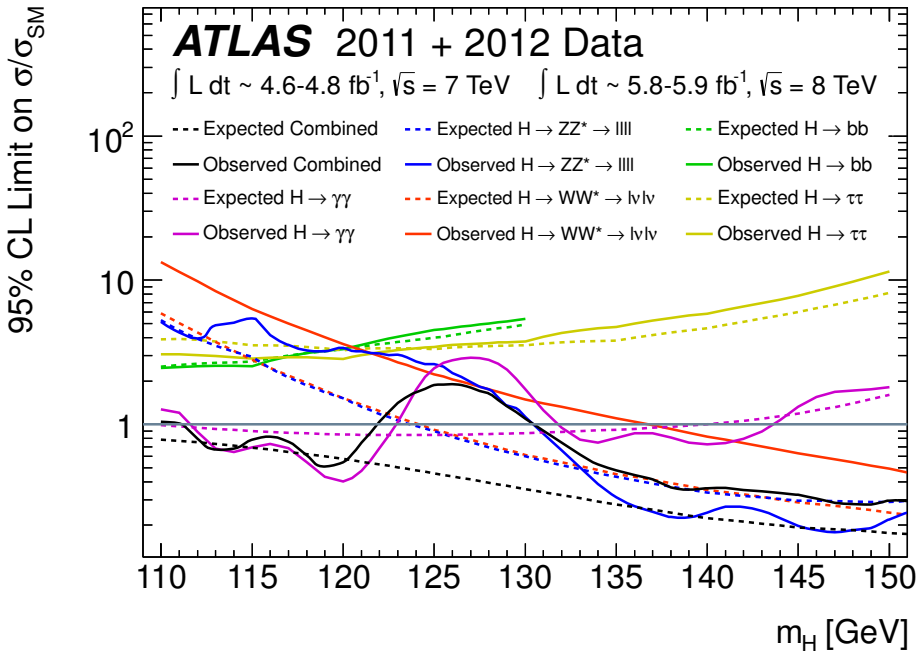

(b) in the low mass regime.

1.5. Higgs Boson Searches in the WH $\rightarrow$ lνb$\bar{\text{b}}$ Channel

The decay of the Higgs boson into a pair of b quarks is dominant for $m_H \lesssim 130$ GeV (see Figure 1.1). As was already mentioned in Section 1.4.1, the dominant low-mass decay can not be combined with the dominant production mechanism $gg \rightarrow H$ due to the huge amount of expected multijet background. Therefore, this decay mode is combined with the associated production modes WH, WZ, and $t\bar{t}H$, that can provide at least one lepton (electron or muon) for an efficient suppression of the multijet background.
The leading order Feynman diagrams for the three different $H \rightarrow b\bar{b}$ channels are shown in Figure 1.6. In case of the WH or ZH production, a pair of quarks annihilates to a virtual W or Z boson that radiate a Higgs. For the $t\bar{t}H$ production, a pair of top quarks is produced by strong interaction that radiates off a Higgs boson.
As brought up in Section 1.4.1, the $H \rightarrow b\bar{b}$ channels can not exploit their increased cross sections compared to the Tevatron, since the cross sections of the main background, W and Z boson in association with heavy flavour jets and the SM processes involving top quarks increase comparatively stronger. Especially the $WH \rightarrow l\nu b\bar{b}$ decay mode suffers from a large $t\bar{t}$ background due to the W boson and the b-jet pair in the final state, that are produced by the top quark decay. For ZH, the background from $t\bar{t}$ is reduced, but the background from a Z boson in association with heavy flavour jets is more problematic than the corresponding process for WH.
The first published results on $H \rightarrow b\bar{b}$ with LHC collision data was done by ATLAS using the first 1.04 fb^{-1} data of the 2011 run [12]. The channels $WH \rightarrow l\nu b\bar{b}$ and $ZH \rightarrow l^+l^-b\bar{b}$ were studied. At 95 % CL, the signal parameter $\mu \gtrsim 10$ could be excluded for $m_H \approx 110$ GeV after combining the WH and ZH. Both channels contribute comparably to the exclusion.
For the Higgs discovery paper [1], the full 2011 dataset has been analysed in the $H \rightarrow b\bar{b}$ channel. Besides channels analysed in the first publication [12], the channel $ZH \rightarrow \nu\bar{\nu}b\bar{b}$ was included. The sensitivity of the $WH \rightarrow l\nu b\bar{b}$ and the $ZH \rightarrow \nu\bar{\nu}b\bar{b}$ are very similar, the channel $ZH \rightarrow l^+l^-b\bar{b}$ is slightly worse. The contribution of the $H \rightarrow b\bar{b}$ exclusion limit to the combined ATLAS exclusion can be seen in 1.5: The sensitivity of $H \rightarrow b\bar{b}$ is comparable to the second fermion channel $H \rightarrow \tau^+\tau^-$. The exclusion power is maximal at $m_H \approx 110$ GeV, where $\mu > 2.5$ is excluded, and decreases to larger masses [13]. With more recorded data and enhancements in the analysis techniques, it will be possible to measure the important coupling of the Higgs boson to b quarks with ATLAS.
The analysis that will be presented in the following, has contributed to the ATLAS $WH \rightarrow l\nu b\bar{b}$ analysis for the full 2011 dataset [13]. It is a complementary, independent

analysis which gabe input to data-driven background estimation techniques, the definition of physics objects, and the treatment of systematic uncertainties.

Figure 1.6.: Leading order Feynman diagrams for the associated production via WH, ZH, and $t\bar{t}H$ and the decay mode $H \to b\bar{b}$. These channels are studied by ATLAS and CMS [14].

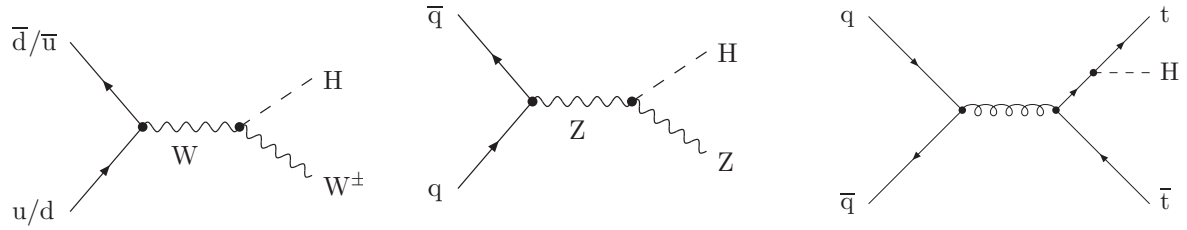

(a) WH production. (b) ZH production. (c) $t\bar{t}H$ production.

2. The ATLAS Experiment at the Large Hadron Collider

The Large Hadron Collider (LHC) is the world's most powerful hadron collider located at Cern, Geneva. It has four collision points where the different experiments reside. The general purpose experiments are ATLAS and CMS, two huge multi-purpose detectors, that are built to analyse the products of the high-energetic proton-proton collisions for precise test of the standard model, search for signatures of the Higgs boson and for new phenomena potentially detectable at the TeV scale. LHCb is specialized in the study of the differences between matter and antimatter by comparing the decays of b hadrons. Besides the potential to collide protons, the LHC is also equipped to collide heavy ions. ALICE analyses the collisions of lead ions which will hopefully generate a particular state of matter, the quark-gluon plasma. Finally, two small experiments, TOTEM and LHCf, are located near CMS and ATLAS, respectively, and focus on particles that are only slightly deflected in the collisions of protons or ions. TOTEM studies the proton-proton cross section and the proton structure; LHCf uses forward particles to simulate cosmic rays under laboratory conditions. Although ATLAS and CMS are devoted for proton-proton collisions, they analyse as well data from heavy ion collisions heavy [15].

2.1. The LHC at CERN

The LHC is a hadron accelerator and collider installed in the 26.7 km long tunnel that was originally built for the CERN LEP machine, an electron-positron collider which operated from 1989 to 2000 [16]. Two transfer tunnels exist with a length of around 2.5 km each that link the LHC to the CERN pre-accelerator complex [17].
In the CERN accelerator complex, protons, obtained by removing electrons from hydrogen atoms, are at first accelerated by a linear accelerator (LINAC2). Afterwards, they pass

three further pre-accelerators, the PS Booster, the Proton Synchrotron (PS) and the Super Proton Synchrotron (SPS), before being finally injected into the LHC. Here, counter-rotating bunches of up to 1.15×10^{11} protons will collide 40 million times per second providing high-energetic proton-proton collisions. It is designed for a centre-of-mass energy of 14 TeV and a luminosity of 10^{34} $\mathrm{cm}^{-2}\mathrm{s}^{-1}$ [15]. At full intensity, each proton beam consists of 2808 bunches [17].

The pre-acceleration of lead ions, gained by a source of vaporized lead, varies only in the first two acceleration steps with respect to protons. Instead of LINAC2, ions are at first accelerated by LINAC3, a further linear accelerator, and afterwards injected into the Low Energy Ion Ring (LEIR). In the LHC, pairs of ions collide with a nucleon-nucleon center-of-mass energy of up to 5.5 TeV at a design luminosity of up to 10^{27} $\mathrm{cm}^{-2}\mathrm{s}^{-1}$ [15]. Figure 2.1 illustrates the CERN site at the border between France and Switzerland at the foot of the Jura mountains. It shows the LHC ring with its final pre-accelerator, the SPS, and the caverns of the four experiments: ATLAS, CMS, ALICE and LHCb.

Figure 2.1.: The LHC at CERN and its geographical environment [15].

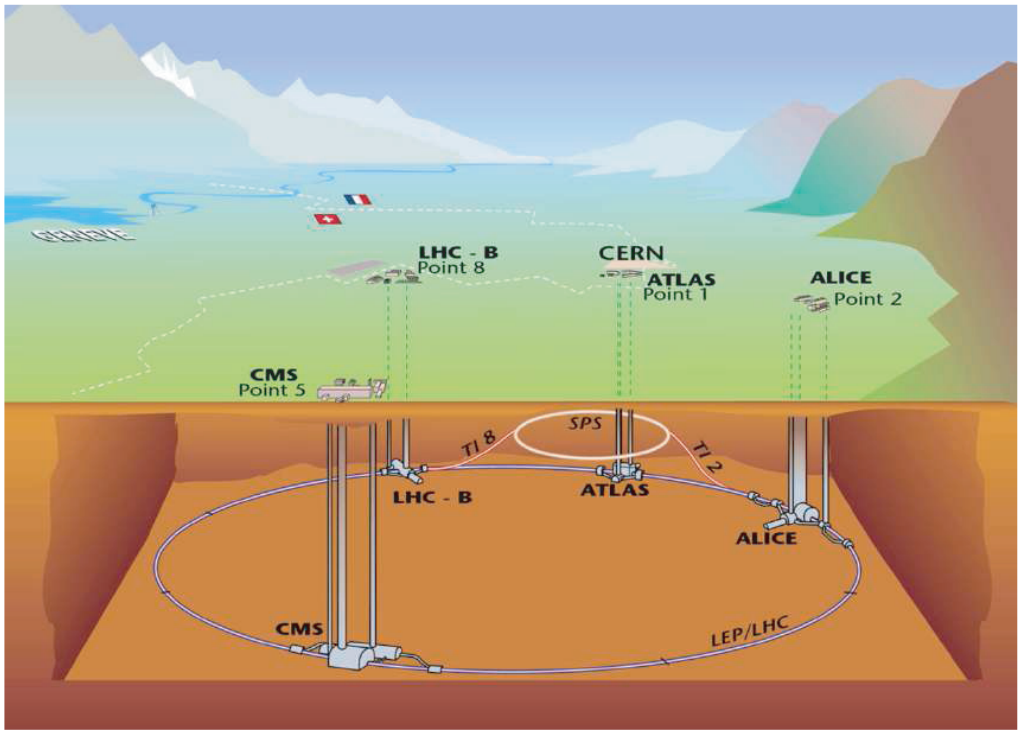

2.2. Proton-Proton Collisions at the LHC

After a serious accident shortly after the start of operation in 2008 and more than one year of reconstruction work, the beam energy was ramped up to 3.5 GeV leading to a centre-of-mass energy of 7 TeV. During 2010, an integrated luminosity $\int \mathcal{L}\, dt$ of 48.1 pb^{-1} was recorded. The integrated luminosity $\int \mathcal{L}\, dt$ quantifies the total amount of collected data. The instantaneous luminosity $\mathcal{L}$ is proportional to the event rate of a specific process. It is defined as

$$\mathcal{L} = \frac{n_b f n_1 n_2}{2\pi\sigma_x\sigma_y} \tag{2.1}$$

where n_b is the number of colliding bunches per beam, f the frequency of the circulating bunches, and n_1 and n_2 the number of protons in the colliding bunches. The parameters σ_x (σ_y) denote the width of the horizontal (vertical) beam profile. While the values for n_b, n_1, and n_2 are measured during the beam injection, the measurement of the beam profile follows the method of the van der Meer scan: The event rate is recorded while scanning the two beams across each other in the horizontal and the vertical direction. The recorded rates result in two curves that have a maximum at zero beam separation. These curves provide the beam profile parameters σ_x and σ_y [18].

After the winter shut down 2010/2011, the proton beams were again collided at a beam energy of 3.5 TeV but at a much higher luminosity $\mathcal{L}$ (see Figure 2.2). An integrated luminosity of $\mathcal{L} = 5.61$ fb^{-1} was delivered [19]. The increased luminosity was paired by a larger number of bunches and by a larger number of interactions per bunch crossing μ. High values of μ result in a high "pile-up" meaning signals in the detectors, that are not part of the triggered hard-scattering event but originate from further proton-proton interactions. Dedicated methods are needed to filter out the events of interest (see Section 3.1).

In 2012, the centre-of-mass energy was raised to 8 TeV and $\mathcal{L} = 14.66$ fb^{-1} was delivered up to the time of writing this thesis. The huge luminosity was accompanied by $\mu \approx 30$. Figure 2.3 illustrates a high pile-up event reconstructed with the ATLAS detector in 2012: It consists of a Z boson candidate that decays into a muon pair and is surrounded by more than twenty further interactions [20].

The operation at the nominal beam energy of 7 TeV was postponed to 2014 after a long shut down in 2013.

Figure 2.2.: Delivered Luminosity as function of time for the LHC runs in 2010, 2011, and 2012. Both *pp* as well as *PbPb* collisions are considered [19].

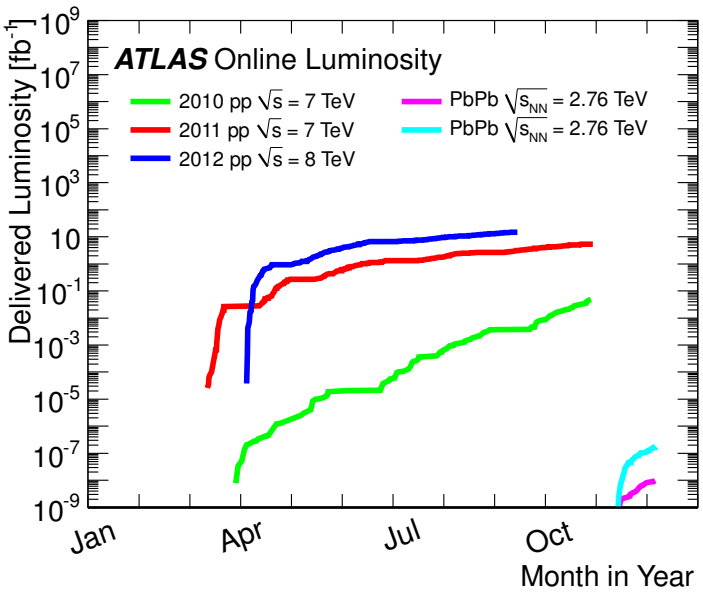

Figure 2.3.: $Z \rightarrow \mu\mu$ candidate among more than twenty pile-up interactions at ATLAS [20]. The two lines traversing the full detector illustrate the reconstructed muons. The various lines in the inner most detector part show reconstructed tracks from the muon pair and from charged particles of the pile-up interactions.

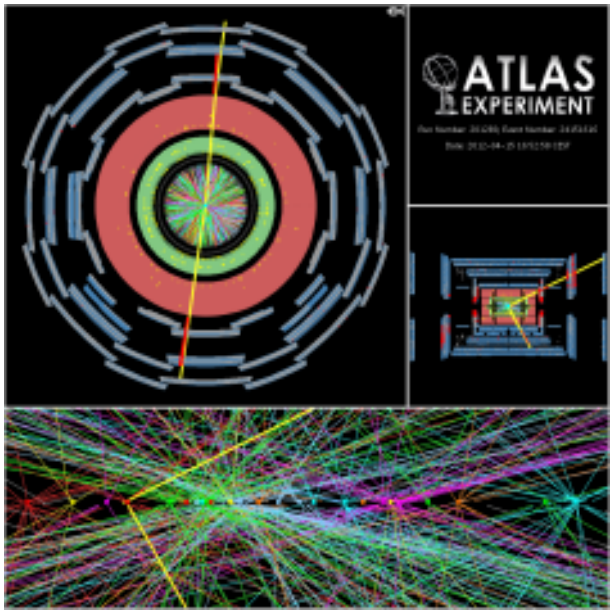

2.3. The ATLAS Detector at the LHC

With a height of 25 m and a length of 44 m, ATLAS (A Toroidal LHC ApparatuS), illustrated in Figure 2.4, is the largest detector of the LHC, although its weight of 7000 t falls below the one of the CMS detector. As a multi-purpose detector, ATLAS is characterized by different detector components surrounding the interaction point: a tracking detector, a calorimeter system and a muon spectrometer. The magnet configuration comprises a superconducting solenoid located around the inner detector and three large superconducting toroid systems (one barrel and two end caps) surrounding the calorimeters. Information about the general functionality of detectors can be found in [21]. The information about ATLAS is extracted from [22].

The ATLAS detector is forward-backward symmetric with respect to the nominal interaction point, which represents the origin of a right-handed coordinate system. The beam direction defines the z axis and the $x-y$ plane is transverse to it. The positive x axis points from the interaction point to the centre of the LHC ring and the y axis is defined as pointing upwards. The azimuthal angle ϕ (the polar angle θ) is measured around the z axis (the x axis) in the range $[-\pi, +\pi]$ ($[0, \pi]$); $\phi = 0$ ($\theta = 0$) corresponds to the positive x axis (positive z axis) and increases clockwise looking into the positive z direction (negative x direction). The pseudorapidity η is defined as $\eta = -\ln\tan(\theta/2)$; $\eta = +\infty$ ($\eta = -\infty$) corresponds to the positive (negative) z direction. $\eta = 0$ points in the positive y direction.

Transverse variables, such as the transverse momentum, p_T, of an object or its transverse energy, E_T, are defined in the transverse plane which corresponds to the $x-y$ plane of the detector. In the pseudorapidity-azimuthal space, the distance ΔR is defined as $\Delta R = \sqrt{\Delta\eta^2 + \Delta\phi^2}$.

The ATLAS detector was designed to be optimally responsive to new physics processes that could possibly occur at the TeV scale. In the following, the main features of the detector components are described:

- **inner tracking detector**: The inner detector is immersed in a 2 T magnetic field of a central solenoid. It is designed for high-precision momentum and vertex measurements of charged particles while handling the very large track density due to the around 1000 particles which will emerge from pp collisions every 25 ns. To satisfy these requirements, the inner tracking detector comprises in its innermost part silicon pixel detectors and silicon micro-strip trackers for precision track measurements. Both components cover the region $|\eta| < 2.5$. The outer part is a transition

Figure 2.4.: Cut-away view of the ATLAS detector [22]. To demonstrate the dimensions of the detector, some people are also pictured.

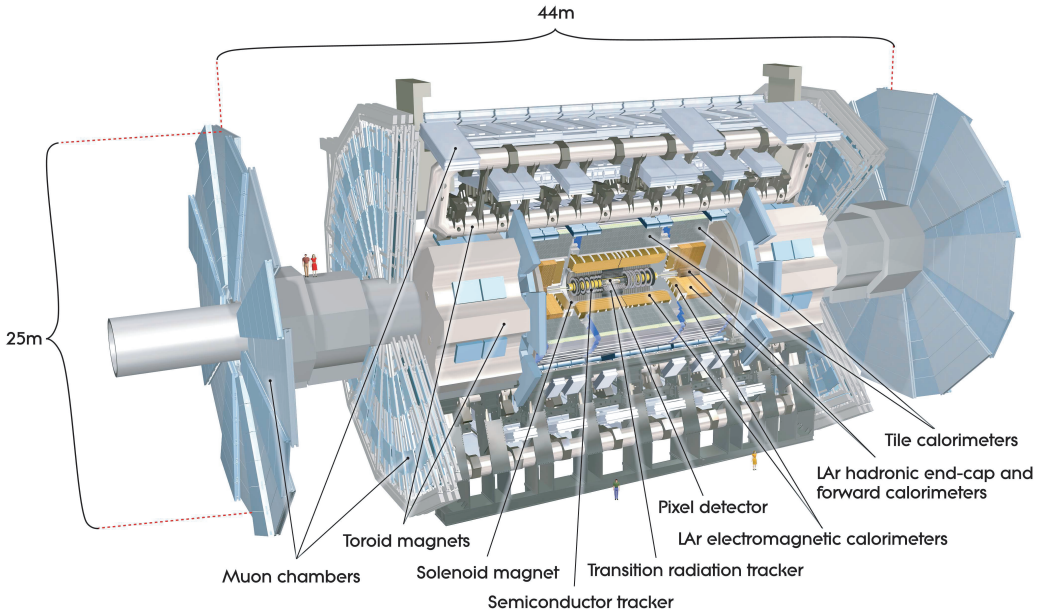

radiation tracker consisting of many layers of straw-tubes and material for transition radiation in between. It is restricted to $|\eta| < 2.0$.

- **calorimeter system** (for a detailed illustration, see Figure 2.5): Electrons, photons, tau decay products or hadrons, are absorbed inside the calorimeter system to allow for a precise energy measurement of the considered object. Its overall coverage is $|\eta| < 4.9$. It is divided into an electromagnetic and a hadronic part.
  The electromagnetic calorimeter system consists of liquid-argon (LAr) sampling calorimeters that use lead plates as absorber and are characterized by accordion-shaped electrodes. It is divided into a barrel part surrounding the central solenoid and a separate end-cap on each side, providing precise measurements of electromagnetic showers of electrons and photons. The barrel component covers the region $|\eta| < 1.52$ and the end cap the region $1.375 < |\eta| < 3.2$.
  Two different constructions are used for the hadronic calorimeter measuring hadronic showers. The hadronic tile calorimeter is a sampling calorimeter of scintillating tiles and absorbing steel. It comprises a barrel and an extended barrel covering the regions $|\eta| < 1.0$ and $0.8 < |\eta| < 1.7$, respectively. The LAr hadronic end-cap calorimeter with copper absorber and a coverage of $1.5 < |\eta| < 3.2$ is located directly behind the electromagnetic end cap.
  Finally, the calorimeter system includes a LAr forward calorimeter for measuring

both the electromagnetic and hadronic showers with copper absorber and tungsten absorber, respectively. It covers $3.1 < |\eta| < 4.9$.
Due to gaps and insensitive ("dead") material between different calorimeter components, the performance of the calorimeter depends on η. Especially worth mentioning is the region $1.37 < |\eta| < 1.52$, characterized by the transition from the electromagnetic barrel to the electromagnetic end cap and referred to as crack region in the following, and the region $|\eta| \approx 1.1$ where the transition from the barrel to the extended barrel of the hadronic tile calorimeter is located. In both regions, the reconstruction performance for electrons is degraded.

Figure 2.5.: The calorimeter system of ATLAS [22].

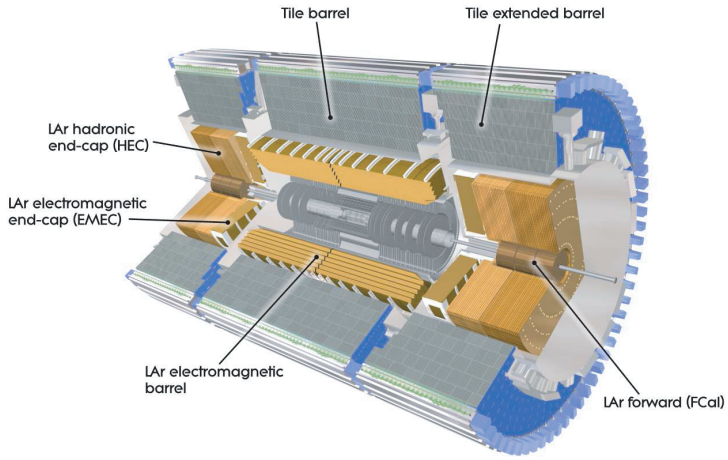

- **muon spectrometer**: The muon system surrounds the calorimeter and sets the overall dimensions of ATLAS. By reconstructing the curvature of muons that are bend in the magnetic field of the toroid system, muon tracking chambers perform high-precision measurements of the muon momentum for $|\eta| < 2.7$.
  In the barrel region, the magnetic field is mainly provided by eight radially aligned coils. For larger $|\eta|$ values, the importance of the two end-cap toroids, which are inserted at the ends of the barrel toroid, grows. In the barrel region, the muon chambers are aligned in three layers around the beam axis, whereas in the end-cap region three layers of chambers are located perpendicular to the beam. The muon system comprises four types of chambers: Monitored Drift Tubes ($|\eta| < 2.7$) and Cathode Strip Chambers ($2.0 < |\eta| < 2.7$) are developed for a precise measurement of the muon coordinate along the principal bending direction of the magnetic field. Resistive Plate Chambers ($|\eta| < 1.05$) and Thin Gap Chambers ($1.05 < |\eta| < 2.7$) are mainly used for triggering and for the measurement of the muon coordinate

orthogonal to the one measured by the precision tracking chambers. At $|\eta| \approx 0$, a gap in the muon spectrometer for a service shaft for inner detector components leads to a degraded muon reconstruction performance in this region.

2.4. Data Aquisition and Preparation

At the design luminosity of 10^{34} cm^{-2}s^{-1}, the expected interaction rate of proton-proton collisions is approximately 1 GHz. By contrast, the recording of the event data is limited to $\mathcal{O}(100)$ Hz. Therefore, a rejection factor of $5 \cdot 10^6$ is necessary to single out the events of interest. This is realized by different trigger levels: the hardware-based Level-1 (L1) trigger system uses a part of the total detector information to decide if the recorded event should be further processed or discarded. L1 reduces the data rate to about 75 kHz and defines Regions of Interest (RoI's), i.e. regions of the detector where interesting features are recognized in the event. The subsequent two levels, denoted as high-level trigger, are software based and comprise the Level-2 (L2) trigger and the event filter. L2 uses the detailed event information in the RoI's and reduces the trigger rate to approximately 3.5 kHz. The event filter finally reduces the rate to around 200 Hz by using offline analysis procedures. If the trigger rate of a certain trigger becomes too large it is prescaled. This means that the corresponding trigger is active only for a certain fraction of bunch crossings.

The ATLAS raw data that passes the event filter is stored at the CERN computing centre "Tier-0". Here, the data is reprocessed and the physics objects are reconstructed within the ATLAS software framework Athena. It is a skeleton providing and connecting a large amount of software tools necessary to manage and treat the collision data and simulated data. The data format containing very detailed information about the reconstructed event is called ESD (Event Summary Data). These large datasets are summarized to AOD (Analysis Object Data), a more user-friendly data format. The AOD can now be directly analysed or be further slimmed and adjusted to the purposes of the planned analysis. The desired information extracted from the AOD can also be stored in a data format called D3PD (Derived Physics Data). These D3PDs can be easily accessed by ROOT, an object-oriented data analysis framework devoted to the needs of data analysis in high energy physics [23].

After the reconstruction step, the output data is distributed to the "Tier-1"s, eleven large computing centres located all over the world. They can rerun the reconstruction with

updated detector alignment, calibration or reconstruction algorithms, and distribute the data to the more than 160 ”Tier-2“s. These smaller computing centres serve mainly for Monte-Carlo production and to run analysis jobs [24].

2.5. Event Generation

The collision data detected by ATLAS is a mixture of many different processes. To be able to study its composition it is crucial to produce separate samples of the known SM processes and possibly of not yet detected processes under study. The simulation of the different processes uses Monte-Carlo techniques for the numerical solution of the multi-dimensional integrals that occur in the description of high-energetic pp collisions [25].
The production and simulation of events is performed within the ATLAS software framework Athena. The events produced by an event generator run through different stages of a computing chain until they have achieved the format used for the physics analysis: After the generation of the events, they are passed through a GEANT4 simulation of the ATLAS detector. GEANT4 is a software tool kit describing the interaction of particles with matter [26]: the interactions of the previously generated particles with the different ATLAS detector components are simulated and stored in this step in the form of Hits. These GEANT4 Hits are subsequently digitized. Thereafter, the GEANT4 Digits are run through the reconstruction where the information of the GEANT4 Digits is assembled in particle tracks and energy deposits, for instance, and the identification of the objects traversing the detector takes place.
Besides the main parton interaction, also the interactions of the rest of the proton, the underlying event, has to be simulated. In ATLAS, this is mainly done by the Monte-Carlo generators Pythia [8] and Jimmy [27]. Pile-up events, the interaction of further proton pairs, are modelled by Pythia.
The reconstruction and the subsequent steps are done analogously for simulated data and collision data. As done for the collision data, the simulated data is distributed to different computing centres after their production.

3. Description of the Inclusive $WH \to l\nu b\bar{b}$ Analysis

This section details the various ingredients of the cut-based $WH \to l\nu b\bar{b}$ analysis, followed by an outline of the signal process and the background components. Finally, it discusses the studied event topology.

3.1. Reconstruction and Definition of Physics Objects

The reconstructed objects considered in this analysis are jets, leptons (electrons, muons) and missing transverse energy $\not{E}_{\mathrm{T}}$. The terms "electrons" and "muons" design both particles and antiparticles. For muons, electrons and jets exist a "signal" as well as a "veto" definition. Signal objects are the objects of interest and have to fulfil tight selection criteria. Veto objects follow looser selection requirements and they are rejected by a veto: Reconstructed objects that obey the veto definition but not the signal definition do not pass the analysis.

3.1.1. Muons

Muons are reconstructed by the "Muid" algorithms. These consist of four different reconstruction algorithms that either start from an inner detector track or from hits in the muon spectrometer [28, 29]:

- "Muid Combined" uses a global refit to combine an inner detector track with a muon spectrometer track resulting in a combined muon.

- "MuGirl" is seeded by inner detector tracks and searches for tracks and track segments in the muon spectrometer. If a refit between an inner detector track and a spectrometer track is successful, a combined muon is built. If this is not the case but a muon spectrometer track segment or track is close enough to the predicted position of an inner detector track at the muon spectrometer, the inner detector track is tagged as muon and is denoted as "tagged" muon.

- "MuTagIMO" is a further tagging algorithm and associates inner detector tracks with spectrometer segments. The statistical fitting procedure between inner detector tracks and muon spectrometer track segments is different for "MuTagIMO" compared to "MuGirl".

- "MuidStandalone" extrapolates muon spectrometer tracks to the beam line. This algorithm does not make use of inner detector tracks.

The definition of signal muons comprises the following requirements:

- The "Tight" criterion [30]: The muon has to be reconstructed by the "Muid Combined" or the "MuGirl" algorithm.

- The muon has to fulfil various inner detector track quality criteria [30].

- To reject cosmic muons two cuts on the transverse (longitudinal) impact parameter $z0$ ($d0$), defined as the shortest distance of the muon track on the z axis (the transverse plane) to the primary vertex are applied:

  - $|d0| < 0.1$ mm

  - $|z0| < 10$ mm

  The primary vertex is defined as the reconstructed vertex with the highest sum over the p_T of the vertex tracks.

- The following kinematic cuts are applied on the transverse momentum p_T and the pseudorapidity η:

  - $p_T > 25$ GeV

  - $|\eta| < 2.5$

- For an effective rejection of multijet background (see Section 3.6) cuts on the relative track and calorimeter isolation are applied. The isolation variable *ptcone*20 denotes the p_T of tracks in a cone of radius $R = 0.2$ around the muon without accounting for the p_T of the muon itself. In analogy, *etcone*30 quantifies the calorimeter energy around the muon in a cone of radius $R = 0.3$ and subtracts the (estimated) calorimeter energy of the considered muon:

  - $|ptcone20/p_T| < 0.1$

  - $|etcone30/p_T| < 0.14$, applied for muons in the η range $|\eta| < 2.4$

The veto muon definition differs from the signal definition in the following aspects:

- The "Loose" criterion [30]: The muon is reconstructed by one of the four "Muid" reconstruction algorithms.

- Except for standalone muons, the muons have to fulfil above inner detector, cosmic rejection and track isolation cuts. The calorimeter isolation is applied for all types of muons.

- The following kinematic cuts are applied on p_T and η:

  - $p_T > 10$ GeV

  - $|\eta| < 2.7$

3.1.2. Electrons

Electrons are reconstructed by an algorithm that starts from clusters in the electromagnetic (EM) calorimeter and searches for tracks in a $\Delta\eta \times \Delta\phi$ window around the regarded cluster whose momentum p matches the electromagnetic energy E [31]. As the inner detector η-acceptance is limited to $|\eta| < 2.5$, a matching between the cluster and an inner detector track is not possible for forward electrons, reconstructed for $2.5 < |\eta| < 4.9$. The latter are reconstructed only by means of the electromagnetic calorimeter with the forward cluster-based algorithm [31].

The electron reconstruction results in electron candidates. Since these candidates comprise besides real electrons also jets that fake the electron signature, dedicated variables are needed for a proper identification of real electrons and an efficient rejection of jets faking electrons. These variables describe, e.g., the track quality, the shower shape, the consistency between the inner detector and calorimeter information, and the leakage of energy of the electron candidate into the hadronic calorimeter. Depending on the tightness of the cuts on these variables, the quality of the electron identification can be specified by the "Loose, Medium, Tight" keywords [31].
The signal electron definition consists of the following requirements:

- The electron candidate has to be reconstructed by the outlined cluster-based algorithm.
- It has to fulfil the "Tight++" quality criterion [32].
- The following cuts are applied on the transverse energy E_T and the pseudorapidity η:
  - $E_T > 25$ GeV
  - $|\eta| < 2.47$
- To reject electrons not originating from the primary vertex, a cut on the transverse impact parameter $d0$ is applied, as defined in Section 3.1.1 for muons:
  - $|d0| < 0.1$ mm
- Clusters of degraded quality in the EM calorimeter have to be rejected through the electron object quality flag.
- The electron has to be isolated from other activity in the detector (the following variables are defined in analogy to the muon isolation variables introduced in Section 3.1.1):
  - $|ptcone20/E_T| < 0.1$
  - $|etcone30/E_T| < 0.14$

The veto electron definition differs in the following criteria:

- The electron candidate has to be reconstructed by the standard or the forward cluster-based algorithm [31].
- Electrons reconstructed by the standard algorithm have to fulfil the "Loose++" quality criterion, whereas forward electrons must satisfy the "frwdElectronLoose" condition [32].
- The following cuts are applied on E_T and η:
  - $E_T > 10$ GeV ($E_T > 20$ GeV for forward electrons)
  - $|\eta| < 2.47$ ($|\eta| < 4.5$ for forward electrons)
  - The cuts on $d0$, $|ptcone20/p_T|$, and $|etcone30/p_T|$ are the same as for signal electrons, but they are not applied on forward electrons. The calorimeter isolation $|etcone30/p_T|$ can not be used for forward electrons, since no pile-up corrections for this variable are available for the forward η region.

3.1.3. Jets

Jets are reconstructed with the anti-kt algorithm [33] with a radius parameter of $R = 0.4$ using topological clusters of the hadronic calorimeter as input [34]. The jet calibration is based on the electromagnetic scale. The EM scale correctly reconstructs the energy of particles inducing EM showers in the calorimeter system. It is determined by the reconstruction of test-beam electrons with test components of the ATLAS detector. A scaling factor, derived from simulation studies, calibrates the jet energy from the EM scale to the jet energy scale (JES) [35].

The signal jet definition has the following requirements:

- The following cuts are applied on the transverse energy E_T and the pseudorapidity η:
  - $E_T > 25$ GeV

- $|\eta| < 2.5$

- To reject jets coming from pile-up events, a cut on the Jet Vertex Fraction (JVF) is applied. The JVF is the scalar sum of p_T of tracks matched to a certain jet that originates from the primary vertex. It is normalized to the scalar sum of p_T of all tracks matched to the jets that originate from any reconstructed vertices [36]. The closer the JVF value is to 1 (0), the higher is the probability of the jet coming from the primary vertex (a pile-up vertex). Since inner detector tracks are needed for the JVF, this discriminant can only be used in the fiducial volume of the inner detector. Jets without associated tracks have the value JVF $= -1$. For the present analysis, a cut at $|\text{JVF}| > 0.75$ is applied.

- Jet quality cuts are applied to reject jets containing noisy calorimeter cells and jets originating from cosmic rays or non-collision background [35].

For the veto jet definition, these cuts are slightly modified:

- The cuts on the transverse energy E_T, the pseudorapidity η, and the JVF are:

  - $E_T > 20$ GeV

  - $|\eta| < 4.5$

  - $|\text{JVF}| > 0.75$, for $|\eta| < 2.5$

3.1.4. Missing Transverse Energy

Only weakly interacting particles like neutrinos traverse the ATLAS detector without leaving any direct signature. But since the energy in the transverse plane has to add up to zero, the missing transverse energy $\not{E}_{\mathrm{T}}$ allows to draw indirect conclusions on these undetected particles. Besides this "real" $\not{E}_{\mathrm{T}}$, mismeasurements or misidentifications from jets or leptons can lead to "fake" $\not{E}_{\mathrm{T}}$.
The $\not{E}_{\mathrm{T}}$ is calculated using calorimeter cells up to $|\eta| < 4.5$ and reconstructed muons up to $|\eta| < 2.5$ [37]. The muon term $\not{E}_{\mathrm{T}}{}^{\mu}$ is calculated by summing up the the negative momentum components of the muons present in the event. The x and y components are

calculated separately:

$$\not{E}_{\mathrm{T}}{}^{\mu}_{x(y)} = -\sum_{\text{muons}} p^{\mu}_{x(y)} \tag{3.1}$$

The calorimeter term $\not{E}_{\mathrm{T}}{}^{\text{calo}}$ is determined by matching the calorimeter cells to physics objects and calibrating them accordingly. The following objects are considered in $\not{E}_{\mathrm{T}}{}^{\text{calo}}$: electrons, photons, hadronically decaying taus, anti-kt jets, and muons. The order of the listed objects reflects the order of the attempt to match the calorimeter cells to the physics objects. Cells, that could not be matched to the physics objects are calibrated not by the EM+JES scheme as the selected jets but by a local cluster weighting method (LCW), that calibrates the individual cell clusters separately [35]. They are summarised as $\not{E}_{\mathrm{T}}{}^{\text{calo,CellOut}}$ term. An additional calorimeter term for muons, $\not{E}_{\mathrm{T}}{}^{calo,\mu}$ only shows up, if the muons in the muon term $\not{E}_{\mathrm{T}}{}^{\mu}$ are not yet corrected for the energy loss in the calorimeter system. Two different jet terms are regarded for the $\not{E}_{\mathrm{T}}{}^{\text{calo}}$ calculation: the $\not{E}_{\mathrm{T}}{}^{\text{calo,softjet}}$ term devoted for low-p_T jets (7 GeV $< p_T \leq$ 20 GeV). It uses jets that are reconstructed with a radius $R = 0.6$ and are calibrated by the LCW method. The second term, $\not{E}_{\mathrm{T}}{}^{\text{calo,softjet}}$, accounts for jets with $p_T > 20$ GeV and a radius of $R = 0.4$. These jets are as well LCW calibrated but the multiplicative jet energy scale (JES) factor is applied.
The $\not{E}_{\mathrm{T}}{}^{\text{calo}}$ component is calculated separately for each of the considered objects by summing up the negative calibrated cell energy:

$$\not{E}_{\mathrm{T}}{}^{\text{calo,object}}_{x} = -\sum_{i=1}^{N_{\text{cells}}} E_i \sin\Theta_i \cos\Phi_i \not{E}_{\mathrm{T}}{}^{\text{calo,object}}_{y} = -\sum_{i=1}^{N_{\text{cells}}} E_i \sin\Theta_i \sin\Phi_i \tag{3.2}$$

The $\sin\Theta_i$ term projects the cell energy E_i into the transverse detector plane, the $\cos\Phi_i$ ($\sin\Phi_i$) extracts the x (y) component inside the transverse plane. The sum of all $\not{E}_{\mathrm{T}}{}^{\text{calo,object}}_{x(y)}$ terms results in the final $\not{E}_{\mathrm{T}}{}^{\text{calo}}_{x(y)}$ components:

$$\begin{aligned}\not{E}_{\mathrm{T}}{}^{\text{calo}}_{x(y)} = \not{E}_{\mathrm{T}}{}^{\text{calo,electron}}_{x(y)} + \not{E}_{\mathrm{T}}{}^{\text{calo,photon}}_{x(y)} + \not{E}_{\mathrm{T}}{}^{\text{calo,tau}}_{x(y)} + \not{E}_{\mathrm{T}}{}^{\text{calo,jet}}_{x(y)} \\ + \not{E}_{\mathrm{T}}{}^{\text{calo,softjet}}_{x(y)} + (\not{E}_{\mathrm{T}}{}^{\text{calo,muon}}_{x(y)}) + \not{E}_{\mathrm{T}}{}^{\text{calo,CellOut}}_{x(y)}\end{aligned} \tag{3.3}$$

The final $\not{E}_{\mathrm{T}}$ is achieved by adding $\not{E}_{\mathrm{T}}{}^{\text{calo}}$ and $\not{E}_{\mathrm{T}}{}^{\mu}$ and calculating the transverse length:

$$\begin{aligned}\not{E}_{\mathrm{T}}{}_{x(y)} &= \not{E}_{\mathrm{T}}{}^{\text{calo}}_{x(y)} + MET^{\mu}_{x(y)} \\ \not{E}_{\mathrm{T}} &= \sqrt{\not{E}_{\mathrm{T}}{}^{2}_{x} + \not{E}_{\mathrm{T}}{}^{2}_{y}}\end{aligned} \tag{3.4}$$

3.1.5. Overlap Removal between Muons, Electrons and Jets

In the ATLAS reconstruction chain, all electrons are also reconstructed as jets. To avoid double counting, one has to remove these jets. On the other hand, jets can contain electrons from heavy flavour decays. In this case, one is interested in keeping the jet and rejecting the electron, that would be used to reconstruct the W candidate. That means one has to find a compromise between wrongly rejecting too many jets that contain electrons from heavy flavour decays and wrongly rejecting too many electrons that originate from W decays and are only reconstructed additionally as jet. In the present analysis, the transverse momentum p_T of the veto electrons is used as discriminator, since the p_T of electrons from heavy flavour decays is in mean lower than the p_T of electrons from W decays:

- If the distance between veto jets and veto electrons with $p_T > 20$ GeV is smaller than $\Delta R = 0.4$, the jet is removed.

- If the distance between veto jets and veto electrons with $p_T \leq 20$ GeV is smaller than $\Delta R = 0.4$, the electron is no longer considered.

Most of the muons that overlap with jets originate from heavy flavour decays and should therefore not be considered as muons from W candidates. For this reason all veto muons that are closer than $\Delta R = 0.4$ to a veto jet are removed after the electron-jet overlap removal.
A small percentage of muons radiates when traversing the calorimeter. This can result in reconstructed electrons that should be rejected. All veto electrons that are closer than $\Delta R = 0.2$ to a veto muon are therefore rejected.

3.1.6. Trigger Selection

The lowest unprescaled lepton trigger for each data taking period is used as trigger. It is the trigger with the lowest p_T threshold, that is not yet prescaled (see Section 2.4 for definition). These are listed in Table 3.1 for different data taking periods in 2011. Each trigger is defined by the corresponding trigger level (`EF` for event filter), the E_T (p_T) threshold of the electrons (muons), and the minimum quality criteria of the leptons to fire the trigger.

Table 3.1.: Lowest unprescaled single muon [38] and single electron [39] triggers for the different 2011 data taking periods.

data period	muon trigger	electron trigger
B - I	`EF_e20_medium`	`EF_mu18_MG`
J - K	`EF_e20_medium`	`EF_mu18_MG_medium`
L - M	`EF_e22vh_medium1 || EF_e45_medium1`	`EF_mu18_MG_medium`

3.1.7. Composite Kinematic Variables

Transverse Mass

The transverse mass M_T considered in the present analysis is an estimate of the mass of the leptonically decaying W boson. Since the neutrino escapes the ATLAS detector undetected, M_T is calculated by means of the $\not{E}_{\mathrm{T}}$ and the p_T of the charged lepton p_T^{lep} in the following way:

$$M_T = \sqrt{2p_T^{lep}\not{E}_{\mathrm{T}}(1 - \cos(\Phi^{lep} - \Phi^{\not{E}_{\mathrm{T}}}))} \tag{3.5}$$

As the energy is balanced merely in the transverse plane at a hadron collider, only transverse quantities are used in Equation 3.5. Furthermore, the invariant mass of the lepton is neglected.

Transverse Momentum of the W Boson

The reconstructed p_T of the W boson p_T^W is calculated using the x and y component of the $\not{E}_{\mathrm{T}}$ and the lepton transverse momentum p_T^{lep}:

$$p_T^W = \sqrt{(\not{E}_{\mathrm{T}_x} + p_{T_x}^{lep})^2 + (\not{E}_{\mathrm{T}_y} + p_{T_y}^{lep})^2} \tag{3.6}$$

This variabale is used at the final selection step of the analysis when the events are distributed into several p_T^W bins to improve the sensitivity of the exclusion limits (see Section 8).

Invariant Mass of Two Jets

The invariant mass of two jets m_{jj} is calculated via the scalar product of the corresponding jet four-momentum vectors. After applying b-tagging (see Section 3.2) to the two jets, the invariant mass is symbolized by $m_{b\bar{b}}$ and it is directly related to the mass of a Higgs boson decaying into a $b\bar{b}$ pair. Therefore, $m_{b\bar{b}}$ of the two b jets is the key distribution after the final event selection (see Section 3.6) and is used as input for the limit calculation (see Section 8).

3.2. The b-Tagging Algorithm

To study the $H \to b\bar{b}$ decay channel, an efficient identification of b jets and powerful rejection of non-b jets is crucial. The various methods for the identification of b jets, the b-tagging, make use of the particular properties of jets containing b hadrons. The most important one among them is the relatively long lifetime of b hadrons ($\mathcal{O}(1.5$ ps)) leading to a flight path length of ≈ 3 mm for a jet of $p_T = 50$ GeV before the b hadron decays. This results in observable identification criteria: Tracks reconstructed from charged particles from the b hadron decay have a large impact parameter with respect to the primary vertex. In some cases, the secondary vertex that is built by those tracks can be reconstructed [28]. In the present analysis, the MV1 algorithm is used. It is based on the output weights of the IP3D, SV1 and JetFitterCombNN taggers as input to a neutral network [40]. The IP3D algorithm uses information of track impact parameters whereas the SV1 algorithm tries to reconstruct a secondary vertex inside the jet. The JetFitterCombNN takes advantage of the topology of weak b hadron decays inside the jet [41]. All three tagging algorithms are based on a likelihood ratio technique for the calculation of a b-tag weight:
The measured value V_i of a discriminating variable is compared to the (multi-dimensional) probability density functions for both the b and the light jet hypotheses $b(V_i)$ and $u(V_i)$. Depending on the tagging algorithm, the ratio $b(V_i)/u(V_i)$ defines the track or vertex weight. Summing over the logarithm of all the track/vertex weights of a jet results in the tag weight W_{jet} of a jet. Likelihood taggers can easily be combined by simply adding up the individual tag weights W_{jet} [28].
To select b jets with a certain tag efficiency, a cut on W_{jet} is applied. This leads to a specific efficiency to tag b jets (b-tag efficiency) and an efficiency to wrongly tag non-b jets (mistag rate). Since the tag efficiency as well as the mistag rate depends on the the p_T and

η distributions of the jets, the b-tag efficiency / mistag rate varies from sample to sample for a certain cut value on W_{jet}. In ATLAS, a simulated $t\bar{t}$ sample, that contains $t\bar{t}$ pairs with at least one leptonically decaying W boson (non-fully hadronic), is used to benchmark the relation between the b-tag efficiency and the cut on W_{jet}. The cut $W_{jet} > 0.601713$ for the MV1 algorithm corresponds to a b-tag efficiency of 70%. This cut value is chosen for the presented analysis. Figure 3.1 depicts for the non-fully hadronic $t\bar{t}$-sample for four powerful tagging algorithms (MV1, JetFitterCombNN, JetFitterCombNNc, IP3D+SV1) and one very simple secondary vertex algorithm (SV0) the relation between the b-tag efficiency and the rejection rate, defined as inverse of the mistag rate. For a given b-tag efficiency, the MV1 algorithm has the best light-jet rejection.

Figure 3.1.: The light jet rejection as function of the b-tag efficiency for various tagging algorithms shown for a non-fully hadronic $t\bar{t}$ sample [40].

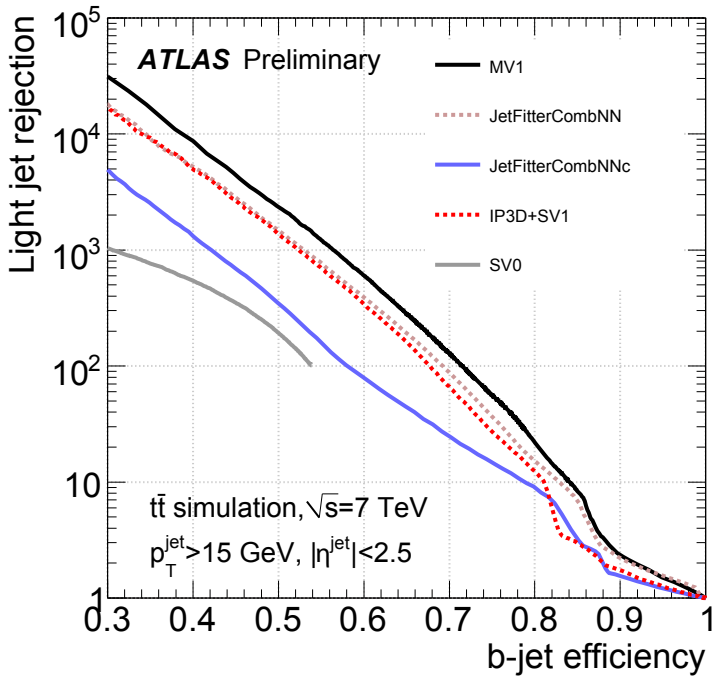

3.3. Event Weighting and Cleaning

Although the simulated Monte-Carlo (MC) samples try to describe the collision events and the subsequent reconstruction of objects as close as possible to the real conditions, they are after their production further corrected for an even better agreement between MC and real data.

During data taking, not all part of the ATLAS detector and the data recording infrastructure work perfectly all the time. Therefore it is necessary to filter out events or even small data periods with degraded data quality.

Pile-up Reweighting

During the crossing of two proton bunches several pairs of protons can interact with each other. The interactions between different protons besides the main hard scatter are called in-time pile-up events. Furthermore, proton-proton interactions of subsequent or previous bunch crossings can leave energy deposits or particles in the ATLAS detector. These events are denoted as out-of-time pile-up.
Since MC samples are normally produced before or during the data-taking phase, the pile-up conditions in data can not be modelled perfectly in advance. Therefore, it is necessary to reweight the pile-up conditions in MC to the ones finally found in the ATLAS data. This procedure is done with the ATLAS pile-up reweighting tool [42].

Good Run List

Only data taken periods from the Good Run List (GRL) are used. It is a summary of all the taken data runs where the different detector subsystems operated properly. The GRL can differ between analyses groups, since for different physics signatures different detector subsystems are necessary for their proper reconstruction. For the outlined analysis, the GRL of the standard model group dealing with W/Z+jets processes is used [43].

$\not{E}_{\mathrm{T}}$ Cleaning

For a better $\not{E}_{\mathrm{T}}$ reconstruction, events containing at least one "bad" jet with $p_T > 20$ GeV have to be rejected in both data and MC. "Bad" jets are jets having energy spikes in the hadronic endcap calorimeter or significant noise in the EM calorimeter, or showing indications of originating from non-collision background or cosmic rays. In this analysis the recommended "looser" selection criteria of "bad" jets is used [35].

LAr Hole Treatment

During the 2011 data taking periods E to H, the liquid argon calorimeter performance was affected by a hole in a certain detector region. This hole degraded the jet reconstruction efficiency and as a consequence also the $\not{E}_{\mathrm{T}}$ reconstruction. Therefore an event veto was introduced for the data periods E to H rejecting events containing at least one jet with $p_T > 40$ GeV falling into the affected region. In MC, the same veto was applied for the events representing the data periods E to H.

LAr Error Flag

Events containing noise bursts or data integrity errors in the LAr calorimeter are rejected using the "LArError" event by event bitset.

Modification of Observables in Data and MC

Since the detector description of the MC is not perfect, several quantities need to be corrected in MC and/or data to get a good agreement between data and MC [29,31,40,44–49].

- The electron energy (muon transverse momentum) are smeared in MC to better reproduce the energy (transverse momentum) resolution in data.
- For the following efficiencies, scale factors $SF = \epsilon_{data}/\epsilon_{MC}$ are applied on MC to account for the different efficiencies in MC ϵ_{MC} and data ϵ_{data}.
  - electron reconstruction
  - electron identification
  - muon reconstruction
  - electron trigger
  - muon trigger

– b-tagging

- The electron energy scale is corrected in data by means of a scale factor.

3.4. Data Sample

The Egamma as well as the Muon stream for the ATLAS data recorded in 2011 were analysed. The Egamma (Muon) stream contains events that were triggered by an electron or photon (Muon) trigger. The data corresponds to an integrated luminosity of $\int \mathcal{L}\, dt = 4713.11\ \text{pb}^{-1}$ after accounting for the dedicated Good Run List.

3.5. Signal and Background Samples

Dedicated MC samples for the signal and background processes are essential to derive meaningful limits on the Higgs signal. Table 3.2 illustrates the inclusive cross sections σ_{WH} of the WH production process as well as the branching ratios $BR_{H\to b\bar{b}}$ for Higgs masses m_H from 110 GeV to 130 GeV. As outlined already in Section 1.5, both σ_{WH} as well as $BR_{H\to b\bar{b}}$ decrease with increasing Higgs mass. The WH samples are produced with the Pythia MC generator [8]. They contain only W bosons that decay into electrons, muons or tau leptons.

Table 3.2.: Cross section for the associated WH production σ_{WH} and the branching ratio of the decay $H \to b\bar{b}$ $BR_{H\to b\bar{b}}$ for various Higgs masses m_H at a centre-of-mass energy $\sqrt{s} = 7$ TeV [14].

m_{Higgs} [GeV]	σ_{WH} [pb]	$BR_{H\to b\bar{b}}$
110	0.875	0.745
115	0.755	0.705
120	0.656	0.649
125	0.573	0.578
130	0.501	0.494

The cross section given in Table 3.3 is the effective cross sections σ_{eff}: It takes the filter for one or two leptons during the event generation ino account as well as the K-factor.

The K-factor is a multiplicative factor to scale the sample cross section to next-to-leading order accuracy.
The background components can be summarized into six groups:

- Processes including top quarks, namely $t\bar{t}$ and single top (st) production. The latter contains the s-, t-, and Wt-channel production. The $t\bar{t}$ sample was is produced by the MC@NLO event generator [54]. The single top samples are generated partly by MC@NLO (s- and Wt-channel) and partly by AcerMC (t-channel) [55]. AcerMC was used for the single top t-channel sample due to a problem in the corresponding MC@NLO sample. In the $t\bar{t}$ sample used here, only $t\bar{t}$ pairs with at least one leptonically decaying W boson are present and in the single top samples the W boson has to decay leptonically. In order to not rely on the theoretical MC cross sections for the large top background ($t\bar{t}$ plus single top), the normalization of the top sample is performed as illustrated in Chapter 5.2.

- Processes including a W boson and jets. Events involving b, c, and light flavour (LF) jets have to be considered. ALPGEN [50] produces different samples for different numbers of additional partons. For $W + LF$ ($W + c$), samples from zero up to five (four) additional partons are used. For $W + c\bar{c}$ and $W + b\bar{b}$, the samples contain from zero up to three additional partons.
  These ALPGEN samples contain heavy flavour jets originating from multi-parton interactions, the parton showering process and the hard interaction. Since no ΔR cut is applied between heavy flavour jets produced by the hard interaction, the different samples overlap strongly between each other since a pair of heavy flavour jets with a small distance ΔR can be produced in the hard scatter or in the parton showering process. Therefore, one has to decide, from which sample to take the overlapping events. This decision is done by the Heavy Flavour Overlap Removal Tool (HFOR) [51]. It reorganizes the overlap between the various ALPGEN W+jets samples according to the following philosophy: pairs of heavy flavour jets with a small distance ΔR are to be described by the parton showering process whereas pairs of heavy flavour jets with a large value of ΔR should be described by the hard interaction.
  The ALPGEN W+jets samples contain only leptonically decaying W bosons. Since NLO order effects can have a large influence on the W+jets samples containing heavy flavour quarks [52] and virtual NLO corrections are not considered in the ALPGEN samples, the different flavour fractions are extracted from the data (see Chapter 5.1) as well as the inclusive W+jets background (see Chapter 5.2).

- Processes including a Z boson and jets. Events involving b, c, and LF jets have to be considered. For $Z + jets$, the $Z + c\bar{c}$ and $Z + c$ contribution is taken from the $Z + LF$ samples, in which massless c quarks are produced, since no specific $Z + c\bar{c}$ samples containing massive c quarks were available. The overlap between the $Z+LF$ samples and the $Z + b\bar{b}$ samples is cut out using the HFOR tool. Only leptonically decaying Z bosons are enclosed in the used samples.

- WW diboson production. One of the W boson is forced to decay leptonically into an electron or muon in the given sample. The samples were produced by the Herwig event generator [53].

- WZ diboson production. Only W boson decays into an electron or muon are allowed in the used sample. Produced were these samples by the MC@NLO event generator [54].

- Multijet production. The multijet samples were produced with a filter selecting events with c or b quarks. Besides, the events have to contain an electron or muon with $p_T > 15$ GeV. Despite the quark and lepton filter, the size of the QCD samples are too low to describe the multijet events passing the WH event selection (see Section 3.6) reasonably. Furthermore, the cross section of the multijet production is insufficiently known. Therefore, a data-driven approach for the multijet-background is necessary.

MC@NLO, ALPGEN, PowHeg and AcerMC have to be interfaced to a different MC generator for the parton showering procedure and the underlying event modelling. For the considered MC@NLO, ALPGEN and PowHeg samples, it is done by Herwig together with Jimmy, and for the AcerMC samples with Pythia.

3.6. WH Event Selection

To select events having one isolated charged lepton, $\not{E}_{\mathrm{T}}$ and two b jets in the final state as in the Higgs channel $WH \to l\nu b\bar{b}$, the following cuts and procedures are applied successively on data and MC events:

Table 3.3.: MC generator, K-factor, and effective cross section σ_{eff} at a centre-of-mass energy of $\sqrt{s} = 7$ TeV for the background processes to the Higgs channel $WH \to l\nu b\bar{b}$. For the K-factor of the single top samples, (a), (b), and (c) refers to s-, Wt-, and t-channel, repectively.

process	MC generator	K-factor	σ_{eff} [pb]
$t\bar{t}$	MC@NLO	1.15	90.55 [56]
single top	MC@NLO, AcerMC	1.06 (a), 1.08 (b), 0.87 (c)	38.16 [56]
$W + b\bar{b}$	ALPGEN	1.2	129.7 [57]
$W + c$	ALPGEN	1.2	1097 [57]
$W + LF$	ALPGEN	1.2	31.5×10^3 [57]
$W + c\bar{c}$	ALPGEN	1.2	361.5 [57]
$Z + LF, c, c\bar{c}$	ALPGEN	1.25	3218 [57]
$Z + b\bar{b}$	ALPGEN	1.25	38.73 [56]
WW	Herwig	1.48	17.02 [57]
WZ	MC@NLO	1.0	3.75 [58]
QCD	Pythia	1	187×10^3 [58]

- Pile up reweighting on the MC samples (see Section 3.3) and the selection of data runs having good data quality based on the GRL (see Section 3.3).

- Events with serious LAr calorimeter problems are removed (see Section 3.3).

- Events have to contain at least one reconstructed vertex with at least three tracks.

- Events have to pass the single electron or single muon trigger as outlined in Section 3.1.6.

- The $\not{E}_{\mathrm{T}}$ cleaning cut (see Section 3.3) and the LAr cleaning cut (see Section 3.3) are applied.

- Exactly one signal lepton (electron or muon) as defined in the Sections 3.1.2 and 3.1.1 is required, meaning one signal electron and zero signal muons or zero signal electrons and one signal muon. This leads to an efficient rejection of dileptonic $t\bar{t}$ events, in which one W boson decays leptonically into an electron and the second one leptonically into an muon. Figure 3.2 depicts the number of isolated leptons for the signal and the different background processes. The tight track and calorimeter isolation of the selected leptons rejects the bulk of the multijet background as can be seen in Figure 3.3 for muons and Figure 3.4 for electrons.

To deal with the overlap between the Egamma und Muon stream, the signal electron (muon) is selected from the Egamma (Muon) stream.

- for an even more efficient rejection of the dileptonic $t\bar{t}$ background and the Z+jets background, a dedicated lepton veto is introduced. Events are rejected, if they have:
  - at least three veto leptons as defined in the Sections 3.1.2 and 3.1.1
  - two veto leptons with $p_T > 20$ GeV
  - two oppositely charged veto leptons, where one leptons fulfils $p_T \leq 20$ GeV

  One of the veto leptons represents the signal lepton, that fulfils, of course, the looser criteria of the veto leptons.

- To account for the neutrino in the final state and further reject multijet and Z+jets events, a $\not{E}_{\mathrm{T}}$ of more than 25 GeV is requested. Figure 3.5 shows the $\not{E}_{\mathrm{T}}$ distribution for signal and background.

- To select events containing a leptonically decaying W boson, a M_T of more than 40 GeV is required. The M_T distribution is depicted in Figure 3.6.

- To reconstruct the invariant mass of a pair of b jets, at least two signal jets (see Section 3.1.3) are necessary in the final state. The tight jet cuts on p_T and η are

Figure 3.2.: The distribution of the number of isolated leptons normalized to unity for a Higgs signal ($m_H = 125$ GeV) and the background processes.

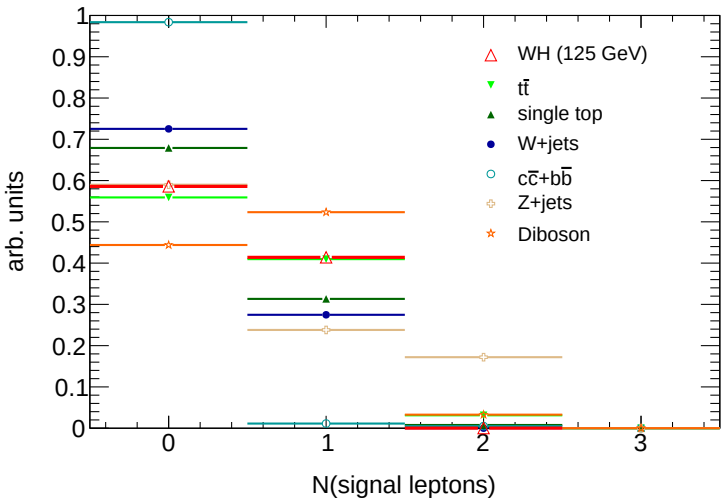

Figure 3.3.: The distribution of the muon calorimeter and track isolation normalized to unity for a Higgs signal ($m_H = 125$ GeV) and the background processes.

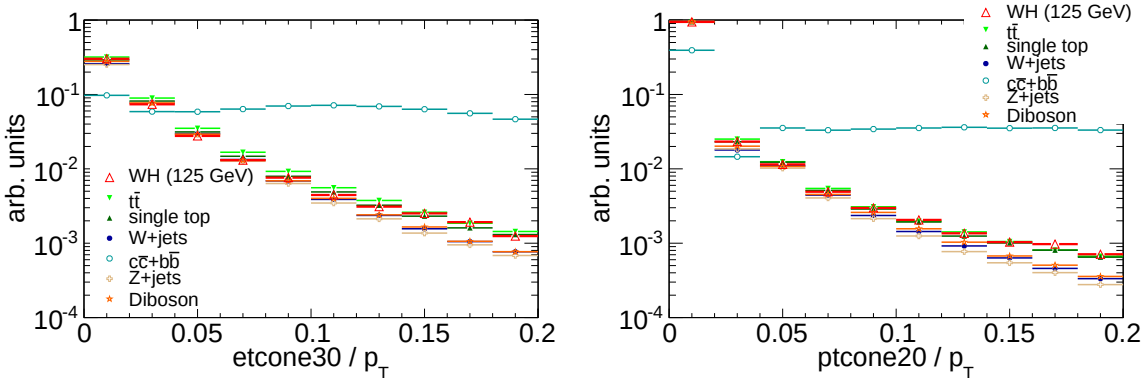

Figure 3.4.: The distribution of the electron calorimeter and track isolation normalized to unity for a Higgs signal ($m_H = 125$ GeV) and the background processes.

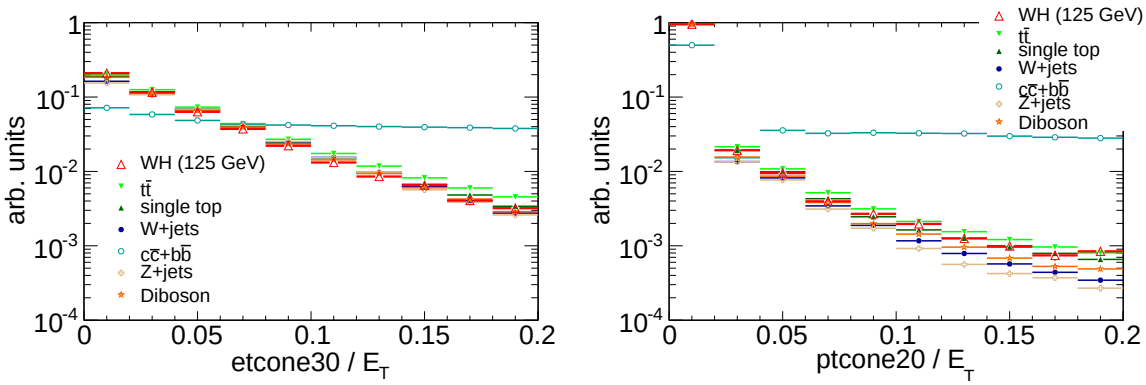

necessary for the later b-tagging step. Since the number of $t\bar{t}$ events increases significantly from two to three signal jets as can be seen in Figure 3.7, a cut on exactly two jets is applied.

- The veto jet definition can not be applied for our signal jets since b-tagging is only applicable in the fiducial volume of the inner detector ($\eta < 2.5$). Nonetheless, a veto cut can be introduced requiring that no further veto jet beside the two signal jets is to be present in the event. This reduces further the large background from $t\bar{t}$.

- Figure 3.8 demonstrates the MV1 b-tag weight W_{jet} for all signal jets present in the selected sample. A cut $W_{jet} > 0.601713$ corresponding to a b-tag efficiency of 70% for $t\bar{t}$ is chosen (see Section 3.2). To reduce the $W + LF$, $W + c$ and $W + c\bar{c}$ background to a manageable size, it is essential to apply the b-tag cut to both signal jets. The number of b-tagged jets for the different samples is shown in Figure 3.9.

Figure 3.5.: The $\not{E}_{\mathrm{T}}$ distribution normalized to unity for a Higgs signal ($m_H = 125$ GeV) and the background processes.

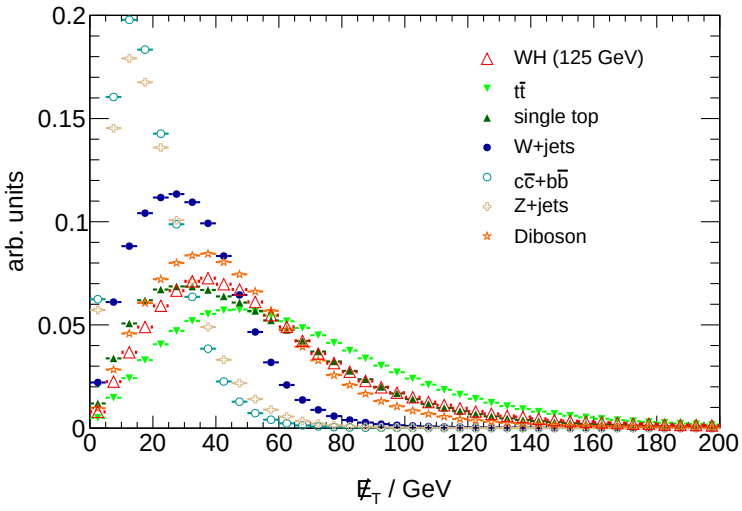

Figure 3.6.: The M_T distribution normalized to unity for a Higgs signal ($m_H = 125$ GeV) and the background processes.

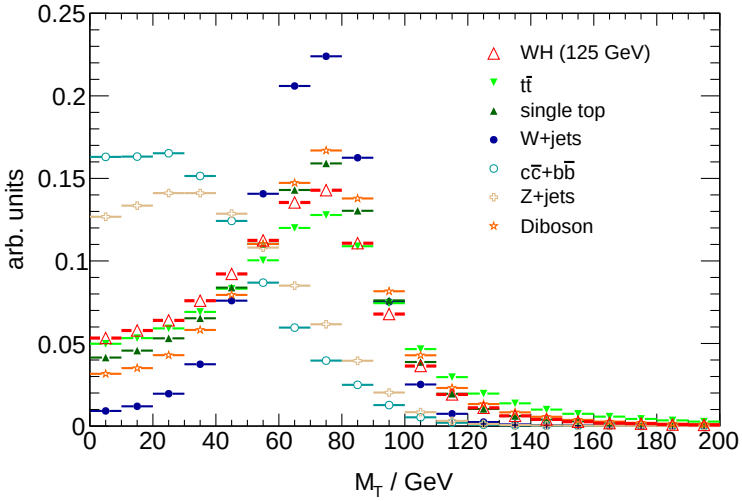

Figure 3.7.: The distribution of the number of signal jets normalized to unity for a Higgs signal ($m_H = 125$ GeV) and the background processes.

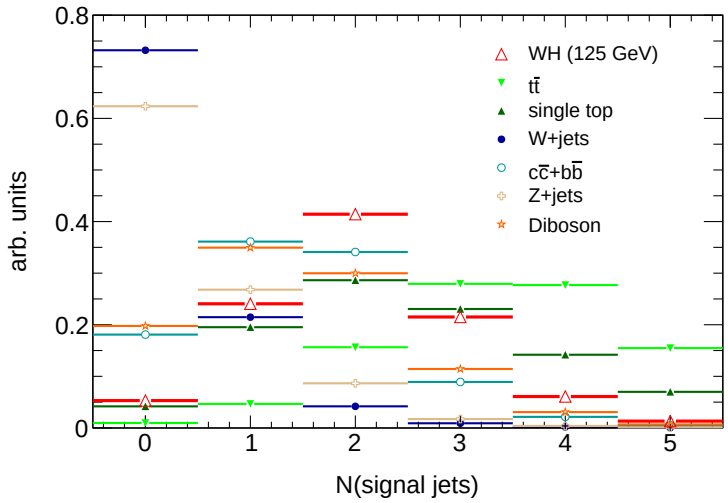

- Finally, $p_T > 45$ GeV is required for one of the two b-tagged jets, besides a cut $\Delta R > 0.7$ between the two b-tagged jets for the region $p_T^W \leq 200$ GeV. These cuts further improve the background rejection and the S/B ratio. For the range $p_T^W > 200$ GeV, the Higgs is considerably boosted leading to small ΔR values. Therefore the ΔR is only applied for $p_T^W \leq 200$ GeV. Figure 3.10 illustrates the $m_{b\bar{b}}$ distribution normalized to unity: The Higgs signal ($m_H = 125$ GeV) sample dominates the range $80 \leq m_{b\bar{b}} \leq 150$ GeV. This region is therefore called the Higgs signal region. The W+jets (top) background is broader distributed and favours the lower (higher) $m_{b\bar{b}}$-regions. These sidebands are used for the background normalization in Section 5.

As mentioned already in Section 3.1.7, the $m_{b\bar{b}}$ distribution of events surviving all cuts is finally classified in several p_T^W bins: The first covers the range $p_T^W < 50$ GeV, the second $50 \leq p_T^W < 100$ GeV, the third $100 \leq p_T^W < 200$ GeV and the fourth $p_T^W \geq 200$ GeV. The reason for this p_T^W splitting is the steeper falling p_T^W distribution for the background compared to the WH Higgs signal (see Figure 3.11).

Figure 3.8.: The distribution of the MV1 b-tag weight normalized to unity for a Higgs signal ($m_H = 125$ GeV) and the background processes.

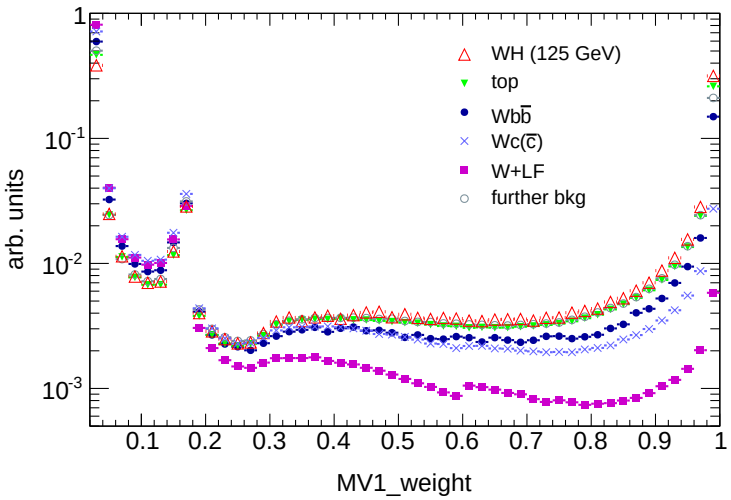

Figure 3.9.: The distribution of the number of b-tagged jets normalized to unity for a Higgs signal ($m_H = 125$ GeV) and the background processes.

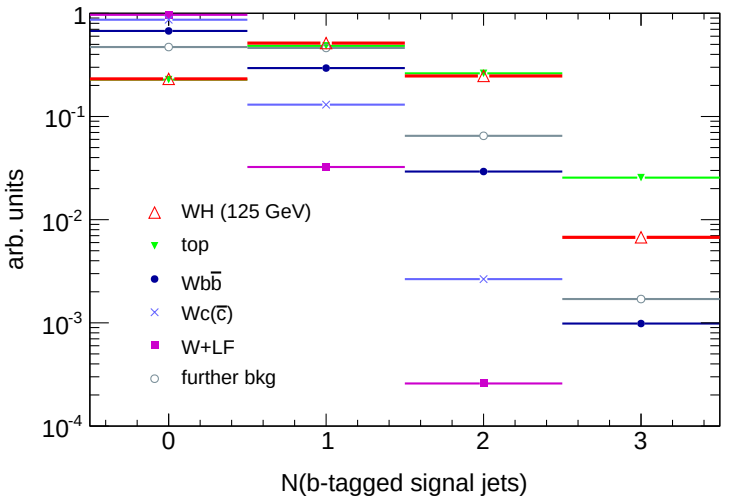

Figure 3.10.: The distribution of the invariant mass $m_{b\bar{b}}$ normalized to unity for a Higgs signal ($m_H = 125$ GeV) and the background processes.

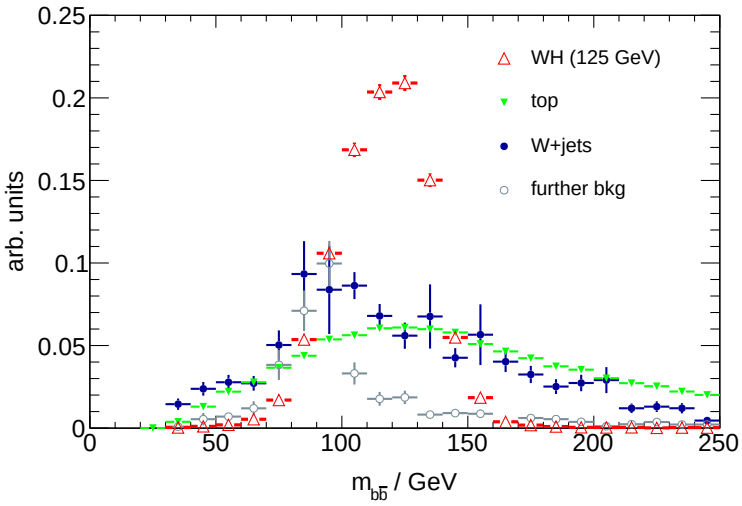

Figure 3.11.: The distribution of the transverse momentum of the W boson p_T^W normalized to unity for a Higgs signal ($m_H = 125$ GeV) and the background processes.

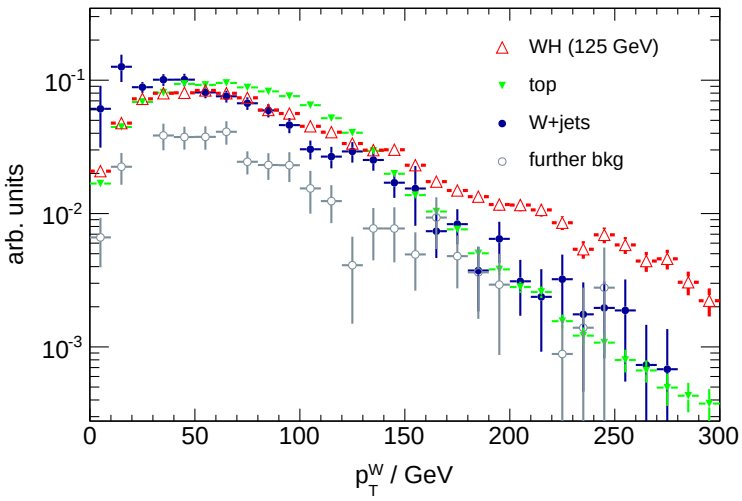

4. Data-Driven Estimate of the Multijet Background

If the description of the multijet background relied on simulated data, huge samples would be needed due to the low probability of a jet to fake an isolated lepton. Furthermore, the theoretical cross sections of MC multijet samples have large uncertainties. Besides, it is very challenging to simulate the process of a jet that fakes a lepton correctly. Therefore, a data-driven method is developed to estimate the multijet contribution to the background of the presented WH analysis.

4.1. The Anti-Isolation Model

The method is motivated by a technique for a data-driven estimate of the multijet background for the W+jets cross section measurement in the muon channel on the ATLAS 2010 dataset [59].
This approach, adjusted to the needs of the WH analysis, uses a template fit to the data distribution of the $\not{E}_{\mathrm{T}}$ in data. One template is the $\not{E}_{\mathrm{T}}$ distribution in a multijet modelling region (MMR) derived from data, the second template is derived from MC and consists of the $\not{E}_{\mathrm{T}}$ contributions from the non-multijet background components (non-MJ), i.e. top, W+jets, Z+jets, WW, and WZ, in the signal region (SR) as outlined in Section 3.1.
To get a multijet description that is as close as possible to the multijet background after all selection cuts, most of the cuts are applied before the $\not{E}_{\mathrm{T}}$ template fit. Only the $\not{E}_{\mathrm{T}}$ and M_T cut are dropped and are applied after the template fit, since the cuts on $\not{E}_{\mathrm{T}}$ and M_T reject the bulk of the multijet background.
The MMR is derived by applying all WH selection cuts (except the $\not{E}_{\mathrm{T}}$ and M_T cuts) to the full 2011 dataset with the following modifications: Dedicated lepton quality criteria, e.g. the lepton isolation, are modified or fully reversed to get mainly jets reconstructed

as leptons instead of real leptons originating from the leptonic W decay. For the electron channel, besides the two jet events also three jet events are considered (see Section 4.1.2). The MMR selection is furthermore applied to the non-multijet background MC samples to subtract these contributions from the data in the MMR.
The fit of the MMR template and the non-MJ template to the SR data $\not\!\!E_{\mathrm{T}}$ distribution is done by the ROOT TFractionFitter method [23]. It is based on the fitting techniques for finite MC samples suggested in [60]. The main aspects of the fitting technique are outlined in Appendix A. The fit parameters are scaling factors for both templates, SF_{MMR} and $SF_{\text{non-MJ}}$. Since the top and W+jets background are constrained in more dedicated distributions (see Section 5), $SF_{\text{non-MJ}}$ does not enter the final results but is tested for consistency in Section 5.3. In contrast, SF_{MMR} allows a multijet estimate MJ in the signal region SR by scaling all distributions generated in the MMR to the SR: $\mathrm{MJ}_{\mathrm{SR}} = \mathrm{MJ}_{\mathrm{MMR}} \times SF_{\mathrm{MMR}}$.
To receive a multijet estimate MJ after *all* selection cuts, one finally needs to apply the cuts on $\not\!\!E_{\mathrm{T}}$ and M_T in the MMR. These cuts were dropped for the fraction fit.

4.1.1. Multijet Background in the Muon Channel

In the muon channel, the enrichment of multijet events in the MMR is done by reversing the track and calorimeter isolation cuts of the signal muon, i.e. $|ptcone20/p_T| \leq 0.1$ and $|etcone30/p_T| \leq 0.14$. Figure 3.3 in Section 3.1 illustrates that the bulk of non-isolated muons originate from multijet events.
The MMR $\not\!\!E_{\mathrm{T}}$ template is depicted in Figure 4.1 before and after subtracting the non-multijet component. The relative difference between the MMR $\not\!\!E_{\mathrm{T}}$ template before and after the subtraction (relative contamination), which is normalized to the MMR $\not\!\!E_{\mathrm{T}}$ template before the subtraction, is shown on the right plot in Figure 4.1: In the high statistics $\not\!\!E_{\mathrm{T}}$ range from 0 to 70 GeV, the relative contamination is low and increases from ~ 0 % to ~ 5 %; in the low statistics range for $\not\!\!E_{\mathrm{T}} > 70$ GeV, it reaches values up to $\sim 20\%$. Therefore the $\not\!\!E_{\mathrm{T}}$ fit is performed only in the range between 0 GeV and 70 GeV. This restriction holds only for the fit range but not for the kinematic distributions itself.
The data $\not\!\!E_{\mathrm{T}}$ distribution in the signal region together with the two fitted templates and their resulting $\not\!\!E_{\mathrm{T}}$ distribution is shown in Figure 4.2. The MMR $\not\!\!E_{\mathrm{T}}$ distribution is scaled down by a factor $SF_{\mathrm{MMR}} = 0.37 \pm 0.03$, whereas the non-MJ $\not\!\!E_{\mathrm{T}}$ distribution is scaled up by $SF_{\text{non-MJ}} = 1.10 \pm 0.05$.

Figure 4.1.: For the muon channel: The $\not\!\!E_T$ template of the multijet modelling region MMR before and after subtraction of the non-multijet contribution (left figure). The relative contamination of the MMR $\not\!\!E_T$ template by non-multijet components normalized to the MMR $\not\!\!E_T$ template before the subtraction (right figure).

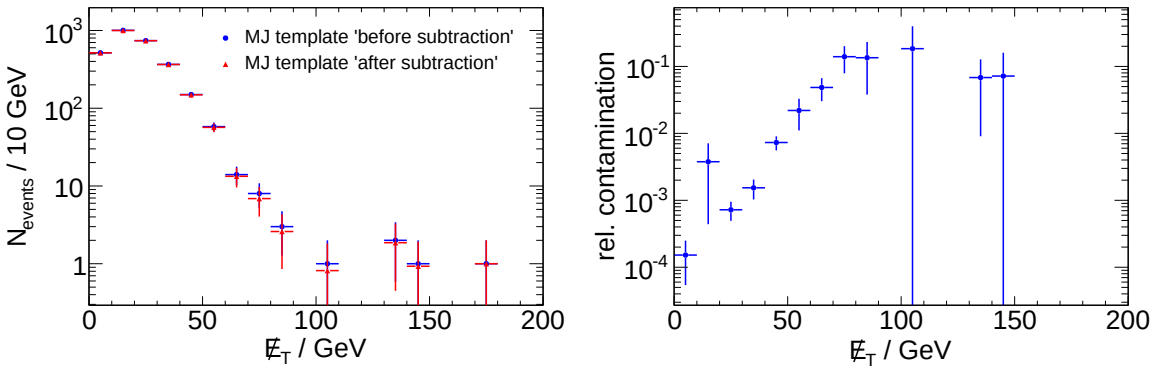

4.1.2. Multijet Background in the Electron Channel

As for the muon channel, in the electron channel the track and calorimeter isolation of the signal electron were reversed to get an enrichment of multijet events in the MMR. Furthermore, the hadronic leakage cut, a quality criterion of the electron identification (see Section 3.1.2) responsible for the rejection of electron candidates that reach too far in the hadronic calorimeter is reversed. This leads to a further enhancement of hadronic objects that can be misidentified as electrons. Since for the overlap removal between jets

Figure 4.2.: For the muon channel: The $\not\!\!E_T$ distribution in data in the signal region, the fitted multijet and non-multijet $\not\!\!E_T$ templates and the result of the fit of both templates.

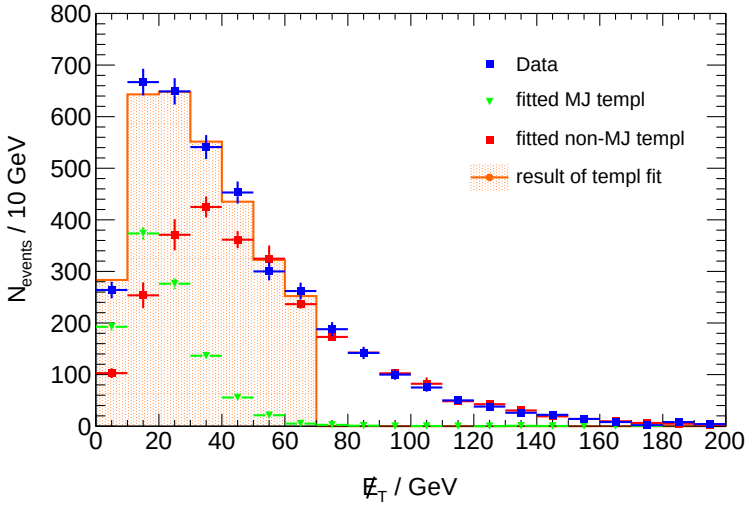

and electrons the isolation criteria are imposed on the electrons, anti-isolated electrons of the MMR could overlay with the two selected b-tagged jets. This overlap leads to a wrong kinematic description of the MJ background, since one of the two b-tagged jets can be considered as signal jet and signal lepton at the same time. To prevent this overlap, an additional cut between the anti-isolated electrons and jets is introduced: If the distance between either of the two b-tagged jets and the anti-isolated electron is smaller than $\Delta R = 0.4$, the electron is rejected. Unfortunately, this additional cut removes most of the events in the MMR. To improve the statistics in the MMR, the requirement on the number of jets was modified from exactly two to two or three jets. The third jet should be interpreted as a misidentified electron and has therefore to overlap with the anti-isolated electron within $\Delta R = 0.4$. Furthermore, the third jet has to be a non-b-tagged jet to prevent confusion between the two b-tagged signal jets and the misidentified electron. Since the kinematics of the MMR three jet events should be as close a possible to the SR two jet events, the distance between the light jet and the closest b-tagged jet is $\Delta R = 2.8$ at maximum. This value is motivated by a satisfying kinematical description of the MJ background in a multijet enriched control region (see Section 4.2).
In analogy to Section 4.1.1, Figure 4.3 depicts the raw and cleaned MMR $\not{E}_{\mathrm{T}}$ template together with the relative contamination and Figure 4.4 shows the result of the fit. The relative contamination increases in the high statistics range $\not{E}_{\mathrm{T}} < 80$ GeV from ~ 0 % to ~ 15 %. The same fit range as in the muon channel is chosen ($\not{E}_{\mathrm{T}} < 70$ GeV) to have a maximum relative contamination of ~ 10 %. Compared to the muon channel, the MMR $\not{E}_{\mathrm{T}}$ template has a lower number of events. The scaling factors are $SF_{\mathrm{MMR}} = 1.41 \pm 0.08$ and $SF_{\text{non-MJ}} = 0.94 \pm 0.05$.

Figure 4.3.: For the electron channel: The $\not{E}_{\mathrm{T}}$ template of the multijet modelling region MMR before and after subtraction of the non-multijet contribution (left figure). The relative contamination of the MMR $\not{E}_{\mathrm{T}}$ template by non-multijet components normalized to the MMR $\not{E}_{\mathrm{T}}$ template before the subtraction (right figure).

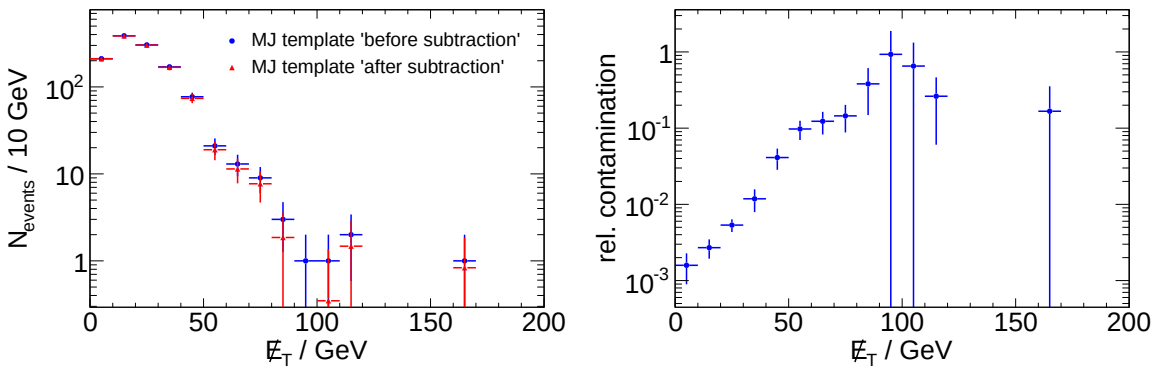

Figure 4.4.: For the electron channel: The $\not\!\!E_{\mathrm{T}}$ distribution in data in the signal region, the fitted multijet and non-multijet $\not\!\!E_{\mathrm{T}}$ templates and the result of the fit of both templates.

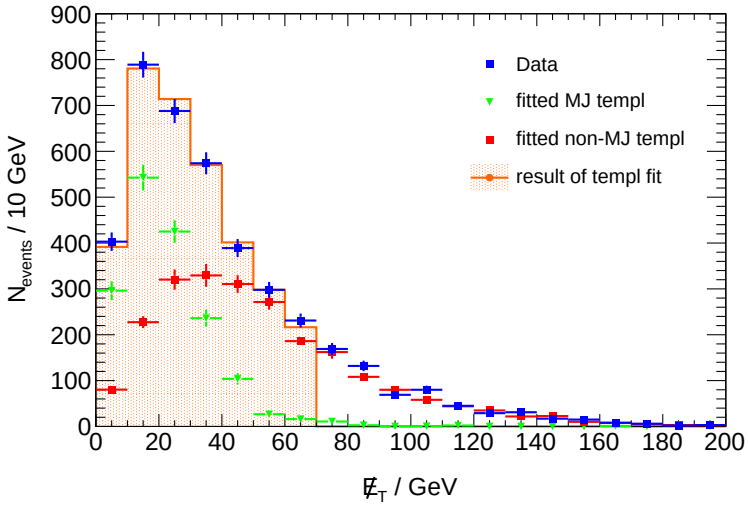

4.2. Validation of the Method in a Multijet-Enriched Control Region

To test the method for a multijet estimate described in the previous section and evaluate a systematic uncertainty on it, a multijet enriched control region CR is defined by applying the analysis cuts as outlined in Section 3.1 except for inverting the cuts on $\not\!\!E_{\mathrm{T}}$ and M_T: $\not\!\!E_{\mathrm{T}} < 25$ GeV and $M_T < 40$ GeV.

Figure 4.5 (4.6) depicts kinematic distributions of jets in the CR for the muon (electron) channel, i.e. the η, ϕ and p_T distributions of the leading and next-to-leading jet, and the distance ΔR between the two jets. The notations "leading" and "next-to-leading" refer to the p_T of the jet. The figures show the data distribution in the CR together with the total background prediction consisting of the data-driven multijet estimate together with the MC prediction for the non-MJ backgrounds. For both channels, the description of the jet variables looks satisfying since the data agree with the background prediction within the statistical uncertainties.

The $m_{b\bar{b}}$ distribution for the muon (electron) channel feature a decent agreement between the data and the background expectation. The corresponding distributions are shown in Figure 4.8a (4.9a). As function of p_T^W however, only in the lowest p_T^W bin (the lowest and next-to-lowest p_T^W bin) the background prediction meets the $m_{b\bar{b}}$ data distribution for the muon (electron) channel (see Figure 4.7 (4.8)). Therefore, a systematic uncertainty

of 100% is assigned on the MJ estimate for the second to the fourth (the third and the fourth) p_T^W bin of the $m_{b\bar{b}}$ distribution for the muon (electron) channel. For the first (first and second) p_T^W bin, the absolute value of the relative difference between the background prediction and the data distribution is investigated. The relative difference is normalized to the background prediction. These deviations, that are interpreted as (symmetric) systematic uncertainties in the following, are shown in Figure 4.9 (4.10 and 4.11) for the muon (electron) channel, and a polynomial (degree 0) is fitted to the deviations. Only the signal range 70 GeV $\leq m_{b\bar{b}} <$ 150 GeV is considered. The fitting results are listed in Table 4.1. As a conservative approach, the statistical uncertainties of the fits are added to the corresponding fit values to estimate the systematic uncertainties in the studied p_T^W bins: 24% for the first bin in the muon channel and 39% (35%) for the first (second) bin in the electron channel.

Figure 4.5.: The η, ϕ, p_T, and ΔR distribution(s) of the leading and next-to-leading jet in the multijet control region ($\not{E}_{\mathrm{T}} \leq 25$ GeV, $M_T \leq 40$ GeV) in the muon channel. Depicted are the data distributions together with the background predictions consisting of the data-driven multijet estimate and the MC expectations for the non-multijet backgrounds. The yellow band illustrates the uncertainty on the background due to the limited statistics of the samples.

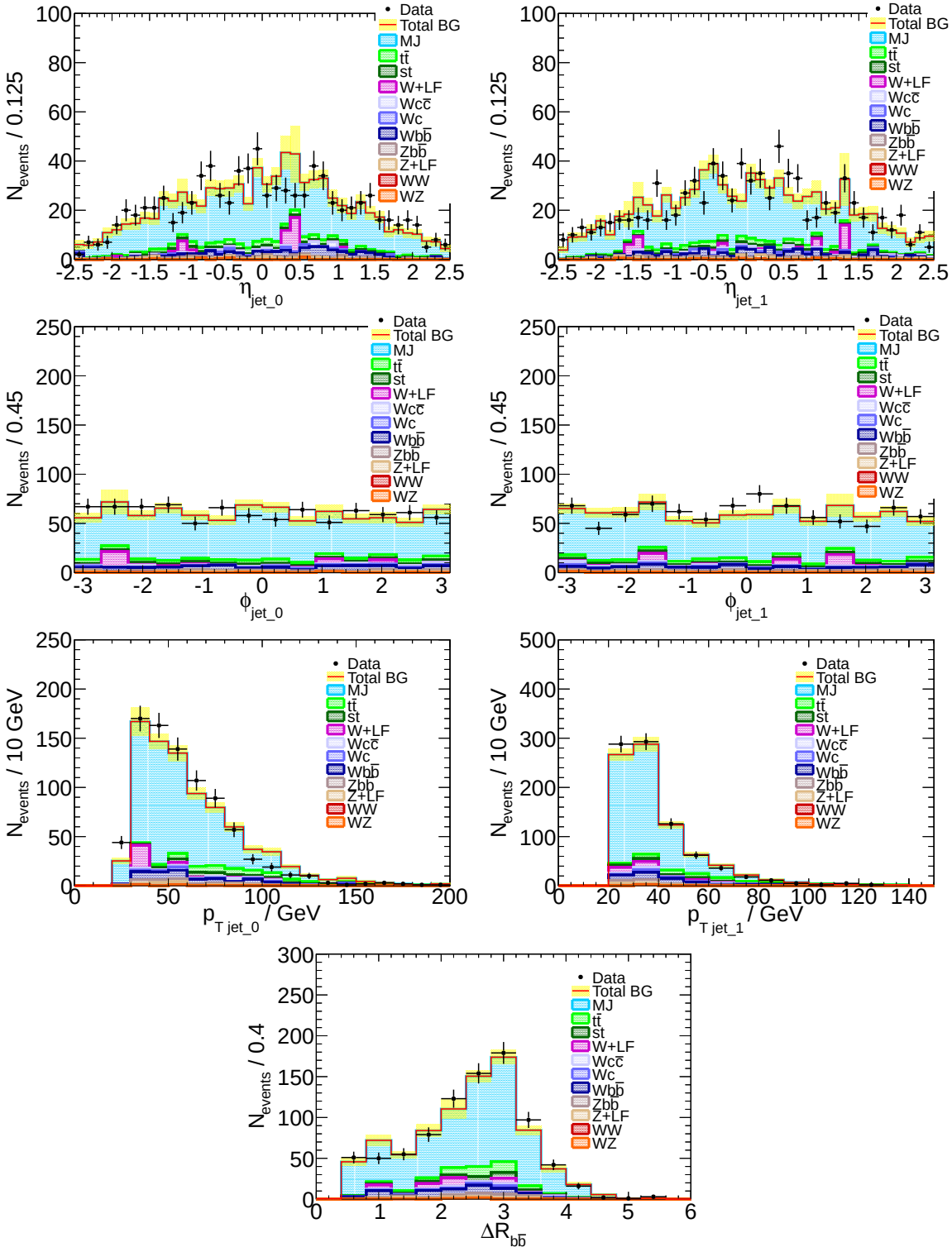

Figure 4.6.: The η, ϕ, p_T, and ΔR distribution(s) of the leading and next-to-leading jet in the multijet control region ($\not\!\!E_{\mathrm{T}} \leq 25$ GeV, $M_T \leq 40$ GeV) in the electron channel. Depicted are the data distributions together with the background predictions consisting of the data-driven multijet estimate and the MC expectations for the non-multijet backgrounds. The yellow band illustrates the uncertainty on the background due to the limited statistics of the samples.

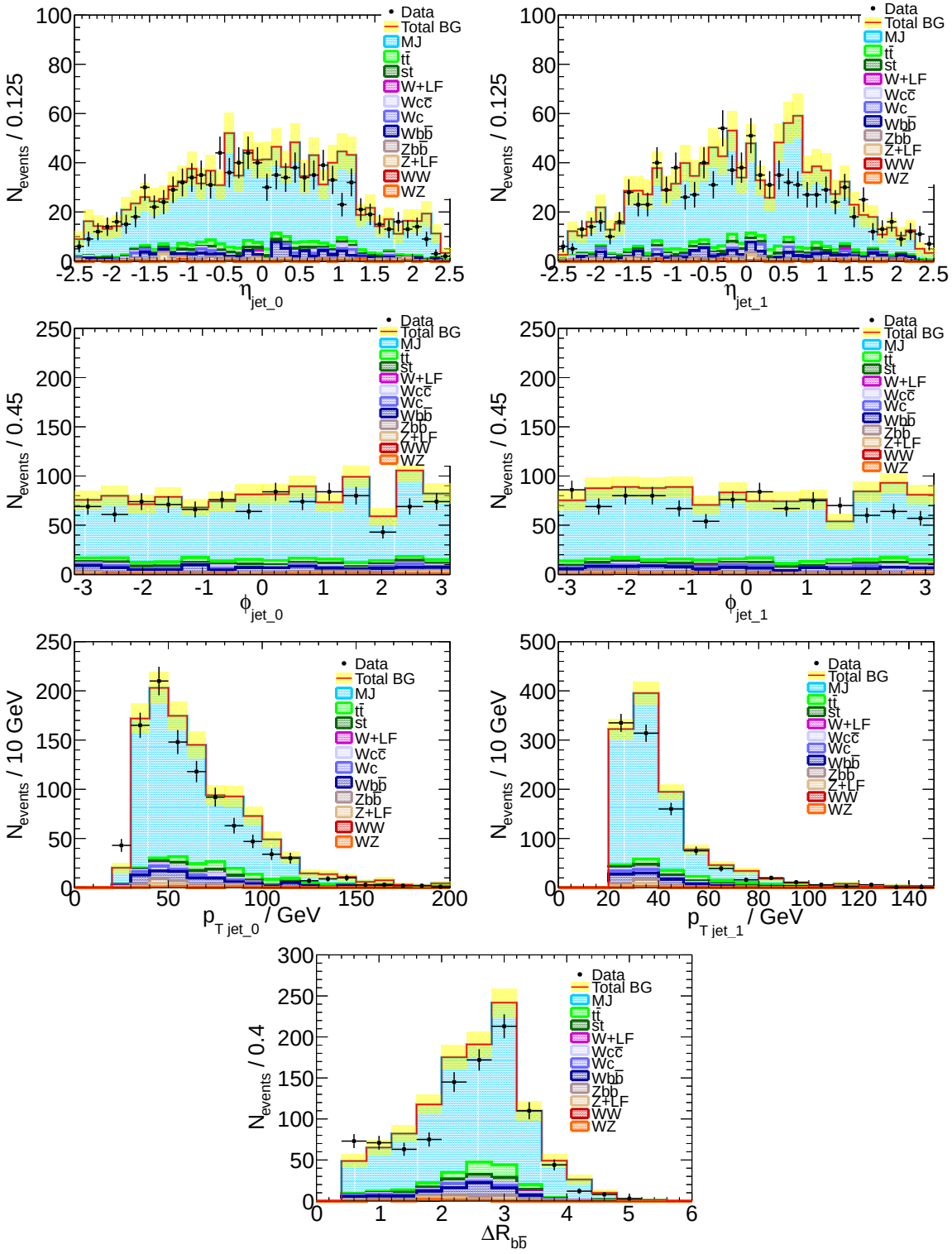

Figure 4.7.: The invariant mass $m_{b\bar{b}}$ of the two b-tagged jets in the multijet control region ($\not{E}_{\mathrm{T}} \leq 25$ GeV, $M_T \leq 40$ GeV) in the muon channel. The events are shown before (a) and after (b-e) splitting into four different p_T^W bins. The yellow band illustrates the uncertainty on the background due to the limited statistics of the samples.

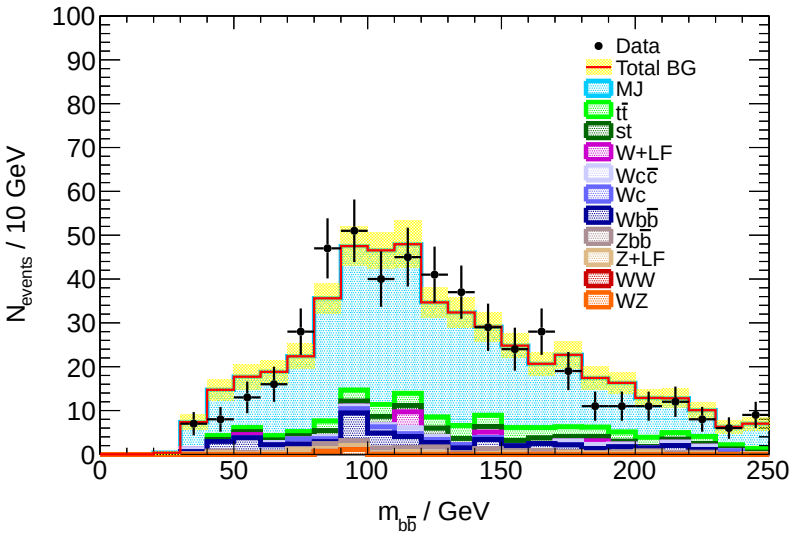

(a) no p_T^W splitting

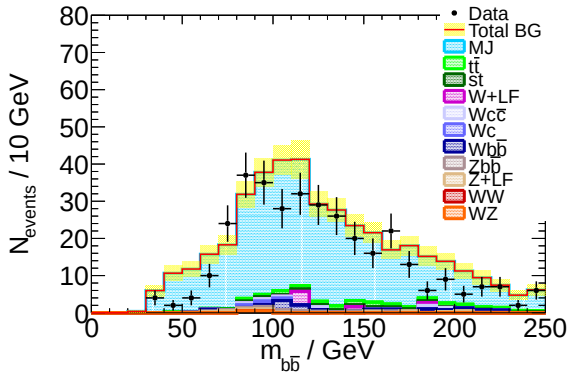

(b) $p_T^W < 50$ GeV

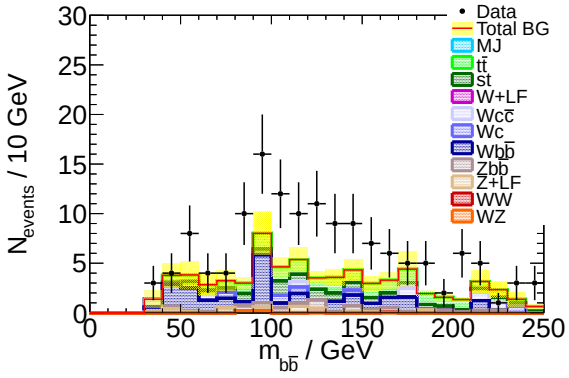

(c) 50 GeV $\leq p_T^W < 100$ GeV

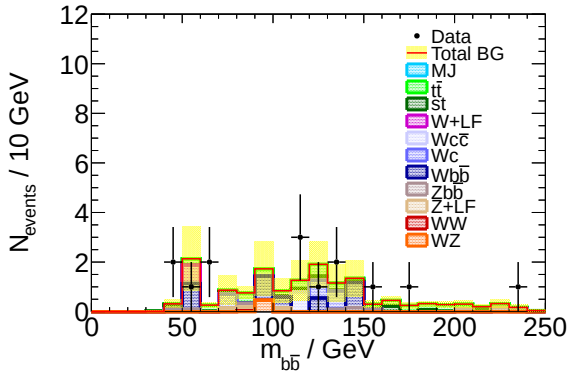

(d) 100 GeV $\leq p_T^W < 200$ GeV

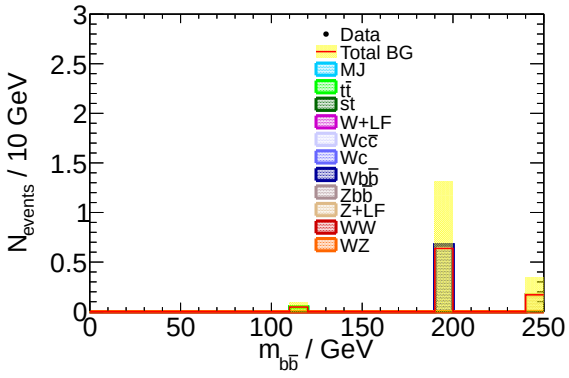

(e) 200 GeV $\leq p_T^W$

Figure 4.8.: The invariant mass $m_{b\bar{b}}$ of the two b-tagged jets in the multijet control region ($\not{E}_{\mathrm{T}} \leq 25$ GeV, $M_T \leq 40$ GeV) in the electron channel. The events are shown before (a) and after (b-e) splitting into four different p_T^W bins. The yellow band illustrates the uncertainty on the background due to the limited statistics of the samples.

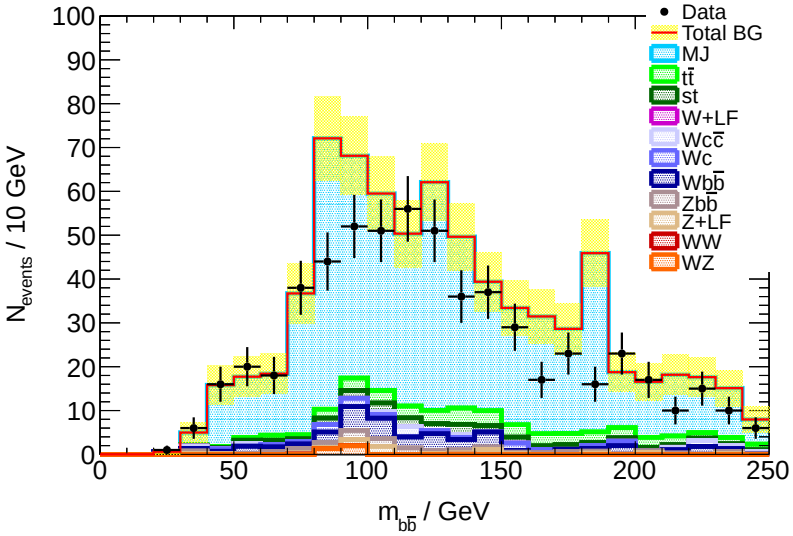

(a) no p_T^W splitting

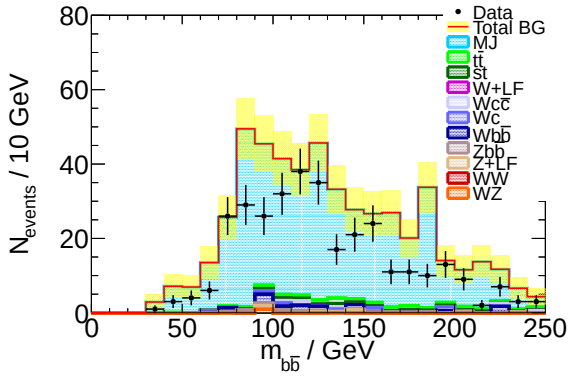

(b) $p_T^W < 50$ GeV

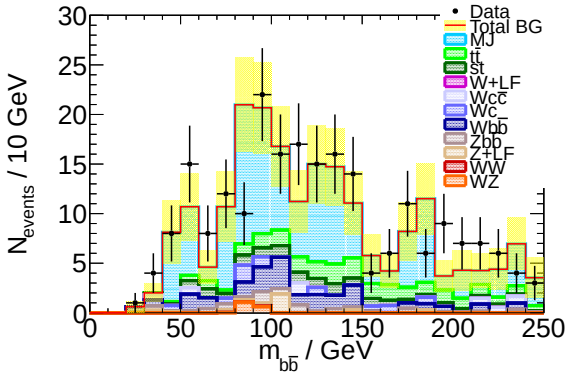

(c) 50 GeV $\leq p_T^W < 100$ GeV

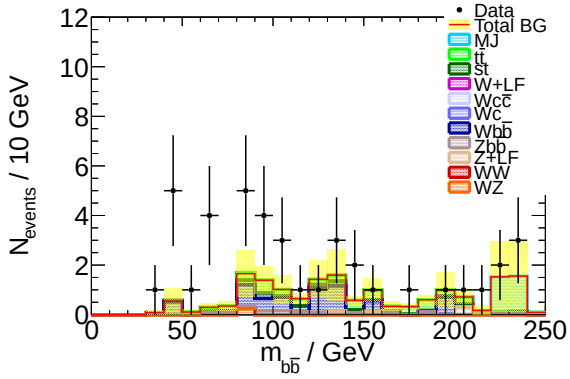

(d) 100 GeV $\leq p_T^W < 200$ GeV

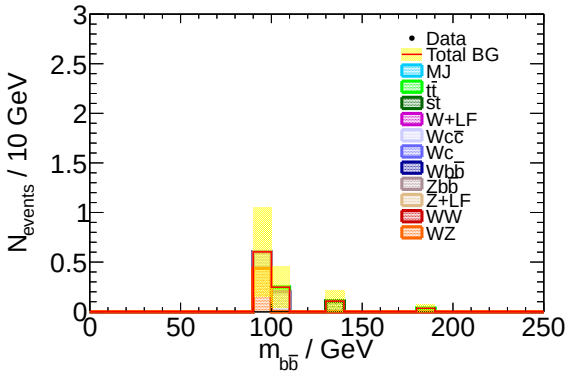

(e) 200 GeV $\leq p_T^W$

Figure 4.9.: The absolute value of the relative difference between the data and the background expectation as function of $m_{b\bar{b}}$ in the multijet control region ($\not{E}_{\mathrm{T}} \leq 25$ GeV, $M_T \leq 40$ GeV) for the first p_T^W bin ($p_T^W < 50$ GeV) in the muon channel. The relative difference is normalized to the background prediction. The additional line is the fit of a polynomial (degree 0).

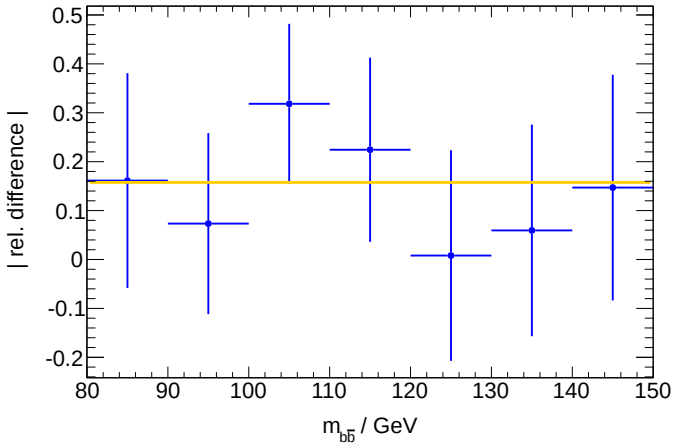

Figure 4.10.: The absolute value of the relative difference between the data and the background expectation as function of $m_{b\bar{b}}$ in the multijet control region ($\not{E}_{\mathrm{T}} \leq 25$ GeV, $M_T \leq 40$ GeV) for the first p_T^W bin ($p_T^W < 50$ GeV) in the electron channel. The relative difference is normalized to the background prediction. The additional line is the fit of a polynomial (degree 0).

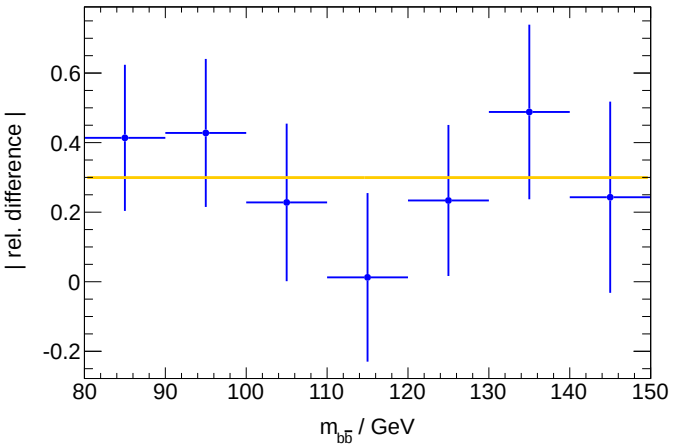

Figure 4.11.: The absolute value of the relative difference between the data and the background expectation as function of $m_{b\bar{b}}$ in the multijet control region ($\not{E}_{\mathrm{T}} \leq 25$ GeV, $M_T \leq 40$ GeV) for the second p_T^W bin (50 GeV $\leq p_T^W <$ 100 GeV) in the electron channel. The relative difference is normalized to the background prediction. The additional line is the fit of a polynomial (degree 0).

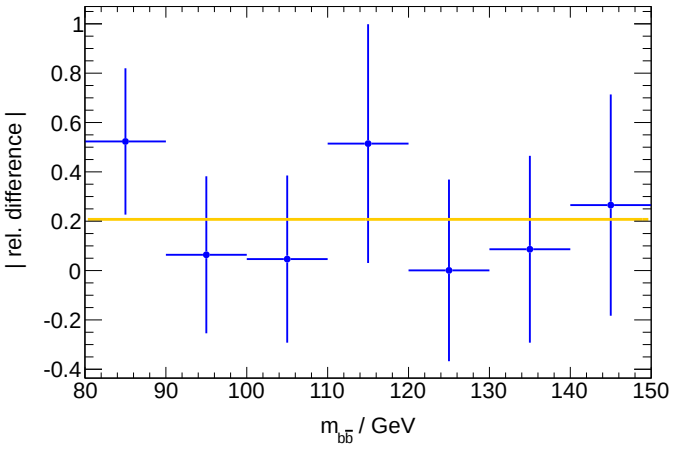

Table 4.1.: Result of the fit of a polynomial (degree 0) to the absolute value of the relative difference between the data and the background prediction in the $m_{b\bar{b}}$ distribution for different p_T^W bins.

p_T^W bin	value	uncertainty
$p_T^W < 50$ GeV (muon channel)	0.16	0.08
$p_T^W < 50$ GeV (electron channel)	0.30	0.09
50 GeV $\leq p_T^W <$ 100 GeV (electron channel)	0.21	0.14

4.3. Multijet Background before the b-Tagging Stage

The normalizations of the W+jets flavour fractions, which are explained in Section 5.1, are determined before the b-tagging stage. Since the multijet estimate that was discussed so far refers to the analysis after the b-tagging, a further estimate needs to be performed before the b-tagging stage.
For the muon channel, the same strategy as outlined in Section 4.1.1 is chosen except for the fact that no b-tag cuts were required for the two selected jets. The MMR $\not{E}_{\mathrm{T}}$ template together with the relative contamination of non-multijet background is shown in Figure 4.12. As for the b-tagged case, the relative contamination increases in the range 0 GeV $\leq \not{E}_{\mathrm{T}} <$ 70 GeV from $\sim$ 0 % to $\sim$ 5 %. Therefore, the same range (0 GeV $\leq \not{E}_{\mathrm{T}} <$ 70 GeV) is used for the fit. Figure 4.13 depicts the results of the template fit. The sum of the two scaled templates agrees well with the data $\not{E}_{\mathrm{T}}$ distribution. For the determination of the W+jets flavour fractions, a fit to the data distribution of the JetCombNN and the IP3DSV1 b-tag weight is done (see Section 5.1). To get an idea of the quality of the multijet estimate for these variables, Figure 4.16 shows the background prediction and the data distributions in the multijet control region ($\not{E}_{\mathrm{T}} \leq$ 25 GeV, $M_T \leq$ 40 GeV). The background is slightly overestimated for large values of both b-tag weights indicating that the defined MMR contains slightly too many heavy flavour events. A shape systematic is evaluated for these discrepancies fitting a polynomial (degree 1) to the absolute values of the relative difference between the data and the background distribution (see Figure 4.18). The fit parameters are listed in Table 4.2.
For the electron channel, besides omitting the b-tagging the MMR is further modified to reach a satisfying multijet description: Only two jet events are considered in the MMR. In addition, the electron isolation cuts for the MMR are not reversed, but are applied as in the signal region. This means, that the enrichment of multijet events in the MMR is only based on the reversal of the hadronic leakage cut of the electron identification. This leads to an increased contamination with non-MJ background and a decreased statistics of the MMR as illustrated in Figure 4.14. Therefore, only the range 0 GeV $\leq \not{E}_{\mathrm{T}} <$ 40 GeV is used for the fit, in which the relative contamination increases already up to $\sim$ 30 %. The result of the fit of both $\not{E}_{\mathrm{T}}$ templates gives a proper agreement with the data $\not{E}_{\mathrm{T}}$ distribution (see Figure 4.15). Due to the modification of the electron definition of the MMR, the background prediction and the data show a satisfying agreement in the multijet CR for the JetCombNN and the IP3DSV1 b-tag weight as shown in Figure 4.17. As done for the muon channel, a linear shape systematic is calculated for the relative discrepancies between data and background prediction for the considered b-tag weights (see Figure 4.19

and Table 4.2).

Figure 4.12.: For the muon channel: The $\not\!\!E_T$ template of the multijet modelling region MMR before and after subtraction of the non-multijet contribution (left figure). The relative contamination of the MMR $\not\!\!E_T$ template by non-multijet components normalized to the MMR $\not\!\!E_T$ template before the subtraction (right figure). No b-tagging is applied here.

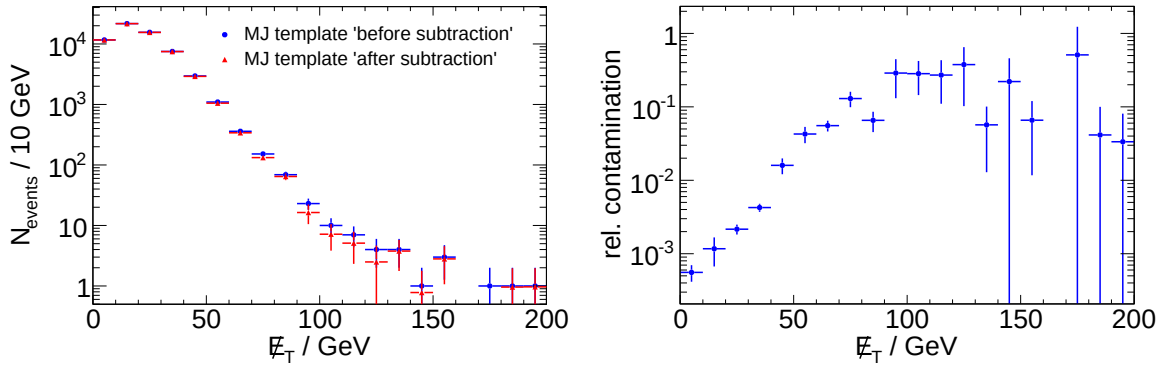

Figure 4.13.: The $\not\!\!E_T$ distribution in data in the signal region, the fitted multijet and non-multijet $\not\!\!E_T$ templates and the result of the fit of both templates in the muon channel. No b-tagging is applied here.

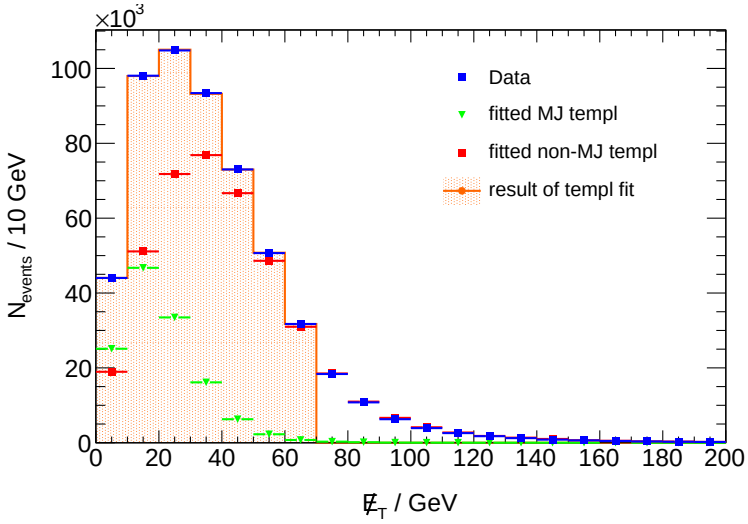

Figure 4.14.: For the electron channel: The $\not\!\!E_T$ template of the multijet modelling region MMR before and after subtraction of the non-multijet contribution (left figure). The relative contamination of the MMR $\not\!\!E_T$ template by non-multijet components normalized to the MMR $\not\!\!E_T$ template before the subtraction (right figure). No b-tagging is applied here.

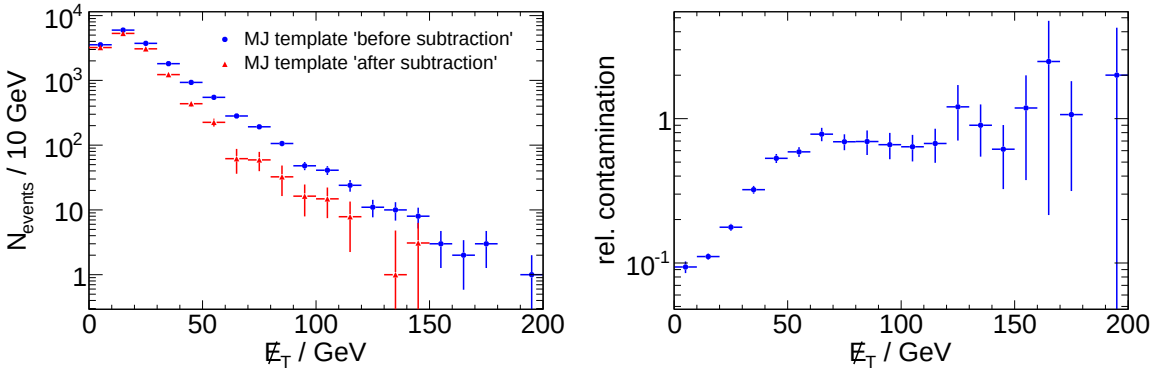

Figure 4.15.: The $\not\!\!E_T$ distribution in data in the signal region, the fitted multijet and non-multijet $\not\!\!E_T$ templates the result of the fit of both templates in the electron channel. No b-tagging is applied here.

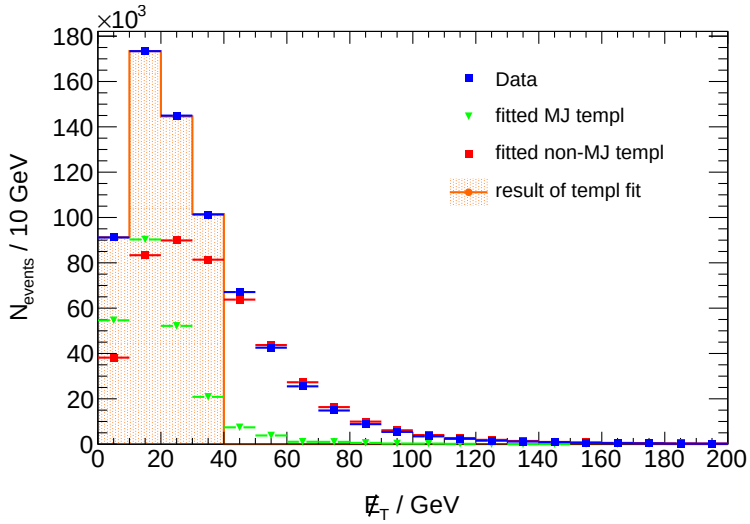

Figure 4.16.: For the muon channel: The distribution of the sum of the b-tag weights of leading and next-to-leading jet for two different tagging algorithms in the multijet control region ($\not\!\!E_{\mathrm{T}} \leq 25$ GeV, $M_T \leq 40$ GeV).

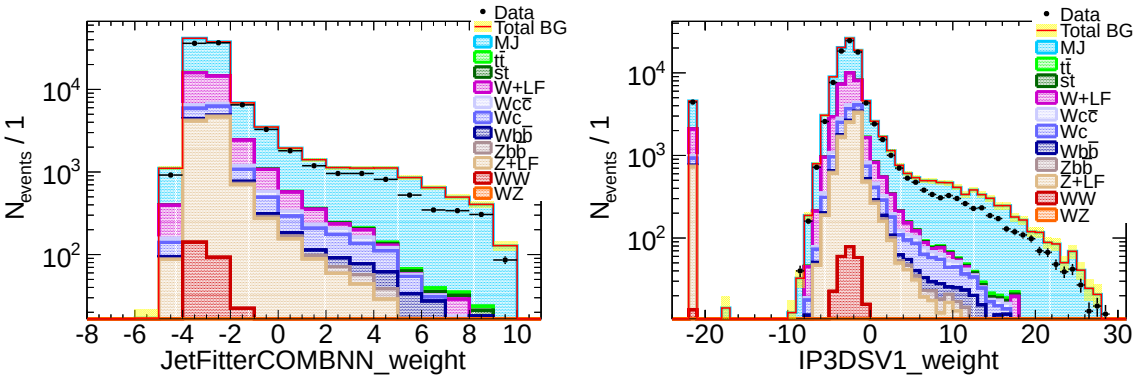

Figure 4.17.: For the electron channel: The distribution of the sum of the b-tag weights of leading and next-to-leading jet for two different tagging algorithms in the multijet control region ($\not\!\!E_{\mathrm{T}} \leq 25$ GeV, $M_T \leq 40$ GeV).

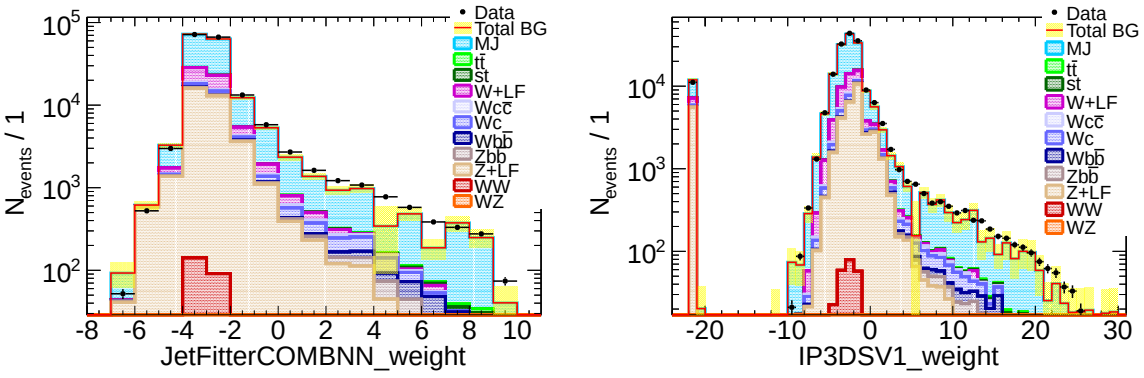

Figure 4.18.: The absolute value of the relative difference between the data and the background expectation in the multijet control region ($\not\!\!E_{\mathrm{T}} \leq 25$ GeV, $M_T \leq 40$ GeV) for the distribution of the JetCOMBNN (left) and IP3DSV1 (right) b-tag weight in the muon channel. The black line is the fit of a polynomial (degree 1).

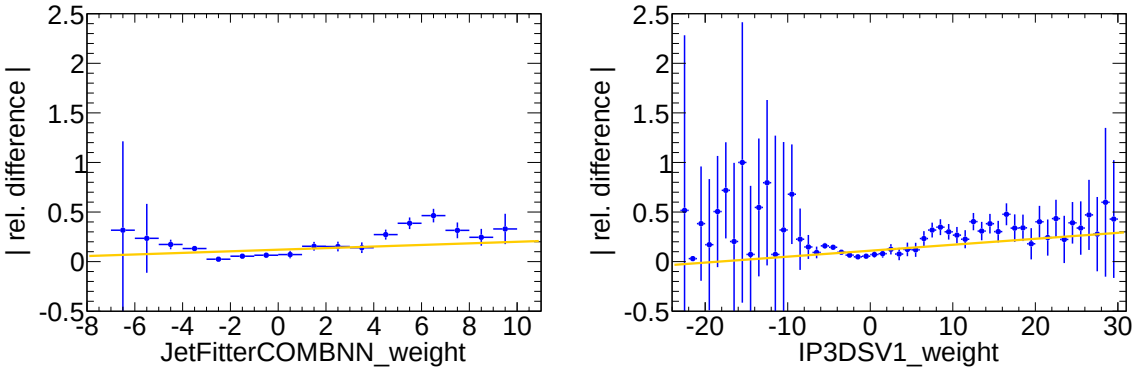

Figure 4.19.: The absolute values of the relative difference between the data and the background expectation in the multijet control region ($\not\!\!E_{\mathrm{T}} \leq 25$ GeV, $M_T \leq 40$ GeV) for the distribution of the JetCOMBNN (left) and IP3DSV1 (right) b-tag weight in the electron channel. The black line is the fit of a polynomial (degree 1).

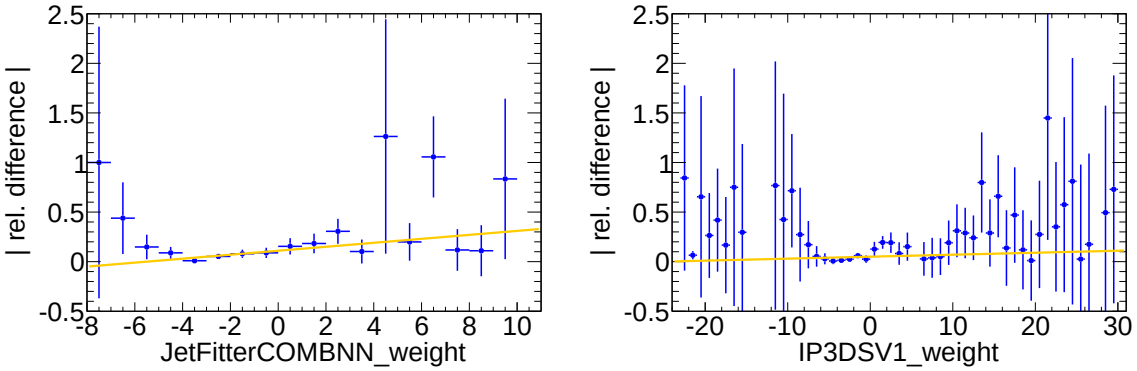

Table 4.2.: Result of the fit of a polynomial (degree 1) to the absolute values of the relative difference between the data and the background prediction in the JetCOMBNN and IP3DSV1 b-tag weight distributions.

channel	lin. function (JetCOMBNN)	lin. function (IP3DSV1)
muon	$0.12 + 0.008\ x$	$0.11 + 0.006\ x$
electron	$0.11 + 0.02\ x$	$0.05 + 0.002\ x$

4.4. Results of the Multijet Background Estimate

In Figure 4.21a (4.22a), the $m_{b\bar{b}}$ distribution for the multijet background in the SR before the p_T^W splitting for the muon (electron) channel is illustrated, whereas Figure 4.20 (4.21) depicts the p_T^W-split distributions. The blue distributions are the original distributions derived from the multijet estimate after the b-tag requirements. Unfortunately, the statistical precision gets very poor for $p_T^W \geq 50$ GeV. Therefore, the $m_{b\bar{b}}$ shapes of the multijet estimate without b-tag cuts are taken and normalized to the b-tagged $m_{b\bar{b}}$ distributions. For all p_T^W bins, the normalization factor from the untagged to the tagged distributions is taken from the $m_{b\bar{b}}$ distributions before the p_T^W splitting. The number of multijet events in the different p_T^W bins is listed in Table 4.3. For the first p_T^W bin, the contribution from the electron and muon channel is comparably large. However, the muon channel multijet contribution decreases significantly faster with rising p_T^W than the electron channel resulting in 76.2 ± 22.9 events (muon channel) and 134.6 ± 61.8 events (electron channel) summed up over the four p_T^W bins.

Table 4.3.: Result of the multijet estimate in the signal region after all cuts split into the different p_T^W bins ($p_T^W < 50$ GeV, 50 GeV $\leq p_T^W < 100$ GeV, 100 GeV $\leq p_T^W < 200$ GeV, 200 GeV $\leq p_T^W$) for both the muon and electron channel. The given uncertainty is the estimated systematic uncertainty on the prediction of the multijet background.

channel	1st p_T^W bin	2nd p_T^W bin	3rd p_T^W bin	4th p_T^W bin	total
muon	70.1 ± 16.8	5.9 ± 5.9	0.2 ± 0.2	0.0	76.2 ± 22.9
electron	74.1 ± 28.9	42.4 ± 14.8	15.0 ± 15.0	3.1 ± 3.1	134.6 ± 61.8

Figure 4.20.: The data-driven multijet (MJ) estimate for the invariant mass $m_{b\bar{b}}$ of the two b-tagged jets for the signal region in the muon channel. The events are shown before (a) and after (b-e) splitting into four different p_T^W bins. The green distribution is the MJ estimate before b-tagging, but normalized to the MJ estimate after b-tagging. The blue distribution is the MJ estimate after b-tagging.

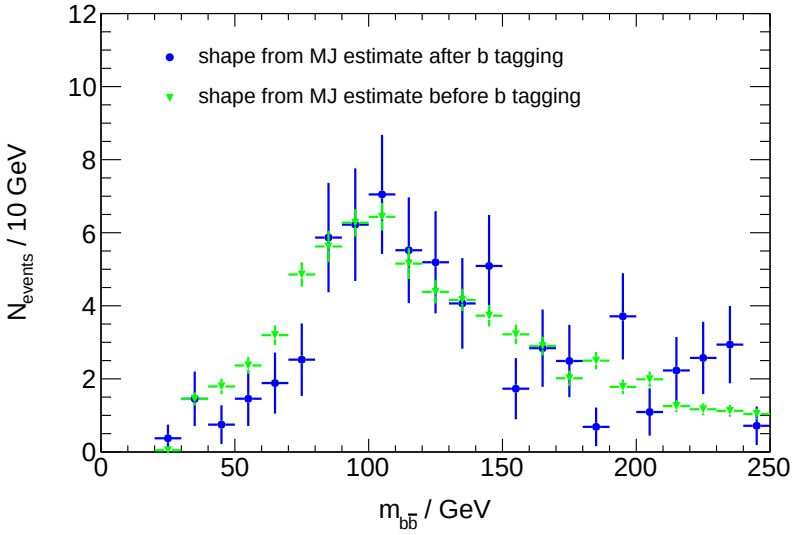

(a) no p_T^W splitting

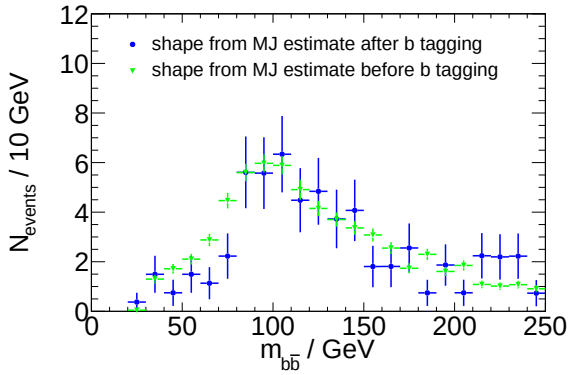

(b) $p_T^W < 50$ GeV

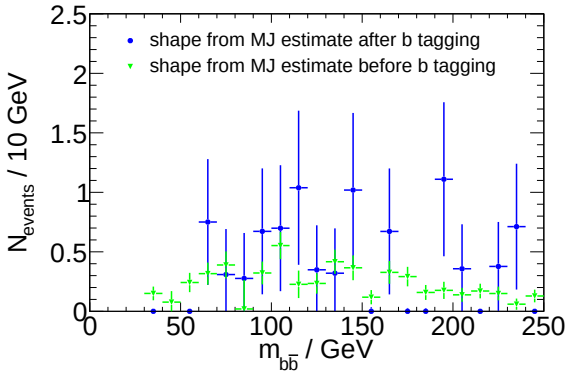

(c) 50 GeV $\leq p_T^W < 100$ GeV

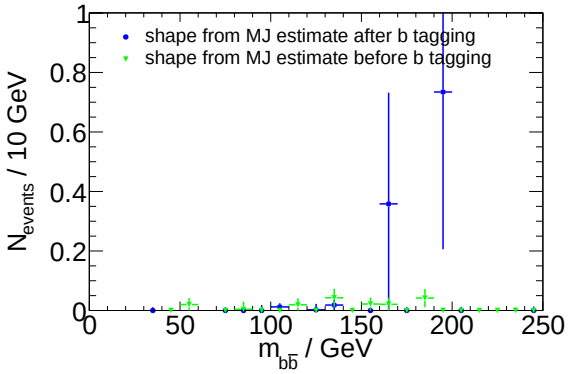

(d) 100 GeV $\leq p_T^W < 200$ GeV

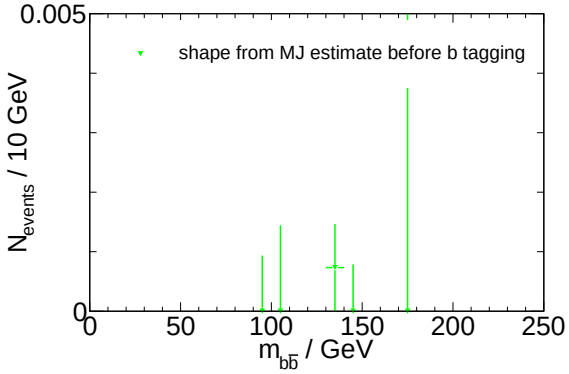

(e) 200 GeV $\leq p_T^W$

Figure 4.21.: The data-driven multijet (MJ) estimate for the invariant mass $m_{b\bar{b}}$ of the two b-tagged jets for the signal region in the electron channel. The events are shown before (a) and after (b-e) splitting into four different p_T^W bins. The green distribution is the MJ estimate before b-tagging, but normalized to the MJ estimate after b-tagging. The blue distribution is the MJ estimate after b-tagging.

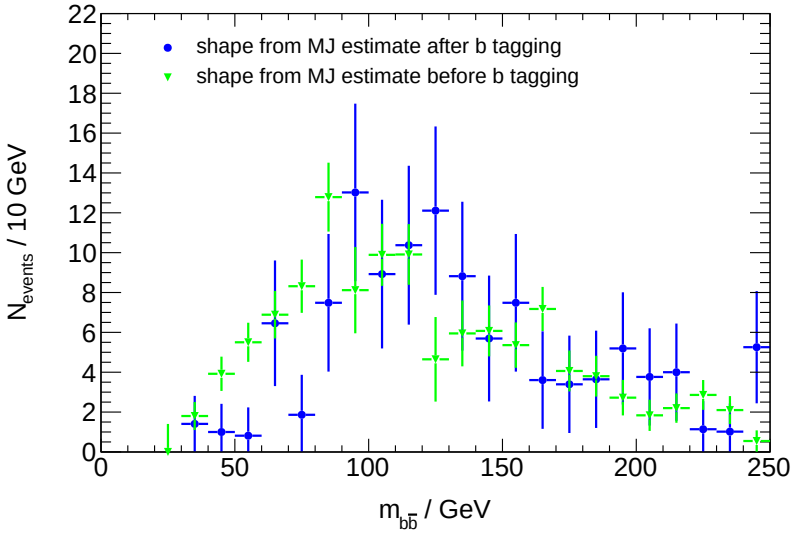

(a) no p_T^W splitting

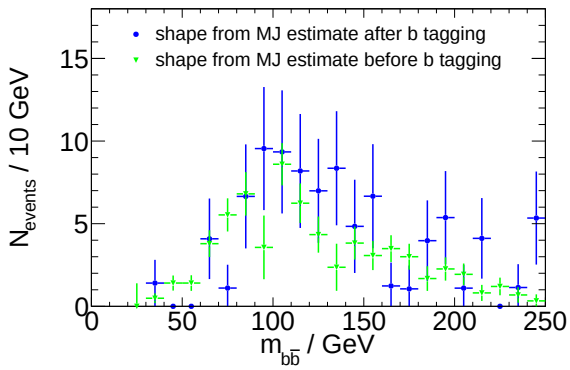

(b) $p_T^W < 50$ GeV

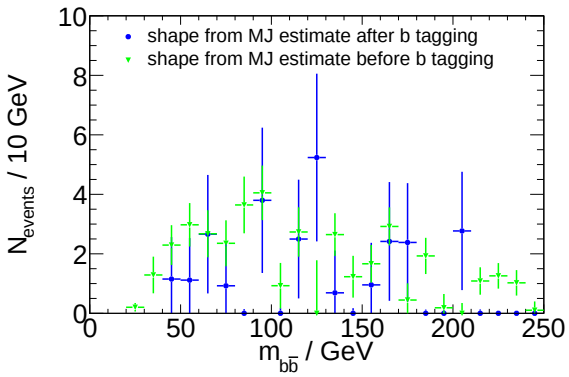

(c) 50 GeV $\leq p_T^W < 100$ GeV

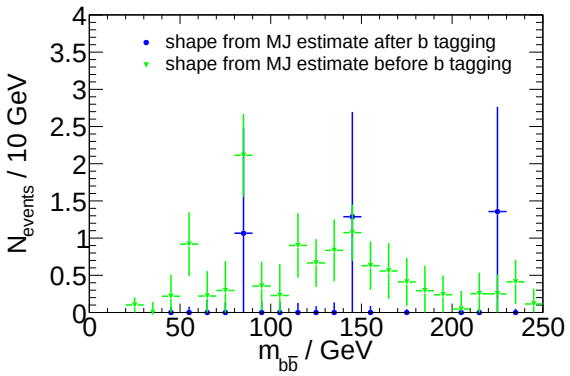

(d) 100 GeV $\leq p_T^W < 200$ GeV

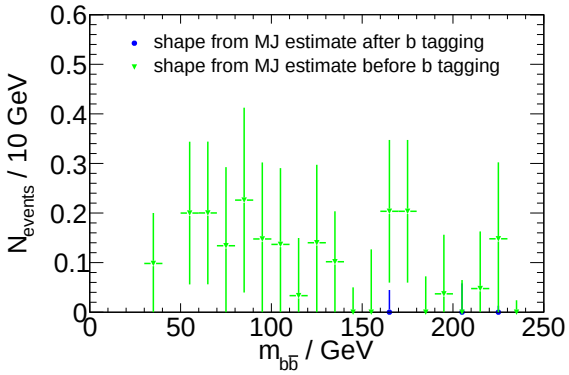

(e) 200 GeV $\leq p_T^W$

5. Normalization of the W+jets and Top Background

The description of the shape of the different W+jets components relies on MC simulation. The relative contributions from these components to W+jets, however, are obtained by fits to the data. They consists of $W + b\bar{b}$, the production of a W boson in association with a pair of b quarks, $W + c$ ($W + c\bar{c}$), events with one W boson and one c quark (a pair of c quarks), and $W + LF$, the associated production of a W boson together with light quarks or gluons. After the fit of these components to a dedicated distribution, the total W+jets background is fitted to data together with the top background, that consists of $t\bar{t}$ and single top production.

5.1. The W+jets Background Composition

Since the next-to-leading order corrections for the $W+b\bar{b}$ production can have a significant influence on the production cross section and still suffer from large uncertainties [52], the relative contributions from $W+b\bar{b}$, $W+c\bar{c}$, $W+c$, and $W+LF$ to the W+jets background are fitted in a distribution sensitive to heavy flavour jets. The b-tag weight distribution fulfils this criterion and is chosen for the WH analysis.
The b-tag weights of the JetFitterCOMBNN and the IP3DSV1 b-tagging algorithms are selected for the fit. The fits to both distributions deliver independent results that can be cross checked and combined. All analysis cuts except for the b-tag cuts are applied before the fit. To avoid any possible contribution from the WH signal in the fit, only the lower m_{jj} sideband region satisfying $m_{jj} < 80$ GeV is used(see Figure 3.10). The fit is performed to the sum of the b-tag weights of both selected jets. It is a combined fit for the electron and muon channel: The distributions consist of the sum of the corresponding distributions in the electron and muon channel.

Figure 5.1 compares the shapes of the b-tag weights for the different W+jets components for the JetFitterCOMBNN, IP3DSV1, and MV1 tagging algorithms, respectively. Since for these b-tagging algorithms, the probability of being a b jet increases with increasing value of the b-tag weight, the $W + b\bar{b}$ component is dominant for large weight values. The $W + c\bar{c}$ and $W + c$ components are the second most important at large b-tag weights, since c jets are more easily misidentified as b jets than light / gluon jets due to their larger lifetime. Because the shapes of the $W + c\bar{c}$ and $W + c$ components are very similar, only a combined template $W + c(\bar{c})$ is used for the fit. It consists of the sum of $W + c\bar{c}$ and $W + c$, both weighted according to their cross sections.

As for the multijet estimate, the TFractionFitter method of ROOT is used for a template fit [23]. Three templates are used: one for each of the three flavour components containing b, c, or (only) light flavour quarks / gluons. These templates are fitted to the data distribution of the b-tag weights after subtracting the non-W+jets backgrounds, i.e. top, multijet, Z+jets, WW, and WZ. The fit is performed over the full range of the distributions not to (dis-)favour any of the components. It results in scaling factors SF_b, SF_c, and SF_{LF} for the three different templates. These scaling factors do not only correct the (conservative) K-factor of 1.2, that is considered already in the cross sections of the different MC samples (see Table 3.3). Since the scaling factors are extracted at reconstruction level, they account furthermore for variations of the b-tagging efficiency and mistag rate, that differs from sample to sample. Therefore, they are not universal but only applicable for the outlined setting.

The fit to the b-tag weight is done separately for the two selected taggers JetFitterCOMBNN and IP3DSV1 and the arithmetic mean of the scaling factors is taken for the succeeding steps of the analysis. In case of the MV1 tagger, the shapes of the three templates are not different enough to gain sensible scaling factors for all three templates.

Since the multijet background estimate has a significant systematic uncertainty (see Section 4.3 and Table 4.2), the fits are additionally done after scaling the multijet background up and down to account for this uncertainty. The result of the fit is presented in Figure 5.4 and Table 5.1. For both b taggers, the sum of the scaled templates agrees reasonably within the statistical uncertainties with the data distribution. The $W + LF$ component is scaled down in both the JetFitterCOMBNN and IP3DSV1 fit by a factor of $SF_{LF} = 0.85 \pm 0.01$ ($SF_{LF} = 0.83 \pm 0.01$), whereas the $W + c(\bar{c})$ component is scaled up significantly by a factor $SF_c = 1.22 \pm 0.04$ ($SF_c = 1.32 \pm 0.04$). For the $W + b\bar{b}$ component, both taggers have an opposite scaling trend: the JetFitterCOMBNN fit scales it up by $SF_b = 1.18 \pm 0.06$, whereas IP3DSV1 keeps the $W + b\bar{b}$ component constant by a scaling factor $SF_b = 0.99 \pm 0.07$. The systematic uncertainty on the scaling factors due to the

multijet background description (sys(MJ)) is negligible for SF_{LF}, SF_c and SF_b compared to the statistical uncertainty of the fit.

Table 5.1.: The scaling factors SF_b, SF_c, and SF_{LF} as result of the fit of the JetFitterCOMBNN and IP3DSV1 b-tag weight distributions. The statistical uncertainty on the fit as well as the systematic uncertainty on the multijet background estimate (sys(MJ)) are considered. The corresponding sign of the systematic uncertainty of the scaling factors due to the systematic variations of the multijet background is defined as follows: If the scaling factor increases when sys(MJ) is varied up, this is symbolized by "$\pm$", in the opposite case by "$\mp$".

$SF_b \pm$ stat $\pm$ sys(MJ)	$SF_c \pm$ stat $\pm$ sys(MJ)	$SF_{LF} \pm$ stat $\pm$ sys(MJ)
JetFitterCOMBNN		
$1.18 \pm 0.06 \mp 0.00003$	$1.22 \pm 0.04 \mp 0.00004$	$0.85 \pm 0.01 \mp 0.00002$
IP3DSV1		
$0.99 \pm 0.07 \mp 0.00003$	$1.32 \pm 0.04 \mp 0.00005$	$0.83 \pm 0.01 \mp 0.00003$
arithmetic mean		
$1.09 \pm 0.07 \mp 0.00003$	$1.27 \pm 0.04 \mp 0.00005$	$0.84 \pm 0.01 \mp 0.00003$

5.2. The Sideband Fit in the Invariant Mass Distribution

After the fit of the different components forming the W+jets background, the composite W+jets background is fitted together with the top ($t\bar{t}$ and single top) background in the sideband region of the $m_{b\bar{b}}$ distribution after applying all analysis cuts. The side band region comprises the lower side band 0 GeV $\leq m_{b\bar{b}} <$ 80GeV and the upper side band 150 GeV $< m_{b\bar{b}} <$ 250 GeV. The fitting region is motivated by the dominance of the W+jets background in the low $m_{b\bar{b}}$-region, whereas the high $m_{b\bar{b}}$-range is dominated by top (see Figure 3.10 in Section 3.1). The ROOT TFractionFitter method is again used for the sideband fit [23].

Before the fit, all background components that do not participate in the fit are subtracted from the data distribution. The result of the fit is depicted in Figure 5.3. In the sideband region, the sum of both templates agrees within the statistical uncertainties with the subtracted data distribution. The scaling factor for the W+jets template $SF_{W+\text{jets}}$ is 0.92 ± 0.29 (stat) and the factor for the top templates SF_{top} amounts to 1.13 ± 0.15 (stat). The scaling of the top background by $SF_{\text{top}} = 1.13$ is validated in a top enriched control region. Since top events contain on average more than two jets, the top control region is defined by the default WH cuts except for the number of jets: instead of exactly two

Figure 5.1.: The normalized distributions of the JetFitterCOMBNN, IP3DSV1, and the MV1 b-tag weight for the different components of the W+jets background, $W + b\bar{b}$, $W + c\bar{c}$, $W + c$, and $W + LF$, before the b-tagging step, for events in the lower m_{jj} sideband region ($m_{jj} < 80$ GeV). The distributions show the sum of the b-tag weight of leading and next-to-leading jet. The combination of electron and muon channel is depicted.

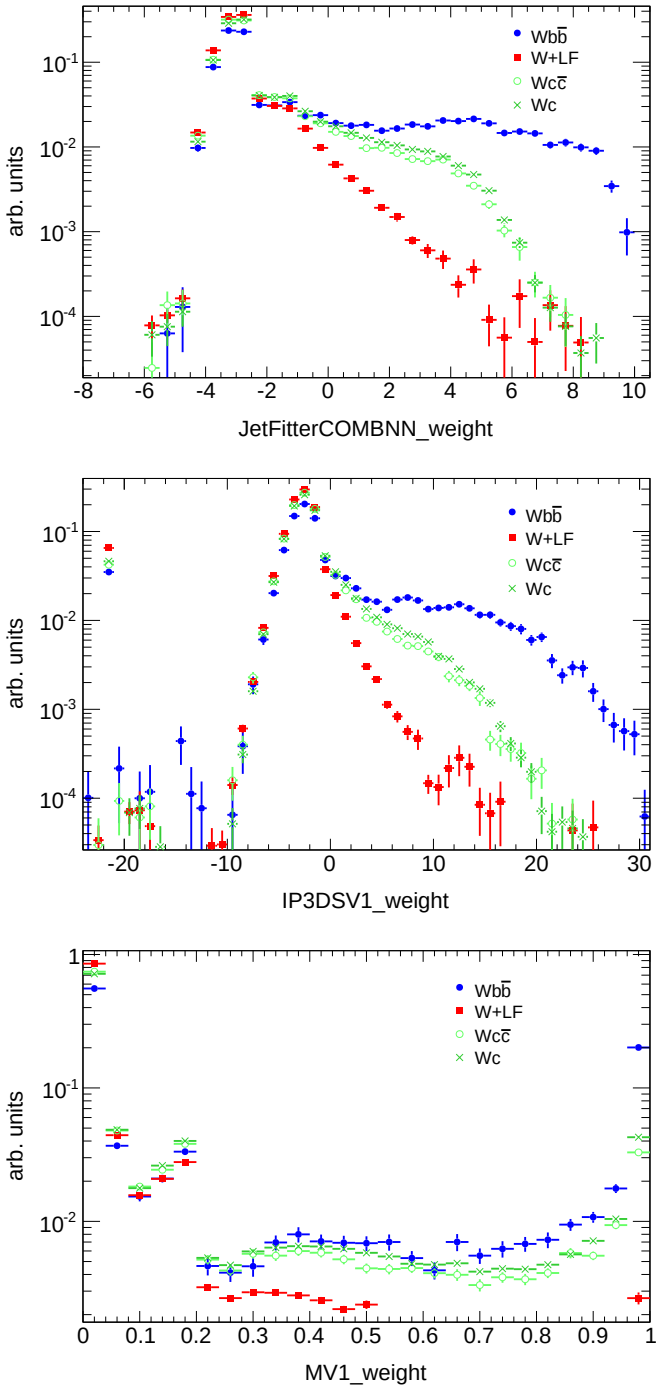

Figure 5.2.: The data distribution after background subtraction for the b-tag weights JetFitterCOMBNN and IP3DSV1, the fitted $W + b\bar{b}$, $W + c(\bar{c})$, and $W + LF$ templates, and the sum of all fitted templates.

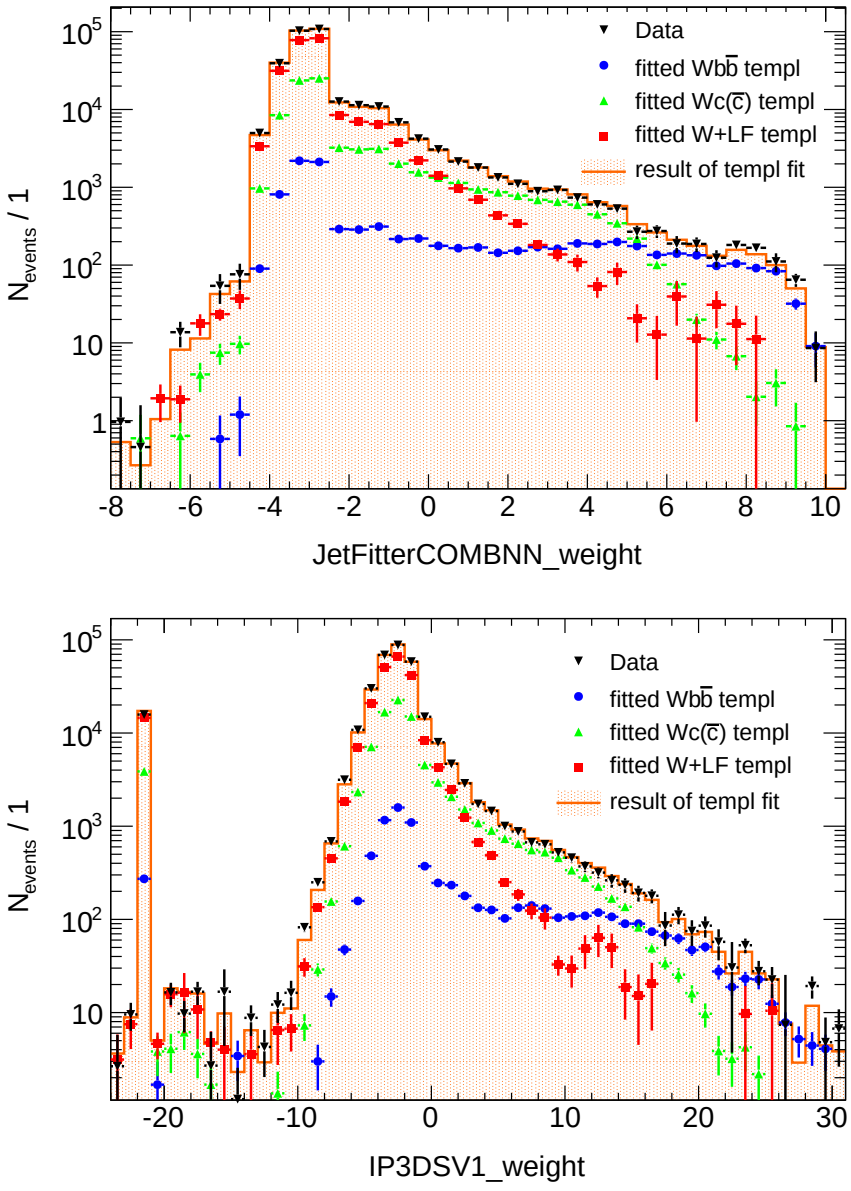

jets that are both b-tagged, exactly three jets are required. The leading and the next-to-leading jet have to be b-tagged and are used to form the invariant mass $m_{b\bar{b}}$.
A data-driven multijet estimate is used for the top control region, which follows the approach as outlined in Section 4.1 but is adapted for the needs of the top control region by requiring three jets.
Figure 5.4 depicts the $m_{b\bar{b}}$ distribution in the top control region for both the electron and muon channel. The top and W+jets background samples are scaled by the scaling factors derived in the sidebands of the signal $m_{b\bar{b}}$ distribution. Both the electron and muon channel show a decent agreement between the data distribution and the background prediction.

5.3. Consistency with the Fit of the $\not{E}_{\mathrm{T}}$ Distribution

In Section 4, scaling factors for the multijet modelling region MMR and the non-multijet background non-MJ where derived by a template fit of the $\not{E}_{\mathrm{T}}$ distribution. These scaling factors SF_{MMR} and $SF_{\text{non-MJ}}$ where calculated before any knowledge about the scaling factors for the W+jets components SF_b, SF_c, and SF_{LF} and the scaling factors SF_{top} and $SF_{W+\text{jets}}$ for the top and the combined W+jets background.
To check whether the results of SF_{MMR} and $SF_{\text{non-MJ}}$ are consistent with the consecutively derived scaling factors, the factors SF_{MMR} and $SF_{\text{non-MJ}}$ are re-evaluated after applying

Figure 5.3.: The data distribution for the invariant mass $m_{b\bar{b}}$ after subtracting all non-top and non-W+jets background for 0 GeV $\leq m_{b\bar{b}} \leq$ 250 GeV. The scaled W+jets and top template and the sum of both templates are shown in the side band region for 0 GeV $\leq m_{b\bar{b}} <$ 80GeV and 150 GeV $< m_{b\bar{b}} <$ 250 GeV.

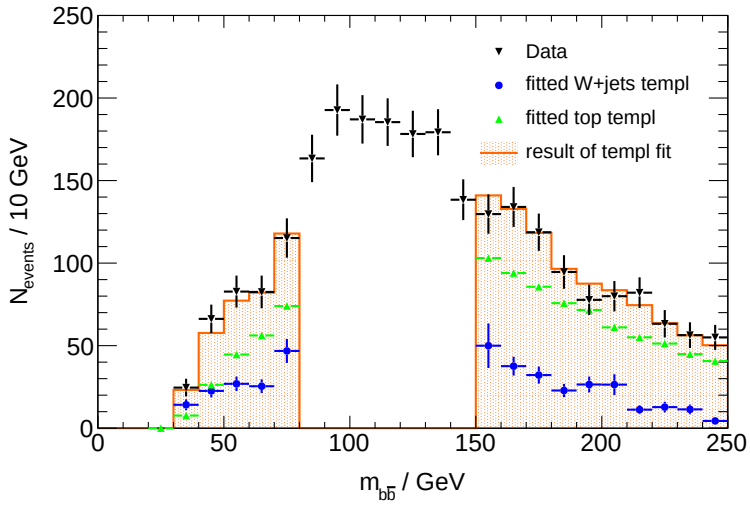

Figure 5.4.: The distribution of the invariant mass $m_{b\bar{b}}$ in the top control region having exactly three jets and at least two b-tagged jets. The figure illustrates the data distributions together with the background predictions consisting of the data-driven multijet estimate and the MC expectations for the non-multijet backgrounds. The top and W+jets backgrounds are scaled by scaling factors derived in the sidebands of the signal $m_{b\bar{b}}$ distribution.

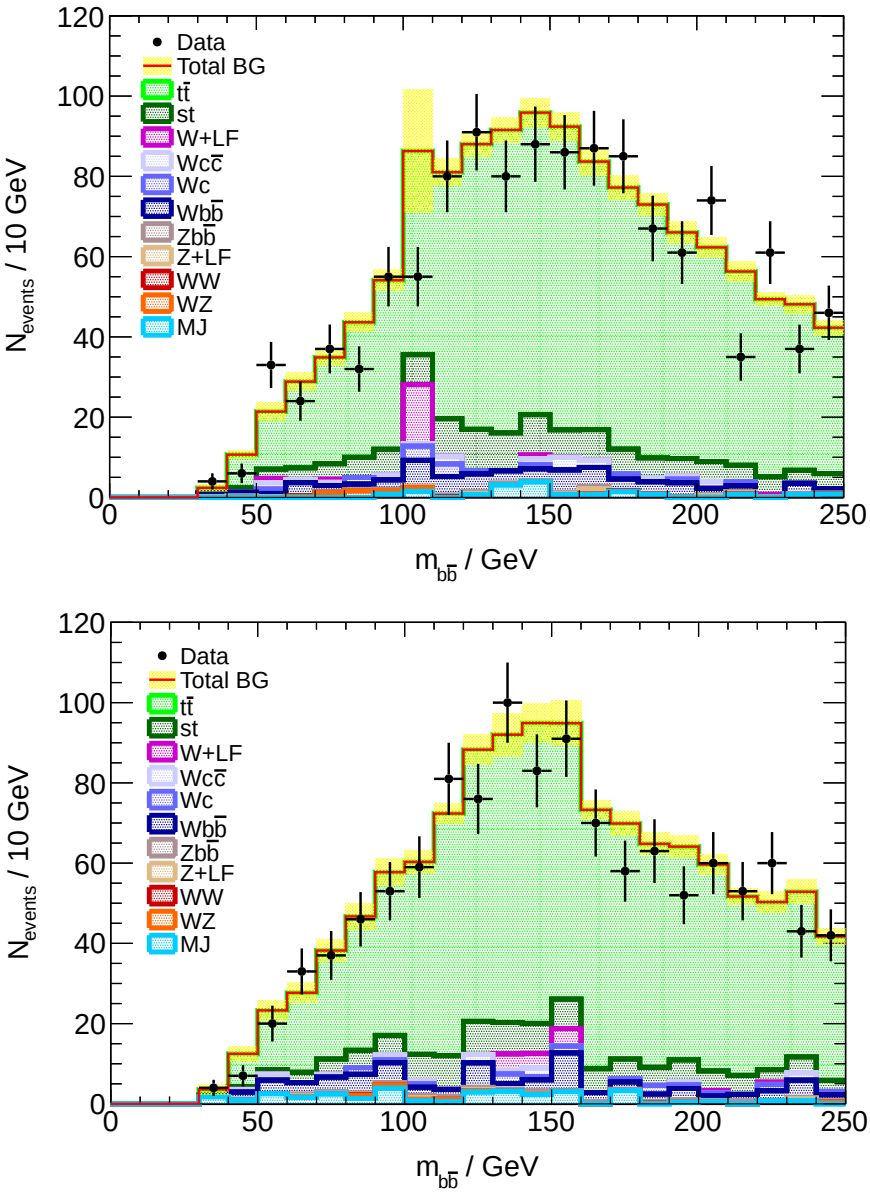

SF_b, SF_c, and SF_{LF} as well as SF_{top} and $SF_{W+\text{jets}}$.
In Table 5.2 the results for SF_{MMR} and $SF_{\text{non-MJ}}$ are listed for the muon and electron channel before and after scaling the top and W+jets background. The values of SF_{MMR} agree within the statistical uncertainties of the $\not\!\!E_{\text{T}}$ template fit for both the muon and electron channel, even after varying SF_{top} and $SF_{W+\text{jets}}$ up or down by the significant statistical uncertainties of the $m_{b\bar{b}}$ sideband fit (see Section 5.2). For the final results of the WH analysis, the original SF_{MMR} value before the top and W+jets scaling is taken. Also the values for $SF_{\text{non-MJ}}$ agree within the statistical uncertainties of the $\not\!\!E_{\text{T}}$ fit before and after scaling the top and W+jets background. In contrast to SF_{MMR}, the values for $SF_{\text{non-MJ}}$ do not agree within the statistical uncertainties of the $\not\!\!E_{\text{T}}$ fit after varying SF_{top} and $SF_{W+\text{jets}}$ up or down. But the up- and downward variations of SF_{top} and $SF_{W+\text{jets}}$ form an uncertainty band around $SF_{\text{non-MJ}} = 1$, that contains the original value of $SF_{\text{non-MJ}}$. Since the non-MJ template of the $\not\!\!E_{\text{T}}$ fit consists mainly of top and W+jets background, the influence of the up and downward variations of SF_{top} and $SF_{W+\text{jets}}$ have a larger impact on $SF_{\text{non-MJ}}$ than on SF_{MMR}: By scaling SF_{top} and $SF_{W+\text{jets}}$ up ($SF_{\text{top}} = 1.28$ and $SF_{W+\text{jets}} = 1.21$), $SF_{\text{non-MJ}}$ is lower than the original value due to the increased contributions from top and W+jets. The downward variation of SF_{top} and $SF_{W+\text{jets}}$ ($SF_{\text{top}} = 0.98$ and $SF_{W+\text{jets}} = 0.63$) has to be compensated by a larger value of $SF_{\text{non-MJ}}$. But it has to be remembered, that the $\not\!\!E_{\text{T}}$ fit is performed before the cuts on $\not\!\!E_{\text{T}}$ and M_T, whereas the $m_{b\bar{b}}$-sideband fit, that results in SF_{top} and $SF_{W+\text{jets}}$, is done after the $\not\!\!E_{\text{T}}$ and M_T cuts. Therefore, a direct comparison between the variations of SF_{top} and $SF_{W+\text{jets}}$ and their impact on $SF_{\text{non-MJ}}$ is not possible.

Table 5.2.: The scaling factors SF_{MMR} and $SF_{\text{non-MJ}}$ before and after taking into account the scaling factors for W+jets and top for the muon and electron channel. Furthermore, SF_{MMR} and $SF_{\text{non-MJ}}$ are recalculated after varying SF_{top} and $SF_{W+\text{jets}}$ up and down by the statistical uncertainties of the $m_{b\bar{b}}$ sideband fit. These variations are denoted by "(stat up)" and "(stat down)", respectively. The uncertainties of SF_{MMR} and $SF_{\text{non-MJ}}$ express only the statistical uncertainties on the $\not\!\!E_{\text{T}}$ template fit.

	SF_{MMR} (muon)	$SF_{\text{non-MJ}}$ (muon)
bef. top and W+jets scaling	0.37 ± 0.03	1.10 ± 0.05
scale top and W+jets	0.38 ± 0.03	1.02 ± 0.05
scale top and W+jets (stat up)	0.38 ± 0.03	0.85 ± 0.04
scale top and W+jets (stat down)	0.39 ± 0.03	1.28 ± 0.06

	SF_{MMR} (elec)	$SF_{\text{non-MJ}}$ (elec)
bef. top and W+jets scaling	1.41 ± 0.08	0.94 ± 0.05
scale top and W+jets	1.41 ± 0.08	0.88 ± 0.05
scale top and W+jets (stat up)	1.41 ± 0.08	0.73 ± 0.04
scale top and W+jets (stat down)	1.42 ± 0.09	1.09 ± 0.06

6. Results in the Channel WH $\rightarrow l\nu b\bar{b}$

After the detailed discussion of the background estimate in the previous chapter, this chapter is devoted to the comparison between the background prediction and the data distributions in the signal region, as well as the expectations for the signal process.

6.1. Data-MC Comparison

To consolidate the confidence in the kinematic description of the signature comprising one lepton, two b jets and $\not{E}_{\mathrm{T}}$, the data and background predictions of variables describing those physics objects are compared. As electron and muon channel have different systematic uncertainties, the channels are treated separately in this section. For the $m_{b\bar{b}}$ distributions presented in this part, the shape of the multijet background is described by the distribution before b tagging. For all other distributions, the shape of the distribution after b tagging is kept (see Section 4.3).
At first, the data and background are compared for the $\not{E}_{\mathrm{T}}$ and M_T distribution, shown in Figure 6.1 and 6.2 for the muon and electron channel, respectively. For the $\not{E}_{\mathrm{T}}$ distribution, all analysis cuts except the cut on $\not{E}_{\mathrm{T}}$ and M_T are applied. The same holds for the M_T distribution with the exception that the $\not{E}_{\mathrm{T}}$ cut is already applied. Both the muon and the electron channel show a reasonable agreement between the data and the background prediction for the $\not{E}_{\mathrm{T}}$ distribution. For the M_T distribution, this holds for the range $M_T > 30$ GeV. In the multijet dominated region $M_T \leq 30$ GeV the background is overestimated especially in the electron channel. This discrepancy lies within the systematic uncertainties on the multijet estimate (see Section 4.2) and the top and W+jets scaling factors (see Section 5.2). The yellow band accounts only for the limited statistics of the background samples.
Figure 6.3 (6.4) depicts kinematic distributions of the signal lepton after all selection cuts for the muon (electron) channel. The η, ϕ and p_T distributions for muons and electrons

demonstrate a decent agreement between the data and the background predictions. Some bins suffer from the insufficient statistics in the $W + LF$ samples. The significantly reduced number of muons in the η range around 0 is caused by the service shaft in the muon spectrometer (see Section 2.3).
The basic kinematic distributions of the selected jets are presented in the Figures 6.5 and 6.6 for the muon and electron channel, respectively. All distributions for η, ϕ and p_T for the leading and next-to-leading jet, as well as the distance $\Delta R_{b\bar{b}}$ feature a satisfying agreement for both lepton channels.
The p_T^W distributions are presented in Figure 6.7 and 6.8 for the muon and electron channel, respectively. They show as well a good agreement between data and background prediction.
The top background dominates the central η region as well as the medium and high p_T region. This holds for both lepton flavours as well as for the leading and next-to-leading jet.

Figure 6.1.: The $\not\!\!E_{\mathrm{T}}$ distribution (left plot) after all selection cuts except the cut on $\not\!\!E_{\mathrm{T}}$ and M_T. The M_T distribution (right plot) after all selection cuts except the M_T cut. The distributions refer to the muon channel.

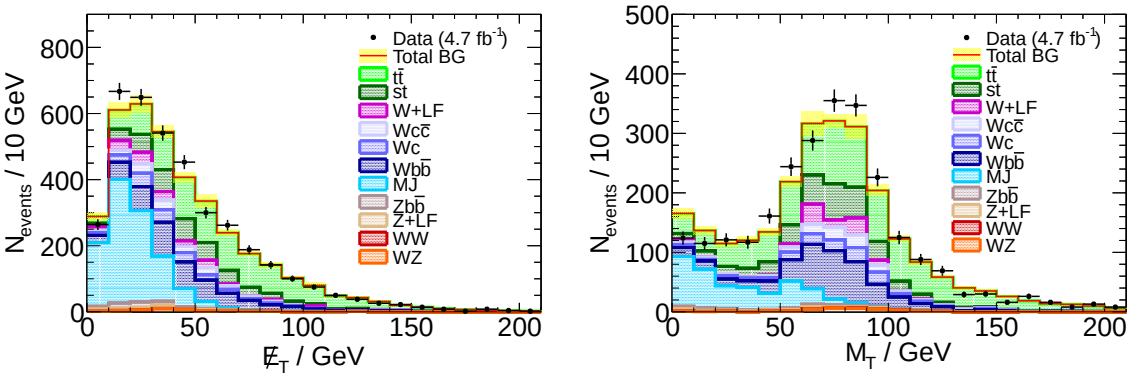

Figure 6.2.: The $\not\!\!E_{\mathrm{T}}$ distribution (left plot) after all selection cuts except the cut on $\not\!\!E_{\mathrm{T}}$ and M_T. The M_T distribution (right plot) after all selection cuts except the M_T cut. The distributions refer to the electron channel.

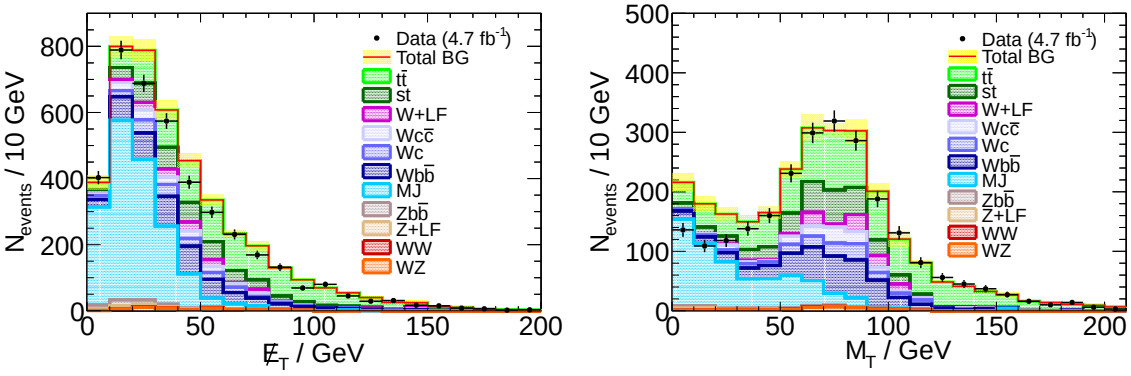

Figure 6.3.: The distributions for η, ϕ, and p_T for the signal muon after all selection cuts.

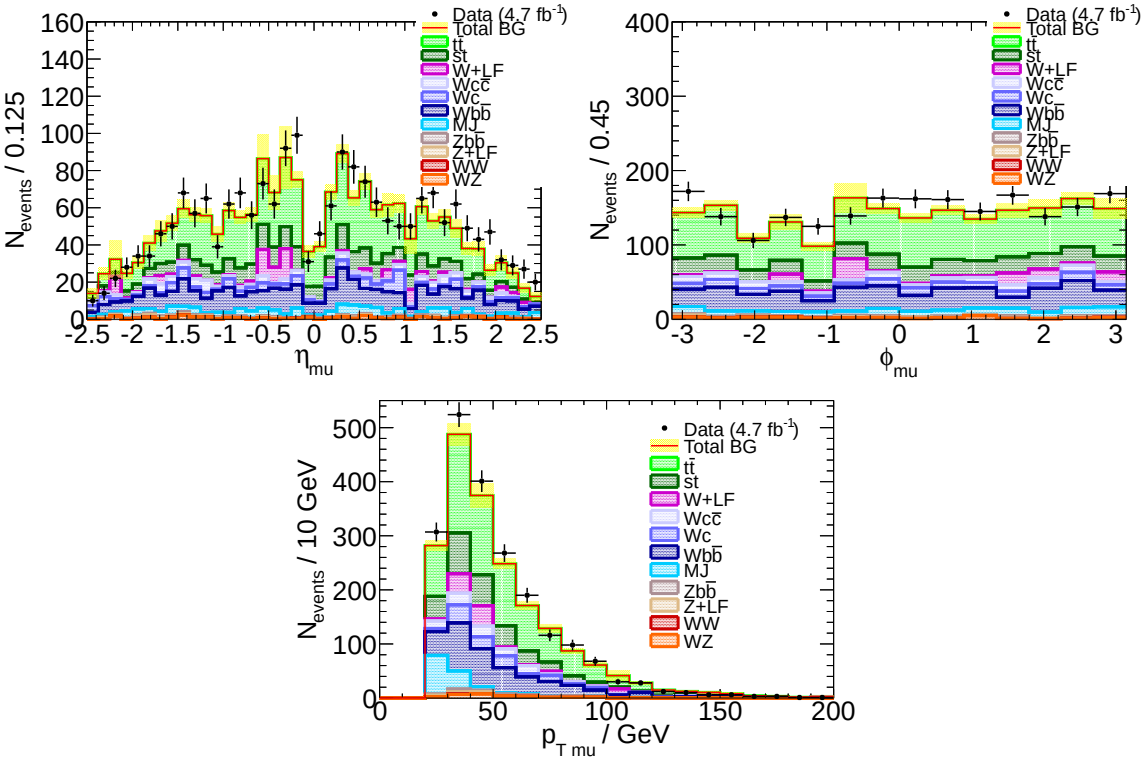

Figure 6.4.: The distributions for η, ϕ, and p_T for the signal electron after all selection cuts.

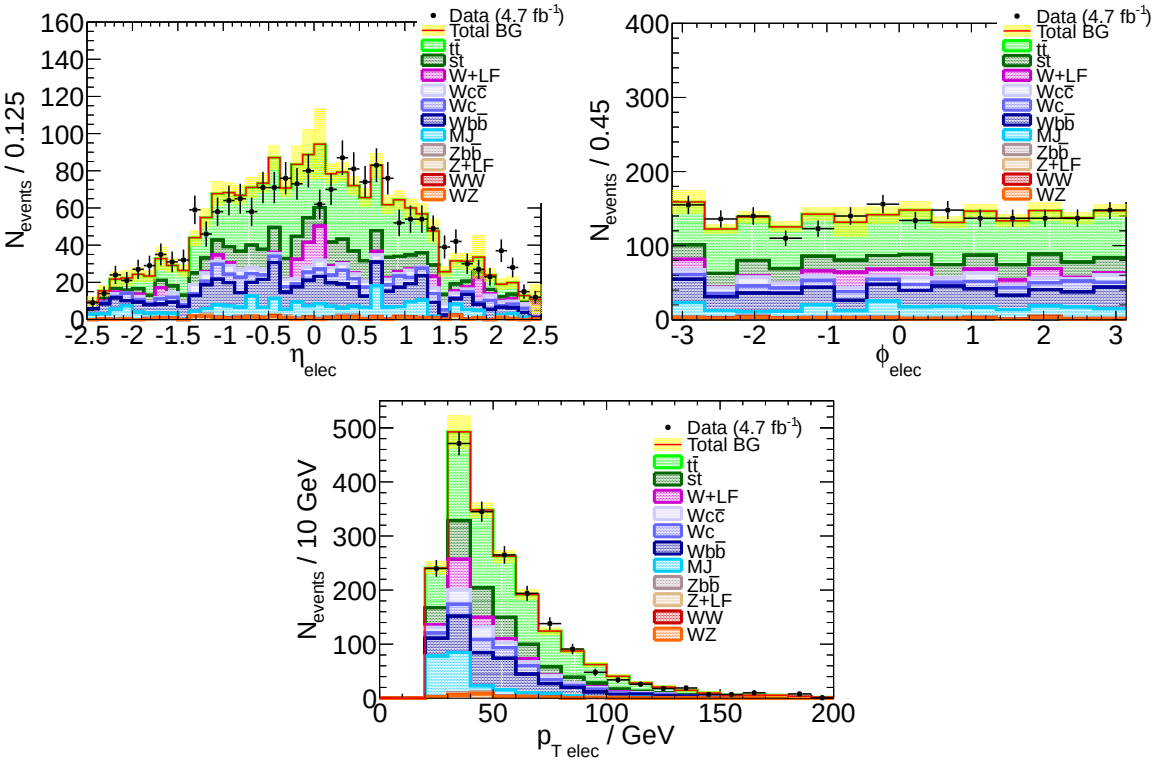

Figure 6.5.: The η, ϕ, p_T, and ΔR distribution(s) of the leading and next-to-leading jet in the muon channel after all selection cuts.

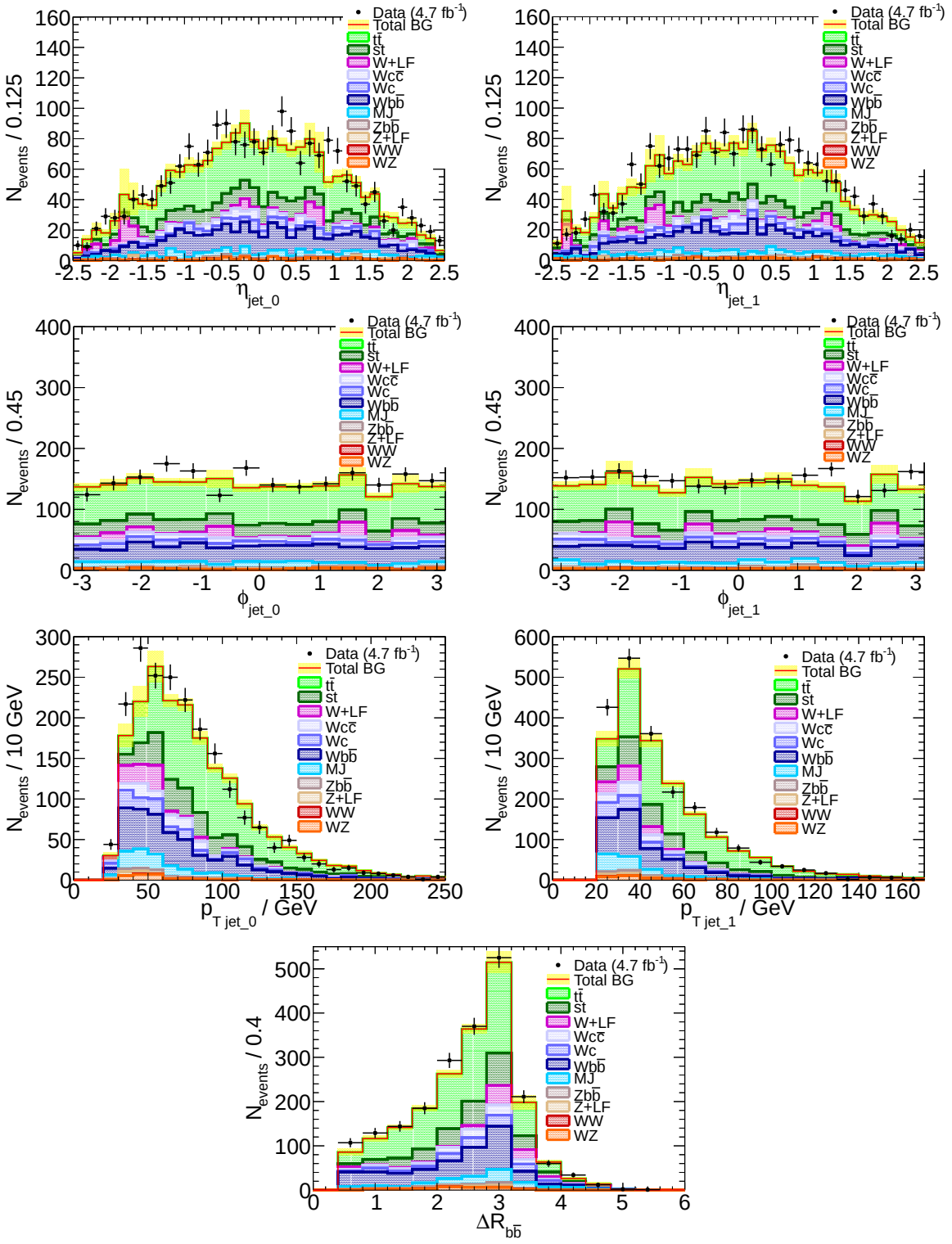

Figure 6.6.: The η, ϕ, p_T, and ΔR distribution(s) of the leading and next-to-leading jet in the electron channel after all selection cuts.

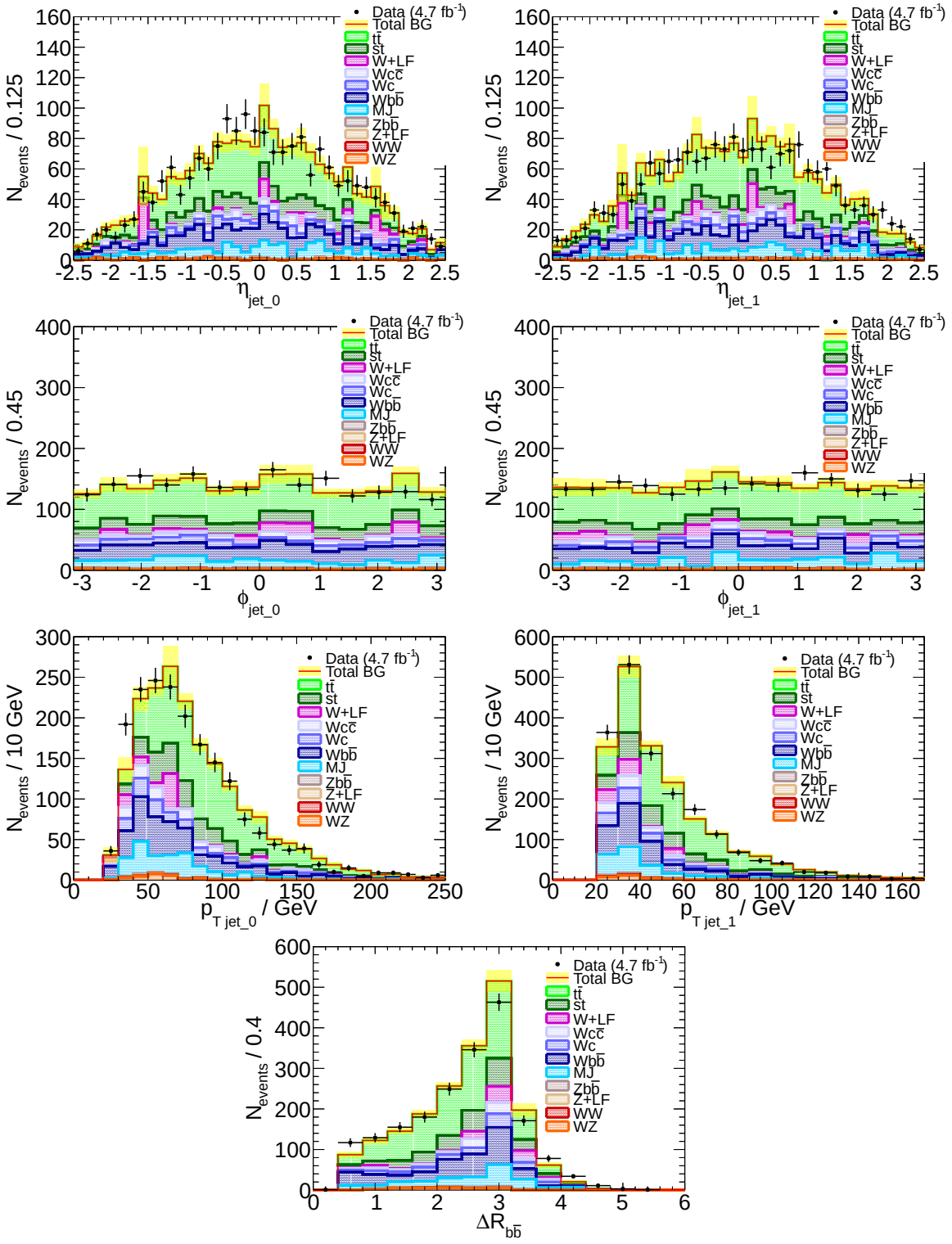

Figure 6.7.: The p_T^W distribution in the muon channel after all selection cuts.

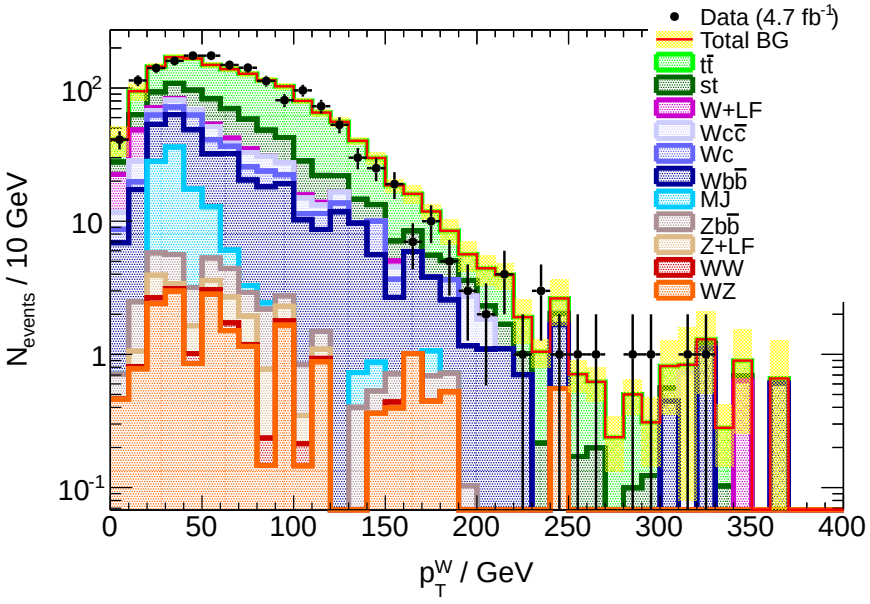

Figure 6.8.: The p_T^W distribution in the electron channel after all selection cuts.

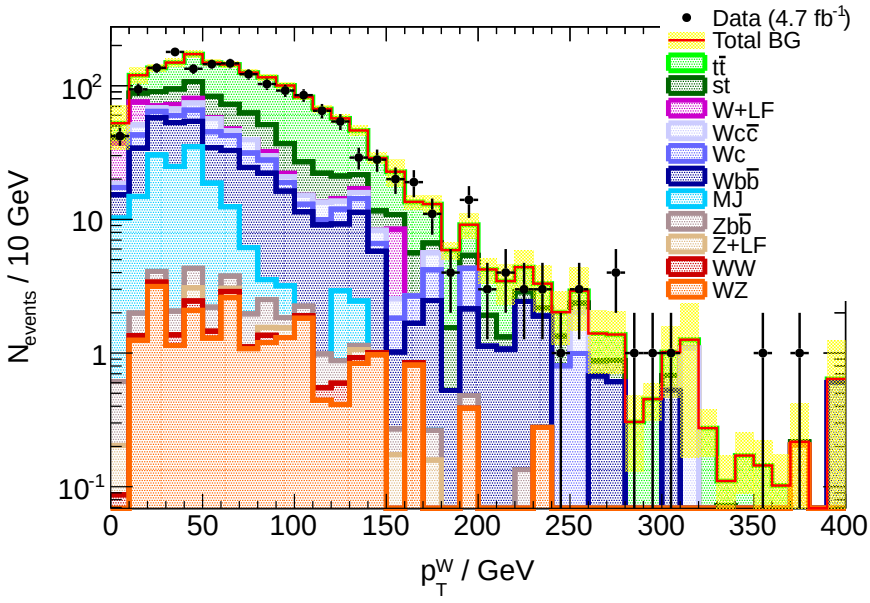

6.2. The Invariant Mass Distribution of the two b Jets

The most important distribution for the WH analysis is the invariant mass $m_{b\bar{b}}$ of the b jet pair, that is finally split into four p_T^W bins.
Figure 6.9 (6.11) presents the $m_{b\bar{b}}$ distribution before the p_T^W splitting for the muon (electron) channel. The corresponding distributions after the splitting are shown in Figure 6.10 (6.12). Besides the data distribution and the background prediction, the plots contain the distribution for a 125 GeV WH Higgs signal drawn in magenta. The signal is scaled by a factor five for visibility reasons.
The Tables 6.1 and 6.2 summarize the event yield for the data and background prediction as well as the signal expectation for the muon and electron channel, respectively. The presented numbers only refer to the signal region $80 \leq m_{b\bar{b}} \leq 150$ GeV. The given uncertainties for the signal and background yield refer to the statistical uncertainties caused by the limited statistics of the corresponding samples. Both the electron and muon channel show a good agreement between the data and the background expectation.
Among the different background contributions before the p_T^W splitting, the most important one is provided by top, which amounts to $\approx 57\%$ of the total background. The second most important background is the heavy flavour dominated W+jets background with a share of $\approx 33\%$. The multijet background holds the third position covering $\approx 7\%$ of the background, whereof the electron channel contributes $\approx 62\%$. Minor background contributions come from the WZ diboson production, that comprises the Z decay into a pair of b jets, the Z+jets background and the WW diboson process.
The p_T^W splitting induces a different behaviour between signal and background and among the different background contributions: all background components except for the top are maximal in the first p_T^W bin and decrease continuously with increasing p_T^W. In contrast, the top background as well as the WH signal have their maximum only in the second p_T^W bin and drop afterwards. But the important aspect is the minor decrease of the signal compared to the dominant top background (see also Figure 3.11). This leads to an increasing signal over background ratio S/B with increasing p_T^W. For the fourth p_T^W bin the S/B ratio amounts to ≈ 8.5 times the S/B ratio before p_T^W splitting. This positive development of the S/B ratio is accompanied by a significant increase of the relative statistical uncertainty.
After the detailed discussion on the systematic uncertainties in Section 7 the influence of the p_T^W splitting on the calculated Higgs limits is outlined in Section 8.

Table 6.1.: The event yield in the signal region ($80 \leq m_{b\bar{b}} \leq 150$ GeV) for a WH signal sample ($m_H = 125$ GeV), the background processes and the data after all analysis cuts for the muon channel. The listed uncertainties for the signal and the background merely consider the statistical uncertainties.

	1st p_T^W bin	2nd p_T^W bin	3rd p_T^W bin	4th p_T^W bin	total
WH	2.17 ± 0.06	2.33 ± 0.06	1.55 ± 0.05	0.51 ± 0.03	6.56 ± 0.10
top	126.2	177.8	97.2	3.3	404.4
W+jets	116.1	66.4	28.2	1.8	212.5
MJ	33.6	2.1	0.1	0.0	35.8
WZ	5.5	4.7	3.4	0.6	14.1
Z+jets	6.4	3.9	0.9	0.0	11.3
WW	0.3	0.4	0.1	0.0	1.0
bkg	288.1 ± 13.7	255.4 ± 7.6	130.0 ± 5.4	5.7 ± 1.3	679.2 ± 16.6
S/B	0.008	0.009	0.012	0.089	0.010
data	298	274	116	7	695

Table 6.2.: The event yield in the signal region ($80 \leq m_{b\bar{b}} \leq 150$ GeV) for a WH signal sample ($m_H = 125$ GeV), the background processes and the data after all analysis cuts for the electron channel. The listed uncertainties for the signal and the background merely consider the statistical uncertainties.

	1st p_T^W bin	2nd p_T^W bin	3rd p_T^W bin	4th p_T^W bin	total
WH	1.64 ± 0.05	2.04 ± 0.05	1.62 ± 0.05	0.55 ± 0.03	5.85 ± 0.09
top	111.4	172.8	102.9	4.3	391.4
W+jets	145.8	62.5	31.8	2.9	243.0
MJ	35.7	15.2	6.2	0.8	57.9
WZ	7.0	6.0	4.5	0.5	18.0
Z+jets	2.6	2.1	0.9	0.0	5.6
WW	0.7	0.4	0.3	0.0	1.4
bkg	303.2 ± 26.3	259.0 ± 8.2	146.5 ± 5.9	8.5 ± 1.5	717.3 ± 28.2
S/B	0.005	0.008	0.011	0.065	0.008
data	271	260	136	7	674

Figure 6.9.: The invariant mass $m_{b\bar{b}}$ of the two b tagged jets in the muon channel after all selection cuts before splitting up into the four p_T^W bins.

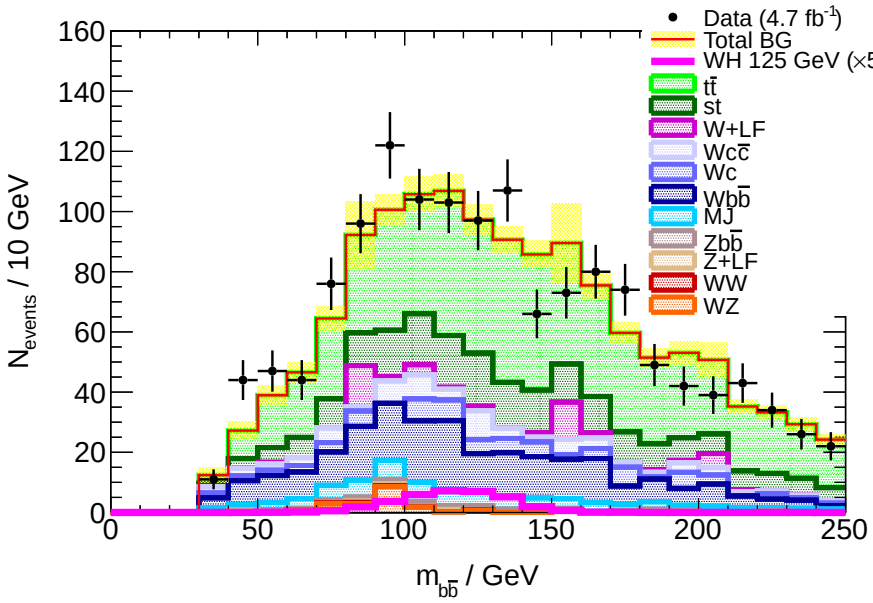

Figure 6.10.: The invariant mass $m_{b\bar{b}}$ of the two b tagged jets in the muon channel after all selection cuts split into four different p_T^W bins ($p_T^W < 50$ GeV, 50 GeV $\leq p_T^W < 100$ GeV, 100 GeV $\leq p_T^W < 200$ GeV, 200 GeV $\leq p_T^W$).

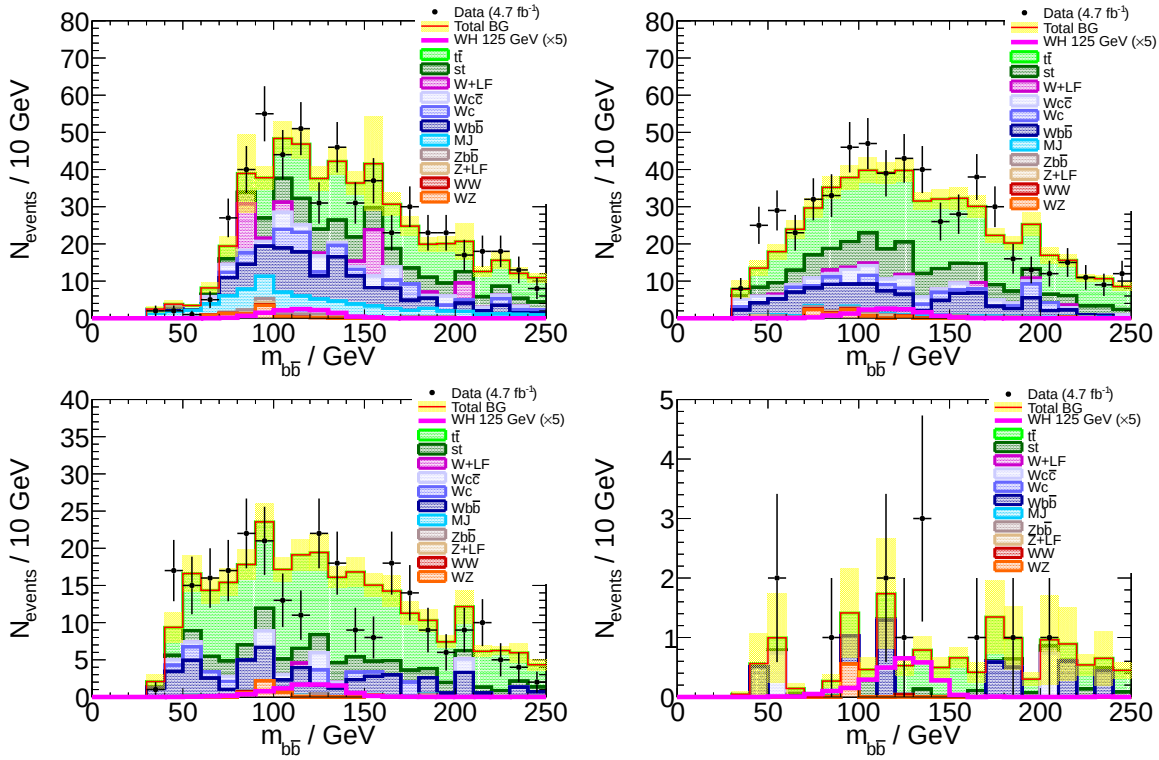

Figure 6.11.: The invariant mass $m_{b\bar{b}}$ of the two b tagged jets in the electron channel after all selection cuts before splitting up into the four p_T^W bins.

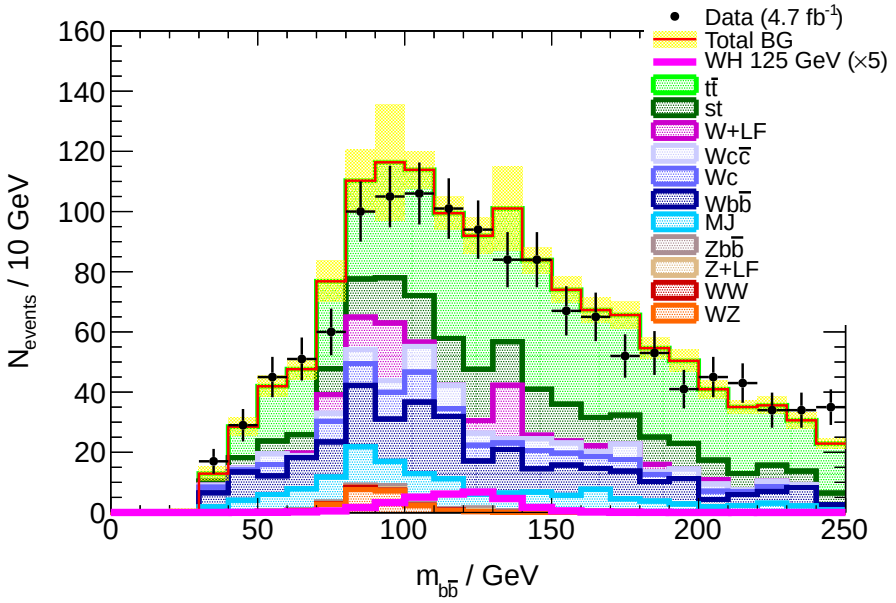

Figure 6.12.: The invariant mass $m_{b\bar{b}}$ of the two b tagged jets in the electron channel after all selection cuts split into four different p_T^W bins ($p_T^W < 50$ GeV, 50 GeV $\leq p_T^W < 100$ GeV, 100 GeV $\leq p_T^W < 200$ GeV, 200 GeV $\leq p_T^W$).

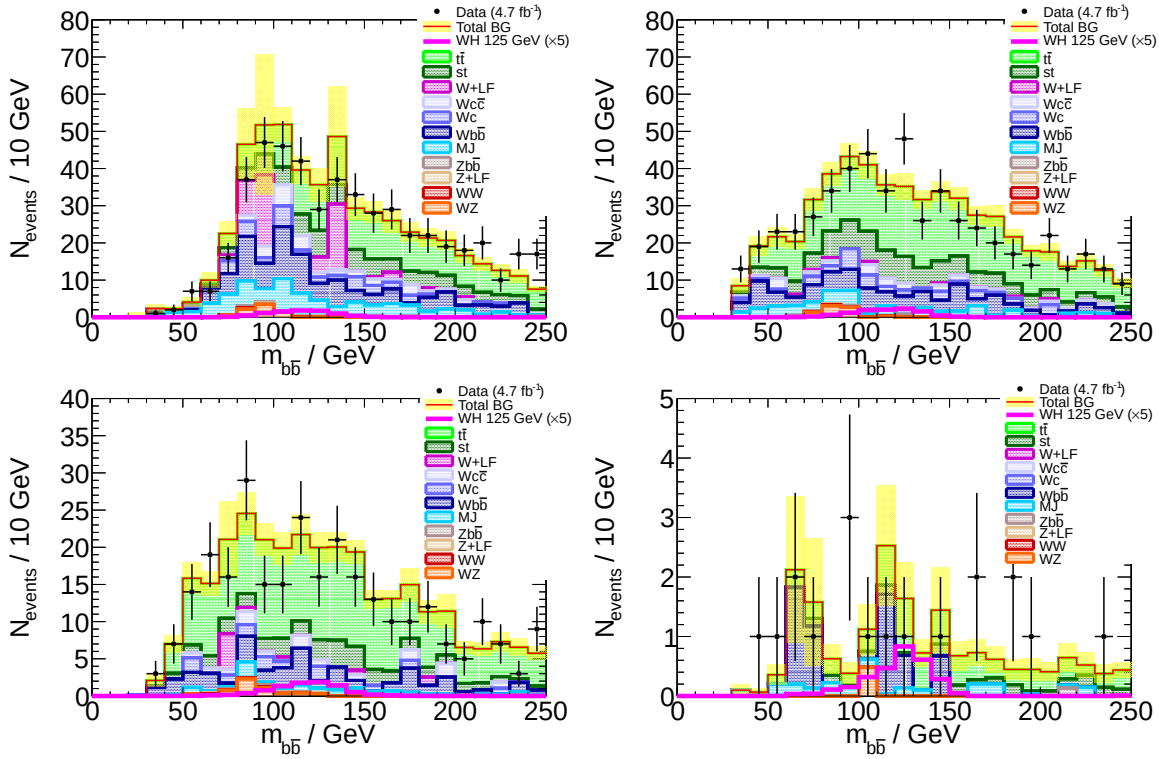

7. Systematic Uncertainties

In the context of the WH analysis, systematic uncertainties σ_{sys} are the experiment-related uncertainties caused by the limited knowledge of the properties of the physics objects, the trigger, and the b tagging, and the limited precision of the luminosity measurement. Further important uncertainties emerge from the various data-driven methods for the background estimation and from the predictions of the cross sections of both the signal and the background processes.
In the first three subsections of this chapter, the different uncertainties are outlined whereas the last part is dedicated to the influence of σ_{sys} on the event yield after all selection cuts.

7.1. Systematic Uncertainties on the Physics Objects and on the Luminosity

All of the physics objects that are considered in the WH analysis suffer from systematic uncertainties, that are studied in detail by the appropriate ATLAS physics performance groups. Representative values of these uncertainties together with their dependence on kinematic quantities are summarized in Table 7.1.

- The selected **muons** are affected by uncertainties on the momentum scale and resolution, and the efficiency to reconstruct and trigger the muon.
  With a value of $\lesssim 1\,\%$, the latter is the most important muon uncertainty [29,44–46].

- For the selected **electrons**, the same uncertainties are considered as for muons. In case of electrons, the uncertainty on the reconstruction efficiency refers to the uncertainty on the efficiency to reconstruct an electron candidate (see 3.1.2). An

additional uncertainty, the uncertainty on the efficiency to identify the electron, has to be accounted for. Since the probability of misidentification is much higher in the calorimeter system than in the muon spectrometer, this uncertainty can not be ignored.
The most important one is the uncertainty on the electron energy resolution with $\sim$ 1.5 %. The uncertainty on the energy scale is much lower for muons than for electrons; the remaining uncertainties are of the same order of magnitude [31,47–49].

- The **jets** suffer from uncertainties on the b-tag efficiency, the jet energy scale (JES), the jet energy resolution (JER), and the jet reconstruction efficiency [35, 40, 61, 62]. The uncertainties on the the b-tag efficiency, the JES, and the JER are the most important experimental uncertainties on the results of the WH analysis.
  The uncertainty on the b-tag efficiency ranges from $\sim$ 6 % for low-energetic jets to $\sim$ 19 % for high energetic jets. It is treated as fully anti-correlated with the uncertainty of the mistag rate.
  The JES uncertainty decreases from $\sim$ 14 % for low-energetic jets in the outer detector region to $\sim$ 3 % for high-energetic central jets. Since there is not yet a dedicated b jet energy scale settled in ATLAS, an additional uncertainty for b-jets is added in quadrature to the nominal JES uncertainty to account for the (not measured) energy of neutrinos emerging in heavy flavour decays inside jets. This additional uncertainty amounts to 2.5 % for jets with $p_T \lesssim 40$ GeV and decreases to 0.76% for jets with $p_T > 600$ GeV.
  The JER uncertainty amounts to 22 % for low-energetic jets and falls to $\sim$ 5 % for high-energetic jets.
  Whereas the uncertainty on the b-tag efficiency increases with an increasing jet energy, the uncertainty on the JES and JER decreases. The rising uncertainty on the b-tag efficiency originates mainly from the decreasing MC sample statistics of high-p_T jets, that is used for the evaluation of the MC b-tag efficiency. Furthermore, the knowledge about the modelling of heavy flavour production and decays becomes more imprecise with increasing jet p_T. The uncertainty on the JES decreases with increasing jet p_T, since the dominant uncertainties for low-p_T jets, i.e. the differences in the event modelling between different MC generators and the differences between the reconstructed jet energy and the energy at generator level, reduce for increasing p_T. For a jet p_T above 100 GeV, the uncertainty on the calorimeter response gets dominant and leads to a rising JES uncertainty for $p_T > 200$ GeV. The JER uncertainty is determined by the JER difference between data and MC and decreases for

increasing jet p_T.
Since the reconstruction of jets is almost fully efficient for $p_T(\text{jet}) > 30$ GeV in both data and MC, the uncertainty affects mainly the low-p_T spectrum of jets and amounts to $< 0.1\,\%$ in this region.

- The uncertainties on the **missing transverse energy $\not{E}_{\mathbf{T}}$** comprise the uncertainty on the separately reconstructed objects, i.e. leptons and jets, and the uncertainty on the additional terms $\not{E}_{\mathrm{T}}^{\mathrm{calo,softjet}}$ and $\not{E}_{\mathrm{T}}^{\mathrm{calo,CellOut}}$ (see Section 3.1.4). The former are evaluated by propagating the uncertainty on the considered physics object to the $\not{E}_{\mathrm{T}}$. The uncertainties on $\not{E}_{\mathrm{T}}^{\mathrm{calo,softjet}}$ and $\not{E}_{\mathrm{T}}^{\mathrm{calo,CellOut}}$ are evaluated by comparing MC samples with a different description of the dead detector material, with a different hadronic shower model, and variations of further MC parameters. An additional uncertainty of 6.6% is introduced to account for the pile-up [37].

- The systematic uncertainty on the **luminosity** was estimated to be 3.9 % for the 2011 dataset [18].

For each of the specified uncertainties, the corresponding physics object is modified according to the recommendations of the ATLAS performance groups and the influence on the signal and background prediction is evaluated. The uncertainties are treated as fully correlated among the different background samples and the signal sample. The normalization factors of the W+jets and the top background are recalculated for each systematic variation, whereas the influence of the systematic variation on the data-driven multijet background can be neglected.
The uncertainty on the luminosity is regarded as normalization uncertainty on the MC samples and is therefore only applied to MC.

7.2. Systematic Uncertainties on the Background Processes

Besides the experimental systematic uncertainties outlined in the previous section, further uncertainties have to be considered for the data-driven background estimates. Uncertainties on the multijet estimate are evaluated in Section 4.2. They are extracted from the study of a multijet-enriched control region. For the muon channel, an uncertainty of $\pm 24\,\%$

Table 7.1.: Overview of the different components of the systematic uncertainties related to the physics objects considered in the WH analysis and the uncertainty on the luminosity [29, 31, 44–49]. The representative values of the uncertainties are listed together with their dependence on kinematic variables.

uncertainty	representative value [%]	dependence
muons		
momentum scale	~ 0.06 ($\eta < 1.05$), ~ 0.2 ($\eta > 2.0$)	η
momentum resolution	< 1	η, p_T
trigger efficiency	$\lesssim 1$	-
reconstruction efficiency	< 0.5	η, p_T
electrons		
energy scale	$\lesssim 1.0$	η, E_T
energy resolution	~ 1.5	η, E_T
trigger efficiency	$\lesssim 1.4$ ($E_T < 25$ GeV), $\lesssim 0.1$ ($E_T > 40$ GeV)	E_T
reconstruction efficiency	0.7	-
identification efficiency	0.4	-
jets		
b-tag efficiency	~ 6 ($p_T < 40$ GeV), ~ 19 ($p_T > 140$ GeV)	p_T
mistag rate	~ 8 ($p_T < 40$ GeV), ~ 55 ($p_T > 140$ GeV)	p_T
energy scale (including b JES)	~ 14 ($p_T < 40$ GeV,$\eta > 4.0$), ~ 3 ($p_T > 150$ GeV,$\eta < 1.0$)	p_T, η
energy resolution	~ 22 ($p_T < 40$ GeV), ~ 5 ($p_T > 150$ GeV)	p_T
reconstruction efficiency	< 0.1 ($p_T < 40$ GeV), ~ 0 ($p_T > 150$ GeV)	p_T
$\not{E}_{\mathrm{T}}$ $\not{E}_{\mathrm{T}}^{\mathrm{calo,softjet}} + \not{E}_{\mathrm{T}}^{\mathrm{calo,CellOut}}$	~ 1.2	-
pile up	6.6	-
Luminosity	3.9	

is assumed for the first p_T^W bin and an uncertainty of $\pm 100\,\%$ for the second to fourth p_T^W bin. The uncertainty in the electron channel is estimated to be $\pm 39\,\%$ for the first p_T^W bin, $\pm 35\,\%$ for the second p_T^W bin, and $\pm 100\,\%$ for the third and fourth p_T^W bin.
Uncertainties on the W+jets flavour fraction fit are listed in Table 5.1 in Section 5.1 and are $\pm 7\,\%$, $\pm 4\,\%$, and $\pm 1\,\%$ for the scaling factors SF_b, SF_c, and SF_{LF}. The uncertainties on SF_b and SF_c are treated independent of each other. The uncertainty on SF_{LF} is small compared to the ones on SF_b and SF_c and is therefore neglected.
The uncertainties on the W+jets flavour fractions as well as the W+jets and top sideband normalization are based on the precision of the fraction fit.
When evaluating the effect on the event yield of the uncertainties on the multijet estimate and on SF_b and SF_c, the sideband fit for W+jets and top is redone for each systematic variation.
The uncertainties on the W+jets and the top normalization itself are outlined in Section 5.2. They amount to $\pm 29\,\%$ for the W+jets component and $\pm 15\,\%$ for the top contribution. The uncertainties on the W+jets and the top component are considered as fully anti-correlated.
For the backgrounds that are described by MC samples and that are not normalized by the data (Z+jets, WW, and WZ) an uncertainty on the theoretical production cross section is taken into account. For the Z+jets production, a cross section uncertainty of $5\,\%$ is assumed [57]. The WW cross section has an uncertainty of $6\,\%$ [64]. The WZ cross section is currently affected by an uncertainty of $6\,\%$ [65].

7.3. Systematic Uncertainties on the Signal Process

Theoretical uncertainties on the various Higgs boson production cross sections as well as on the different branching ratios were studied in detail by the LHC Higgs cross section working group [14]. They account for variations of the factorization and renormalization scale (Scale), and for uncertainties on the strong coupling constant α_s and the parton density functions (PDF). For the Higgs boson mass range between 110 GeV and 130 GeV, the uncertainties on the WH production cross section are listed in Table 7.2. For the branching ratio $BR_{H\to b\bar{b}}$, the estimated uncertainty is $2\,\%$.

The uncertainties on the production cross section and on the branching ratio are combined to one systematic uncertainty. At first the scale uncertainty is symmetrized for each Higgs

Table 7.2.: Systematic uncertainties on the WH production cross section due to variations of the factorization/renormalization scale and variations of the PDF and α_s [14].

m_H [GeV]	σ_{WH} [pb]	$Scale$ [%]	$PDF + \alpha_s$ [%]
110	0.875	$^{+0.3}_{-0.7}$	$\pm$ 3.8
115	0.755	$^{+0.4}_{-0.8}$	$\pm$ 3.9
120	0.656	$^{+0.4}_{-0.7}$	$\pm$ 3.4
125	0.573	$^{+0.2}_{-0.8}$	$\pm$ 3.5
130	0.501	$^{+0.3}_{-0.8}$	$\pm$ 3.5

mass. Secondly, the quadratic mean for the different Higgs masses of both the scale and the $PDF + \alpha_s$ uncertainty is evaluated. Finally, the resulting uncertainties on the scale and on $PDF + \alpha_s$ are added quadratically to the squared uncertainty on the branching ratio $BR_{H\to b\bar{b}}$. Building the square root leads to a total uncertainty of 4.2 %.
The uncertainties as stated in Table 7.2 are inclusive uncertainties on the WH cross section, which is corrected for inclusive NNLO QCD and NLO EW effects. In the ATLAS WH working group, further uncertainties that depend on p_T^W were studied [66]. They comprise a parton level study that evaluates the p_T^W-dependent influence of NLO EW effects. A further study investigates the impact of a different parton showering and NLO QCD corrections on the p_T^W-dependent signal event yield. Both studies assume the differential uncertainties to be independent of the Higgs mass. Adding up the two p_T^W-dependent uncertainties in quadrature together with the inclusive uncertainty of 4.2 % results in the total signal uncertainty listed in Table 7.3. The uncertainty rises from $\pm$4.5 % in the first p_T^W bin to $\pm$10.4 % in the fourth p_T^W bin.

Table 7.3.: The relative systematic uncertainty on the WH signal (m_H = 125 GeV) in dependence of the four p_T^W bins (p_T^W < 50 GeV, 50 GeV $\leq p_T^W <$ 100 GeV, 100 GeV $\leq p_T^W <$ 200 GeV, 200 GeV $\leq p_T^W$) [66].

WH	1st p_T^W bin [%]	2nd p_T^W bin [%]	3rd p_T^W bin [%]	4th p_T^W bin [%]
total unc.	$\pm$4.5	$\pm$5.0	$\pm$5.7	$\pm$10.4

7.4. Impact of the Systematic Uncertainties on the WH Analysis Results

The influence of the various experimental and theoretical systematic uncertainties on the signal and background of the WH analysis are outlined in Tables 7.4 and 7.5. Depicted are the relative deviations from the nominal result (see Tables 6.1 and 6.2) for the combination of the electron and muon channel.
Several uncertainties are merged in the Tables 7.4 and 7.5 by adding the corresponding yield variations in quadrature: all uncertainties affecting the electrons or the muons are combined to one uncertainty, respectively. Furthermore, the $\not{E}_{\mathrm{T}}$ uncertainties on the softjet and the CellOut term are merged (see 7.1). The uncertainty on the background normalization is the total uncertainty on the W+jets flavour fractions SF_b and SF_c together with the uncertainty on the W+jets and top sideband fit. The theory component of the uncertainty refers in case of the signal to the total cross section uncertainty (see Table 7.3) and in case of the background to the cross section uncertainties on the WW, WZ, and Z+jets processes (see Section 7.2).
From the right most column of Table 7.4, that illustrates the systematic uncertainties on the signal before the p_T^W splitting, one can conclude, that the uncertainties on the jets dominate, followed by the ones on the signal cross section and the luminosity. This behaviour holds as well for the different p_T^W bins, except for the first one. In this bin, the uncertainties on the leptons and the $\not{E}_{\mathrm{T}}$ are larger than the ones on the cross section and the luminosity and follow closely the ones on the jets. This leads to the largest uncertainties in the first and the last p_T^W bin: $\sigma_{sys,\mathrm{Signal}}^{1.p_T^W\text{-bin}} = ^{+23.6}_{-22.6}$ % and $\sigma_{sys,\mathrm{Signal}}^{4.p_T^W\text{-bin}} = ^{+23.8}_{-22.2}$ %.
The total uncertainty on the prediction of WH signal events is for all p_T^W bins clearly dominated by the systematic uncertainties, which are an order of magnitude larger than the uncertainties due to the limited statistics of the signal sample.
Due to the re-evaluated sideband fit of the W+jets and top background for every uncertainty component, the importance of the individual uncertainties is slightly different for the background uncertainties (see Table 7.5): Before the p_T^W splitting, the uncertainties are still dominated by the jet uncertainties, which are, however, smaller than the jet uncertainties on the signal, and which are closely followed by the uncertainties on W+jets and top background estimates and the leptons. The uncertainty on the luminosity is reduced by the data-driven background techniques. Since the background contributions from Z+jets, WW, and WZ are relatively small, the cross section uncertainties on these processes do not have a significant impact. The first p_T^W bin suffers mostly from the uncertainty on

the jet energy resolution. In the second p_T^W bin, the jet uncertainty is still the largest one, but it is close to the uncertainties on the leptons and the data-driven background estimate/normalization. It is the bin with the lowest uncertainties. In contrast to the further bins, the third one is dominated by the multijet uncertainty. In this bin, the multijet contribution is not yet negligible (see Tables 6.1 and 6.2), but is already affected by an uncertainty of 100 %. The last p_T^W bin suffers from large uncertainties on jets, leptons, and $\not{E}_{\mathrm{T}}$. As for the signal process, the first and the last p_T^W bin of the background have the largest uncertainties: $\sigma_{sys,\mathrm{Bkg}}^{1.p_T^W\text{-bin}}$ [%] $=^{+21.5}_{-22.7}$ and $\sigma_{sys,\mathrm{Bkg}}^{4.p_T^W\text{-bin}}$ [%] $=^{+16.4}_{-20.7}$. In the first and the third bin, the systematic uncertainty is significantly larger than the uncertainty due to the limited sample statistics. In the two further bins, their values are of comparable size. Besides the p_T^W dependence of several uncertainties, the uncertainties on the jets tend to modify the shape of the $m_{b\bar{b}}$ distribution inside the different bins. Figure 7.1 (7.2) depict the $m_{b\bar{b}}$ distributions for the signal (background) in the signal range ($80 \leq m_{b\bar{b}} \leq 150$ GeV) before and after scaling the three important jet uncertainties up/down: the b-tag efficiency, the jet energy scale, and the jet energy resolution. All distributions are normalized to unity in every p_T^W bin. For both the signal and background, the most important influence on the $m_{b\bar{b}}$ shape has the variation of the jet energy resolution. The uncertainty on the jet energy scale has also a significant impact, whereas the variation of the b-tag efficiency does not significantly modify the $m_{b\bar{b}}$ shape.

Table 7.4.: The relative variations of the event yield of the WH signal process (m_H = 125 GeV) after all selection cuts due to the systematic variations of the corresponding uncertainty. Only the signal region ($80 \leq m_{b\bar{b}} \leq 150$ GeV) is considered. The combination of the electron and muon channel is shown. The last column refers to the event yield before p_T^W splitting. The uncertainty symbolised by "stat" is the uncertainty due to the limited sample statistics.

unc. / p_T^W bin	1st bin [%]	2nd bin [%]	3rd bin [%]	4th bin [%]	total [%]
muon	+11.9	+0.8	+3	+1.3	+2.9
	−11.6	−0.9	−2.7	−1.0	−2.8
electron	+9.1	+0.8	+3.3	+1.4	+1.7
	−9.0	−1.3	−2.9	−1.1	−1.7
jet					
b-tag. eff.	+11.4	+13.1	+16.0	+16.9	+13.6
	−11.3	−11.7	−14.7	−16.3	−12.8
energy scale	+9.4	+3.9	+2.7	+10.1	+5.8
	−5.1	−0.3	−6.1	−6.9	−0.7
energy res.	+2.4	+1.8	+1.9	+7.3	+1.2
	−1.4	−1.7	−2.1	−7.3	−2.2
rec. eff.	±0.01	±0.2	±0.1	±0.4	±0.07
total	+15.0	+13.8	+16.4	+21.0	+14.9
	−12.5	−11.9	−16.1	−19.1	−13.0
$\not{E}_{\mathrm{T}}$	+8.4	+1.3	+3.4	+1.4	+1.1
	−10.1	−1.4	−3.2	−0.4	−1.8
theory	±4.5	±5	±5.7	±10.4	±5.5
lumi	±3.9	±3.9	±3.9	±3.9	±3.9
total	+23.6	+15.3	+18.6	+23.8	+16.7
	−22.6	−13.6	−18.2	−22.2	−15.1
stat + sys	+2.9 +23.6	+2.5 +15.3	+3.2 +18.6	+5.7 +23.8	+1.5 +16.7
	−2.9 −22.6	−2.5 −13.6	−3.2 −18.2	−5.7 −22.2	−1.5 −15.1

Table 7.5.: The relative variations of the event yield of the total background after all selection cuts due to the systematic variations of the corresponding uncertainty. Only the signal region ($80 \leq m_{b\bar{b}} \leq 150$ GeV) is considered. The combination of the electron and muon channel is shown. The last column refers to the event yield before p_T^W splitting. The uncertainty symbolised by "stat" is the uncertainty due to the limited sample statistics.

unc. / p_T^W bin	1st bin [%]	2nd bin [%]	3rd bin [%]	4th bin [%]	total [%]
muon	+4.6	+3.0	+4.5	+9.6	+2.4
	−4.6	−3.1	−4.8	−9.8	−2.3
electron	+5.1	+3.1	+4.6	+7.7	+2.9
	−4.9	−3.5	−3.8	−6.4	−2.8
jet					
b-tag. eff.	−1.1	−1.8	−0.3	−2.7	−1.1
	−3.1	−0.3	−1.7	−5.6	−1.8
energy scale	+2.0	+2.9	+6.7	+3.9	+1.6
	−5.6	−2.0	−6.2	−9.9	−0.3
energy res.	+17.7	+3.1	+6.8	+4.8	+5.1
	−17.7	−3.1	−6.8	−6.8	−4.9
rec. eff.	±1.8	±1.3	±1.2	±0.5	±1.5
total	+17.9	+4.7	+9.6	+6.8	+5.6
	−18.9	−3.9	−9.4	−13.3	−5.5
$\not{E}_{\mathrm{T}}$	+4.8	+0.5	+3.5	+6.2	+1.5
	−6.1	−0.9	-3.0	−6.9	−2.2
multijet	+1.6	+2.6	+1.4	+0.3	+1.9
	−1.0	−0.6	−1.6	−4.7	−1.0
Bkg. norm.	+7.7	+3.3	+4.6	+2.8	+2.5
	−8.0	−2.9	−4.2	−3.8	−2.7
theory	+2.1	+2.6	+2.4	+3.6	+2.4
	−2.2	−2.8	−2.6	−4.0	−2.5
lumi	+1.2	+1.5	+1.4	+2.0	+1.3
	−1.3	−1.6	−1.6	−2.4	−1.5
total	+21.5	+8.5	+13.4	+16.4	+8.3
	−22.7	−7.8	−13.0	−20.7	−8.3
stat + sys	+6.7 +21.5	+3.1 +8.5	+4.1 +13.4	+20.2 +16.4	+3.2 +8.3
	−6.7 −22.7	−3.1 −7.8	−4.1 −13.0	−20.2 −20.7	−3.2 −8.3

Figure 7.1.: The shape variation of the invariant mass $m_{b\bar{b}}$ of the signal sample (m_H = 125 GeV) in the signal region ($80 \leq m_{b\bar{b}} \leq 150$ GeV) after scaling the the b-tag efficiency, the jet energy scale, or the jet energy resolution up/down. The invariant mass is split into four different p_T^W bins ($p_T^W < 50$ GeV, 50 GeV $\leq p_T^W < 100$ GeV, 100 GeV $\leq p_T^W < 200$ GeV, 200 GeV $\leq p_T^W$). The distributions are normalized to unity in each p_T^W bin.

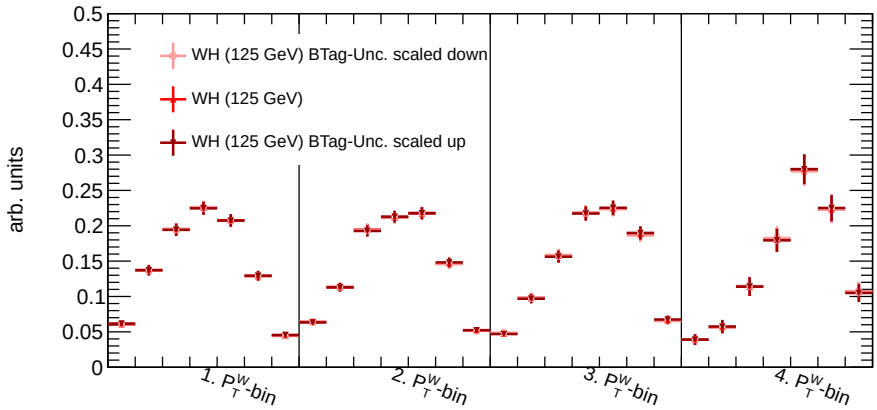

(a) The b-tag efficiency is scaled up/down.

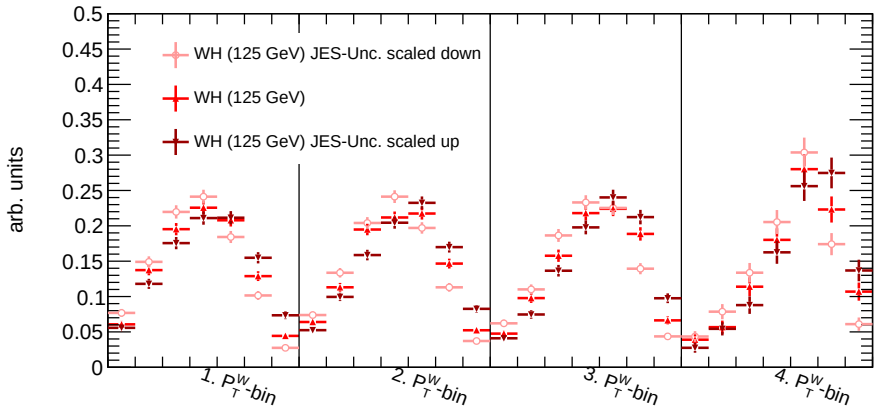

(b) The jet energy scale is scaled up/down.

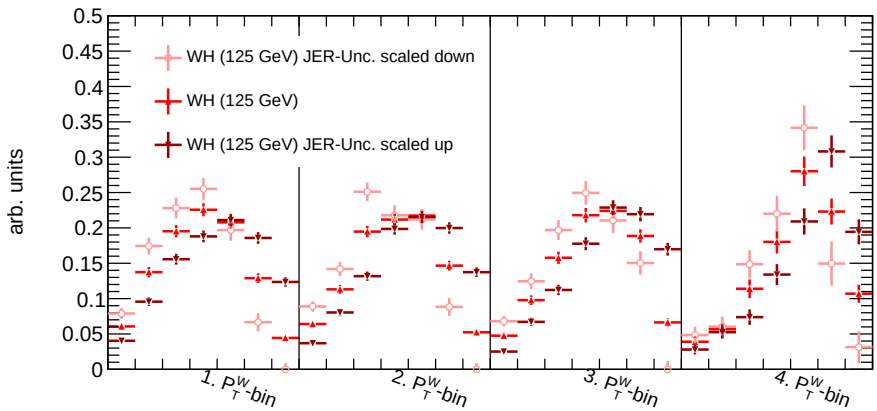

(c) The jet energy resolution is scaled up/down.

Figure 7.2.: The shape variation of the invariant mass $m_{b\bar{b}}$ of the total background in the signal region ($80 \leq m_{b\bar{b}} \leq 150$ GeV) after scaling the the b-tag efficiency, the jet energy scale, or the jet energy resolution up/down. The invariant mass is split into four different p_T^W bins ($p_T^W < 50$ GeV, 50 GeV $\leq p_T^W < 100$ GeV, 100 GeV $\leq p_T^W < 200$ GeV, 200 GeV $\leq p_T^W$). The distributions are normalized to unity in each p_T^W bin.

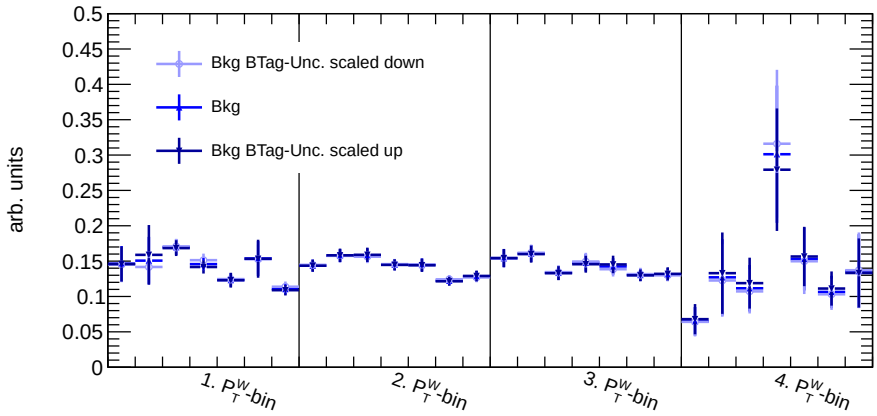

(a) The b-tag efficiency is scaled up/down.

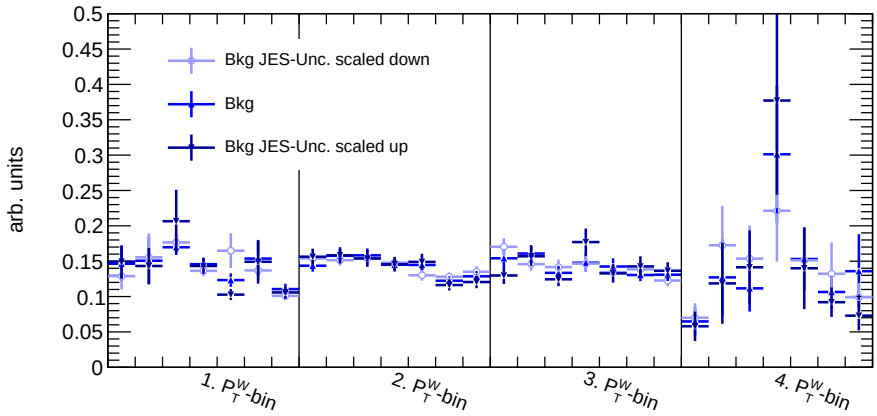

(b) The jet energy scale is scaled up/down.

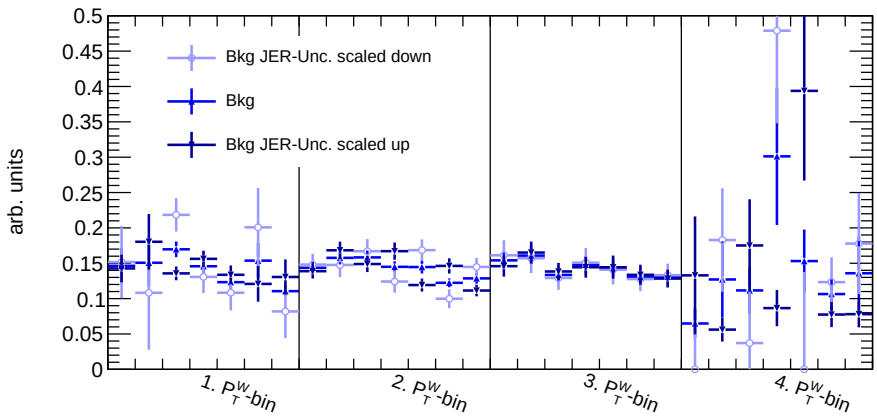

(c) The jet energy resolution is scaled up/down.

8. Exclusion Limit on the SM Higgs Cross Section

The search for the Higgs boson in the WH channel is a search for a small signal over a large background. The so-called CLs method provides a convenient approach to calculate meaningful limits under these conditions. The first section gives a short introduction on the concept of CLs limits, which is the commonly used method for the calculation of Higgs limits in ATLAS. The information given in this section is based on [67, 68]. In the second section, the CLs method is applied to the WH analysis.

8.1. CLs Method

The construction of exclusion limits for the Higgs search can be interpreted as a hypothesis testing: The null hypothesis assumes the absence of a signal, whereas the alternative hypothesis assumes the existence of a signal. As a first step, it has to be decided, whether the statistical analysis should be based simply on the number of events after all analysis cuts n, or whether the number of events n_i in the different bins i of a histogram are considered, that describes convenient observables x. In case of the WH analysis, x corresponds to the invariant mass of a pair of b-tagged jets $m_{b\bar{b}}$. In the first case, the statistical analysis is called a "counting experiment", in the latter case it is denoted as "shape analysis". Secondly, a so-called test statistic q is needed. It is a function of the selected observable(s), the model parameter(s) (which is in case of a Higgs search the signal strength) and the number of expected signal $s(x)$ and background $b(x)$ events. In the case of the signal+background hypothesis, the signal strength μ is equal to 1, whereas for the background only hypothesis μ is zero. The value of the test statistic indicates whether the experimental result of the analysis is more signal (and less background) or less signal (and more background) like. Finally, certain modalities of the hypothesis test have to be

determined, e.g. the possible range of the model parameter(s) or the confidence level CL at which values of the model parameter(s) are considered to be excluded.

8.1.1. Test Statistic

In ATLAS, the definition of the test statistic q is based on a frequentist likelihood function $L(\mu, \boldsymbol{\Theta})$:

$$L(\mu, \boldsymbol{\Theta}) = \prod_{\mathbf{i=1}}^{\mathbf{N}} \frac{\mathbf{e}^{-(\mu \mathbf{s_i} + \mathbf{b_i})} (\mu \mathbf{s_i} + \mathbf{b_i})^{\mathbf{n_i}}}{\mathbf{n_i}!} \mathbf{G}(\boldsymbol{\Theta}) \tag{8.1}$$

As defined in Section 8.1, the parameter μ is the model parameter of the hypothesis test, i.e. the signal strength. The nuisance parameters $\boldsymbol{\Theta}$ are all parameters, which are not of interest but influence the hypothesis test. All systematic uncertainties are considered as nuisance parameters. N is the number of different channels, i.e. the number of bins of a histogram. n_i is the number of observed data events. s_i (b_i) is the expected number of signal (background) events in bin i. s_i and b_i depend on Θ. A further histogram of function $G(\Theta)$ can be introduced in $L(\mu, \boldsymbol{\Theta})$ with the intention to constrain the nuisance parameters Θ.
To test the hypothesis for a fixed parameter μ, the profile likelihood ratio is built:

$$\lambda(\mu) = \frac{L(\mu, \hat{\hat{\boldsymbol{\Theta}}})}{L(\hat{\mu}, \hat{\boldsymbol{\Theta}})} \tag{8.2}$$

$\hat{\hat{\boldsymbol{\Theta}}}$ describes the value of $\boldsymbol{\Theta}$ that maximizes L for the fixed value of μ. In contrast, $\hat{\mu}$ and $\hat{\boldsymbol{\Theta}}$ are the values that maximizes L independently of each other. The values of $\lambda(\mu)$ lie between 0 and 1 by construction. A value close to 1 implies good agreement between the experimental result and the hypothesized value of μ. The lower the value of $\lambda(\mu)$, the worse is the compatibility.
A general form of the test statistic is defined by:

$$q_\mu = -2 \ln \lambda(\mu) \tag{8.3}$$

The higher the value of q_μ, the higher is the incompatibility between the data and the hypothesis μ. The level of disagreement is quantified by the p value, that integrates all

values of q_μ that are equal or less compatible with the observed value $q_{\mu,\text{obs}}$:

$$p = \int_{q_\mu,\text{obs}}^{\infty} f(q_\mu|\mu) dq_\mu \tag{8.4}$$

The function $f(q_\mu|\mu)$ is the probability density function (pdf) of q_μ. Usually, it is calculated by means of Monte-Carlo pseudo-experiments using the Equations 8.2 and 8.3. The subscript μ in $(q_\mu|\mu)$ refers to the tested hypothesis of μ and is found in the numerator(s) of Equation 8.2. The second parameter μ in $f(q_\mu|\mu)$ refers to the mean value $\mu s_i + b_i$ of a Poisson distribution. Random values of n_i are produced by pseudo-experiments following this Poisson distribution. In ATLAS, the current approach uses an asymptotic formula for q_μ that leads to an analytic expression of $f(q_\mu|\mu)$. In this way, the demanding pseudo-experiments can be avoided.

8.1.2. Definition of CLs

To quantify the compatibility of a measurement with the signal+background hypothesis ($\mu = 1$) the p value can be used as defined in Equation 8.4.

$$p_{s+b} = \int_{q_{s+b},\text{obs}}^{\infty} f(q_{s+b}|s+b) dq_{s+b} \tag{8.5}$$

The larger the value of p_{s+b}, the larger is the probability of the signal+background hypothesis.
An example of the probability density function $f(q_{s+b}|s+b)$ together with the observed value $q_{s+b,\text{obs}}$ and the p value p_{s+b} is depicted in Figure 8.1. The smaller the value of $q_{s+b,\text{obs}}$, the better is the compatibility of the experimental outcome with the signal+background hypothesis. In the statistical analysis of the Higgs search in the WH channel, which is a small (positive) signal together with a large background, the following situation can occur: The observed number of events is significantly smaller than the expected number of background events. This leads to a small value of p_{s+b}, equivalent to a strong exclusion of the signal+background hypothesis. The exclusion of the signal is in this case even more pronounced than in the case of a decent agreement between data and the background expectation, although a downward fluctuation of the background does not provide more information on the signal exclusion. To get even in the outlined situation a meaningful

statistical result, not only p_{s+b}, but also p_b has to be taken into account:

$$p_b = \int_{-\infty}^{q_{s+b,\mathrm{obs}}} f(q_{s+b}|b) dq_{s+b} \tag{8.6}$$

The p value p_b describes the compatibility of the experimental result with the background-only pdf $f(q_{s+b}|b)$. The test statistic and the tested hypothesis are the same as for p_{s+b}. The smaller the value of p_b the better is the compatibility between the experimental data and the background expectation. Figure 8.1 depicts the pdf $f(q_{s+b}|b)$ and the p value p_b. The p value p_{s+b} is now replaced by CL_s that depends on both p_{s+b} and p_b. It is defined by:

$$CL_s = \frac{p_{s+b}}{1 - p_b} \tag{8.7}$$

Though a downward fluctuation of the background leads to a smaller value of p_{s+b}, this is compensated in the CL_s definition by a larger value of p_b and therefore a reduced value of $1 - p_b$.

Instead of calculating p values for the fixed value $\mu = 1$, a threshold α (e.g. 0.05) can be defined to determine the corresponding range of μ values, for which hold:

$$CL_s = \frac{p_{\mu s+b}}{1 - p_b} \overset{!}{\leq} \alpha \tag{8.8}$$

These values of μ are then excluded at a confidence level CL of $1 - \alpha$. The lowest (highest) value of μ satisfying $CL_s \leq \alpha$ is called the lower (upper) confidence limit at $1 - \alpha$. In Equation 8.8, CL_s is defined as alternative to the p value p_{s+b}. This means, the signal+background hypothesis is excluded at $CL = 95$ %, if $CL_s \leq 0.05$. The definition of the exclusion of the signal hypothesis at the confidence level CL using CL_s is in case of a downward fluctuation more meaningful than to define it only via p_{s+b}, since the downward fluctuation of the background weakens the exclusion power compared to the case, where no downward fluctuation arises. For decreasing values of p_b, what happens when the signal+background pdf and the background pdf get more and more distinct, both definitions become similar. Systematic uncertainties broaden the pdf's $f(q_{s+b}|s + b)$ and $f(q_{s+b}|b)$ and therefore increase the overlap of $f(q_{s+b}|s + b)$ and $f(q_{s+b}|b)$. The larger the overlap, the weaker becomes the exclusion on the bases of CL_s.

As a drawback, the exclusion of the signal by $1 - CL_s$ is more conservative than the exclusion by $1 - p_{s+b}$, since it excludes a smaller range of model parameters and the false exclusion of the signal is normally smaller than $1 - CL$.

Besides the observed limits, that are calculated using the observed number of events in data, the expected sensitivity of the experiment is of interest. For these expected limits,

the observed number of events in data is replaced by the expected number of events from simulated data. In case of exclusion limits, the simulated data contains no contribution from the signal. Therefore, the expected exclusion limits quantify the range of μ values that can be excluded under the assumption of background-only data.

Figure 8.1.: The pdf's $f(q_{s+b}|s+b)$ and $f(q_{s+b}|b)$ (symbolized by $f(q|s+b)$ and $f(q|b)$ in the figure) for the signal+background hypothesis describing the probability of signal+background results and background-only results, respectively. Furthermore, the observed test statistic $q_{s+b,\mathrm{obs}}$ (q_{obs} in the figure) and the p values p_{s+b} and p_b are shown [67].

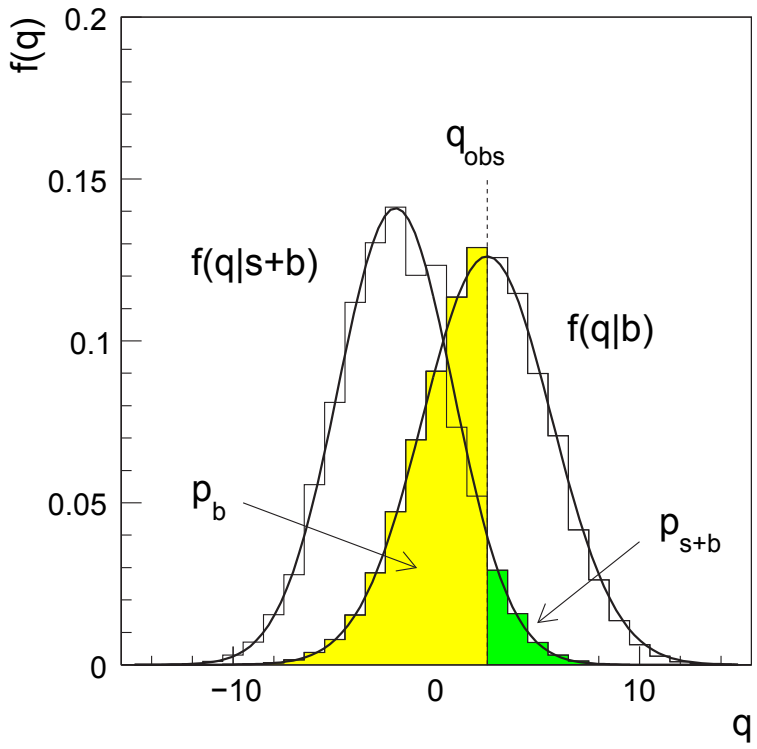

8.2. Exclusion Limit in the WH $\rightarrow$ lνb$\bar{\text{b}}$ Channel

The exclusion limit for the WH analysis follows the ATLAS recommendation and uses the CLs approach as defined in Equation 8.8 in the previous section. The threshold α is set to 0.05 to derive a confidence limit at 95 %. The strength parameter μ corresponds to the multiples of the ratio σ/σ_{WH}. Separate limits are computed for the Higgs masses $m_H = 110, 115, 120, 125, 130$ GeV. The limits are calculated inside the RooStats framework [69]. It is a project inside ROOT [23], that provides dedicated statistical tools especially for the evaluation of exclusion limits and discoveries.
For the WH analysis, the likelihood function as illustrated in Equation 8.1 is formed by the histogram bins of the invariant mass distribution $m_{b\bar{b}}$ after all selection cuts for the WH signal process and the background. Each bin covers 10 GeV of the $m_{b\bar{b}}$ distribution. Only the signal range ($80 \leq m_{b\bar{b}} \leq 150$ GeV) is considered. To raise the sensitivity, the $m_{b\bar{b}}$ distribution is split into the four p_T^W bins ($p_T^W < 50$ GeV, 50 GeV $\leq p_T^W < 100$ GeV, 100 GeV $\leq p_T^W < 200$ GeV, 200 GeV $\leq p_T^W$). Therefore the histogram that is provided to RooStats consists of 28 bins: seven bins for each p_T^W bin.
The systematic uncertainties present in the analysis are treated as nuisance parameters Θ. They are constrained by unit Gaussian distributions. To be able to constrain Θ, the information has to be provided, how the analysis results changes under the up and downward variations of each systematic uncertainty. Two different types of uncertainties are distinguished: rate uncertainties that change mainly the event yield after the selection cuts, and shape uncertainties that significantly change the shape of the provided distribution. For uncertainties that influence both the shape and the rate significantly, both uncertainties are regarded. Since all p_T^W bins are provided in only one histogram, the impact on the shape comprises the change of the $m_{b\bar{b}}$ shape inside one p_T^W bin as well as the significant dependence of p_T^W itself. In the present analysis, the uncertainties on jets (b-tag efficiency, JES, JER) are treated as both flat and shape uncertainties on the background and the signal. For the signal, moreover the theoretical uncertainty on the cross section is treated as rate and shape uncertainty. All further uncertainties are only considered as rate uncertainties. Details on the impact of the various uncertainties are outlined in Section 7.4. Further nuisance parameters are introduced to account for the uncertainty due to the limited sample statistics. They are constrained by Poisson terms.
The observed and expected limits on μ for the considered Higgs boson mass range are depicted in Figure 8.2 and listed in Table 8.1: The best exclusion limit is reached for $m_H = 110$ GeV with a value of $\mu_{obs} = 4.8$. Since the production cross section decreases for increasing masses m_H and the background is almost flat in the $m_{b\bar{b}}$ signal region, the ex-

clusion limit weakens to $\mu_{obs} = 12.2$ for $m_H = 130$ GeV. The observed limits lie within the $\pm 1\sigma$ range of the expected limits μ_{expec} that ranges from $\mu_{expec} = 5.8$ for $m_H = 110$ GeV to $\mu_{expec} = 11.7$ for $m_H = 130$ GeV.

Figure 8.3a and Table 8.2a show the exclusion limits when ignoring the systematic uncertainties due to the limited sample statistics: Averaged over the considered Higgs mass range, the observed (expected) limits improve by 13.9 % (20.9 %) relative to the original limits.

The exclusion limits derived by ignoring any any systematic uncertainties are illustrated in Figure 8.3b and are listed in Table 8.2b: Averaged over the considered Higgs mass range, the observed (expected) limits improve by 60.6 % (50.8 %) compared to the original limits. The fact that the observed limits μ_{obs} are smaller than the expected limits μ_{expec} originates in the slightly higher total number of background events than data events (see Tables 6.1 and 6.2).

Figure 8.3c together with Table 8.2c show the derived limits without p_T^W splitting but considering all systematic uncertainties. They illustrate the advantage of the p_T^W splitting in comparison to the $m_{b\bar{b}}$ distribution without splitting: Averaged over the considered Higgs mass range, the observed (expected) limits get worse by 55.3 % (50.1 %) relative to the original limits when abandoning the splitting procedure.

With the presented analysis, the SM Higgs boson can not be excluded in the considered mass range $110 \leq m_H \leq 130$ GeV. More collision data, larger statistics of the Monte-Carlo samples and a deeper understanding of the physics objects to decrease the systematic uncertainties are necessary to improve the sensitivity of this analysis and to be able to measure the coupling strength between the discovered Higgs-like particle and b quarks.

Figure 8.2.: The observed and expected exclusion limits on the Higgs boson signal strength $\mu = \sigma/\sigma_{WH}$ at 95 % CL as function of the hypothesized Higgs boson mass m_H.

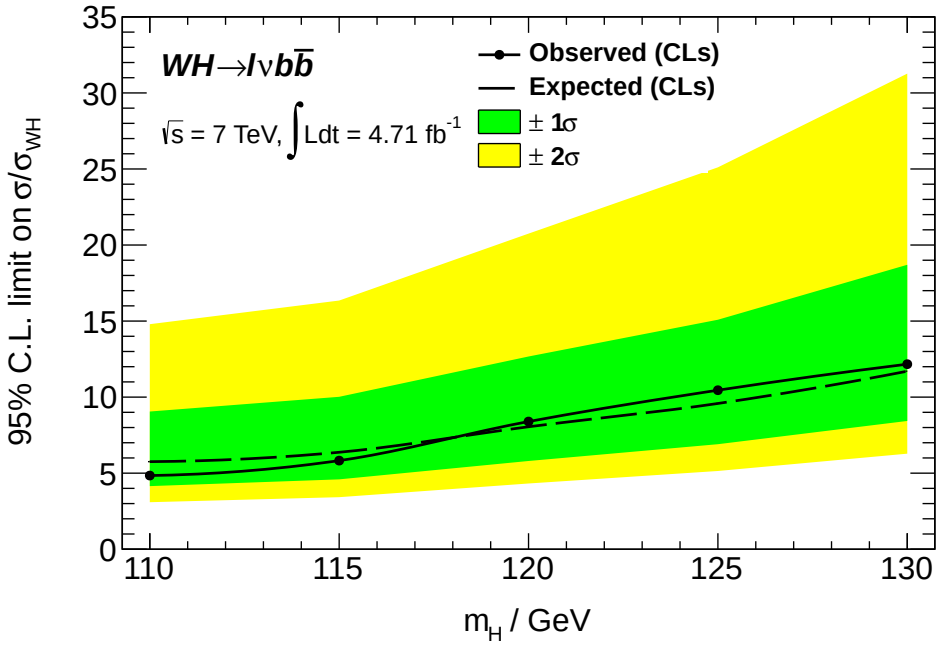

Figure 8.3.: The observed and expected exclusion limits on the Higgs boson signal strength $\mu = \sigma/\sigma_{WH}$ at 95 % CL as function of the hypothesized Higgs boson mass m_H when applying the following modifications to the nominal limit procedure:

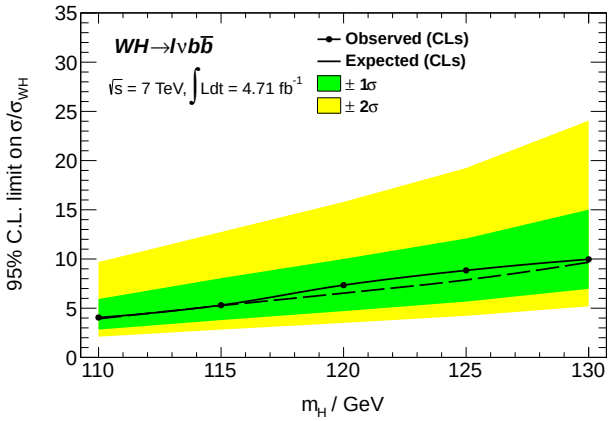

(a) without considering systematic uncertainties due to the limited sample statistics.

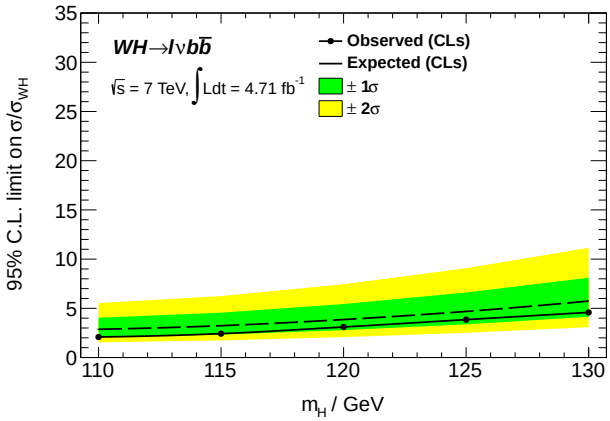

(b) without considering any systematic uncertainties.

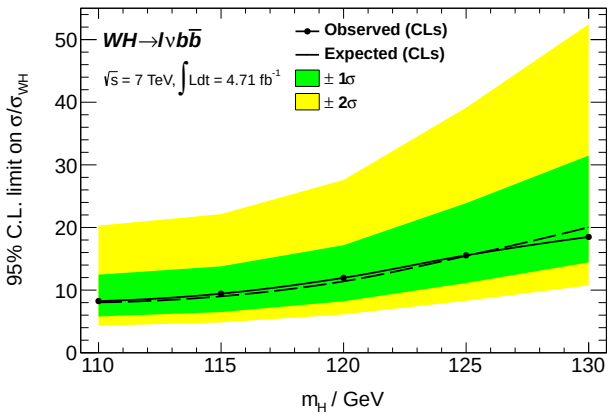

(c) without splitting the invariant mass $m_{b\bar{b}}$ into different p_T^W bins.

Table 8.1.: The observed and expected exclusion limits on the Higgs boson signal strength $\mu = \sigma/\sigma_{WH}$ at 95 % CL as function of the hypothesized Higgs boson mass m_H.

m_H [GeV]	obs.	exp.
110	4.8	5.8
115	5.8	6.4
120	8.4	8.1
125	10.4	9.6
130	12.2	11.7

Table 8.2.: The observed and expected exclusion limits on the Higgs boson signal strength $\mu = \sigma/\sigma_{WH}$ at 95 % CL as function of the hypothesized Higgs boson mass m_H when applying the following modifications to the nominal limit procedure:

(a) without considering systematic uncertainties due to the limited sample statistics.

m_H [GeV]	obs.	exp.
110	4.1	3.9
115	5.3	5.3
120	7.3	6.5
125	8.8	7.9
130	10.0	9.7

(b) without considering any systematic uncertainties.

m_H [GeV]	obs.	exp.
110	2.1	2.9
115	2.4	3.2
120	3.1	3.9
125	3.9	4.7
130	4.6	5.7

(c) without splitting the invariant mass $m_{b\bar{b}}$ into different p_T^W bin.

m_H [GeV]	obs.	exp.
110	8.2	8.0
115	9.4	9.0
120	12.0	11.4
125	15.5	15.4
130	18.5	20.0

9. Summary and Outlook

In this thesis a search for the standard model Higgs boson in the channel $WH \to l\nu b\bar{b}$ is presented. It is performed on the 2011 ATLAS dataset from pp collisions at $\sqrt{s} = 7$ TeV comprising an integrated luminosity of 4.7 fb^{-1}. The signature of interest contains exactly one isolated lepton, missing transverse energy $\not{E}_{\mathrm{T}}$ of more than 25 GeV and a transverse mass of the W boson of more than 40 GeV. These cuts are targeted to reconstruct the leptonically decaying W boson, that is supposed to be produced in association with the Higgs boson. As signature of the Higgs boson, exactly two jets are required, both of which are b-tagged with an efficiency of ≈ 70 % per jet.

The multijet background for both the electron and muon channel is estimated by a data-driven method. It is based on a template fit to the $\not{E}_{\mathrm{T}}$ distribution in data by two templates: one is the multijet template consisting of collision data from a multijet enriched region, the second one consists of all non-multijet background described by simulated data. The number of multijet events after all selection cuts is 76.2 ± 22.9 for the muon channel and 134.6 ± 61.8 for the electron channel.

Since the flavour fractions of the W+jets background are insufficiently described by Monte-Carlo simulations, they are estimated by fitting three different templates to the distribution of the b-tag weight: one for $W + b\bar{b}$, one for $W + c(\bar{c})$, and one for W+light-flavour. After weighting the different flavour fraction with the derived scaling factors, the total W+jets background is fitted together with the top background ($t\bar{t}$ and single top) in the signal-free sideband regions of the invariant mass $m_{b\bar{b}}$. The top background is scaled up by a scaling factor 1.13 ± 0.15 (stat), whereas the W+jets background is slightly scaled down by 0.92 ± 0.29 (stat).

The remaining background components from Z+jets, WW, and WZ production are described by dedicated Monte-Carlo samples normalized using theoretical cross sections. Together with the estimated background contributions for multijet, top, and W+jets production, the total background prediction is 1396.5 ± 44.7 (stat) ± 115.9 (sys) events compared to 12.4 ± 0.2 (stat) $^{+2.1}_{-1.9}$ (sys) predicted WH signal events at $m_H = 125$ GeV for the combined electron and muon channels. This corresponds to a S/B ratio of $S/B = 0.9$ %.

The number of data events is 1369. To become more sensitive to the signal, differences in the p_T^W distributions of signal and background events are utilised: Since the p_T^W distribution of the WH signal decreases less steeply than the background, the selected events are split into four p_T^W bins: $p_T^W < 50$ GeV, $50 \leq p_T^W < 100$ GeV, $100 \leq p_T^W < 200$ GeV, and $p_T^W \geq 200$ GeV. The S/B ratio increases from $S/B = 0.7$ % in the first bin to $S/B = 7.7$ % in the last bin.

Systematic uncertainties cover experimental and theoretical uncertainties as well as uncertainties on the background estimate. The largest uncertainties for both the signal and background processes are the uncertainties on jets (b-tag efficiency / mistag rate, jet energy scale, jet energy resolution).

In the absence of an excess, exclusion limits on the Higgs boson signal strength $\mu = \sigma/\sigma_{WH}$ are calculated using the CL_s method, which is especially devoted for the search of a small signal compared to a large background. The statistical analysis is performed using the invariant mass $m_{b\bar{b}}$ split into the four p_T^W bins. The limits are calculated in the Higgs boson mass range 110 GeV $\leq m_H \leq$ 130 GeV in steps of 5 GeV. The best limit is achieved for the lowest mass: $\mu_{obs} \geq 4.8$ is excluded at 95 % CL for a Higgs boson mass $m_H = 110$ GeV. For $m_H = 130$ GeV the observed limit is $\mu_{obs} \geq 12.2$. These observed limits are within one standard deviation of the expected limits indicating a good description of the background processes. The expected limits are: $\mu_{expec} \geq 5.8$ for $m_H = 110$ GeV and $\mu_{expec} \geq 11.7$ for $m_H = 130$ GeV. The sensitivity suffers significantly from the large systematic uncertainties: For a Higgs boson mass $m_H = 110$ GeV, the observed (expected) limit improves to $\mu_{obs} \geq 2.1$ ($\mu_{expec} \geq 2.9$) compared to the original limit when ignoring any systematic uncertainties.

Since March 2012, ATLAS has already collected an integrated luminosity of more than 15.4 fb^{-1} at a centre-of-mass energy of 8 TeV. The increasing amount of collision data will improve the sensitivity in the $WH \to l\nu b\bar{b}$ channel. However, not only the larger set of collision data will enhance the sensitivity. Efforts are also ongoing to reduce the systematic uncertainties on jets by introducing a separate energy scale for b jets, by considering the muons inside jets from semi-leptonic b decays, and by using in-situ techniques for the JES calibration. A further b-tagging calibration technique based on $t\bar{t}$ events is established that significantly reduces the systematic uncertainty on the efficiency scale factors. The production of high-statistics MC samples can reduce the uncertainty due to the limited sample statistics. Instead of applying the b tagging cut on the W+light-flavour, $W + c$, and $W + c\bar{c}$ samples, the probability of light- and c-flavour jets to be wrongly tagged as b jets ("fake factorisation") can be evaluated and used to prevent the poor MC statistics of these background components after all selection cuts. Besides these experimental efforts,

the study of new Monte-Carlo samples for the signal and background processes produced by recent NLO Monte-Carlo generators is ongoing to get a better theoretical description of these processes. Furthermore, alternatives and modifications to the cut-based analysis approach, such as multivariate analysis techniques or jet substructure techniques can be introduced in the $WH \to l\nu b\bar{b}$ Higgs boson channel.
When combining the Higgs boson production channels WH, ZH, and $t\bar{t}H$, these efforts will bring the study of the (possible) $H \to b\bar{b}$ decay of the discovered Higgs-like particle within reach.

A. Fraction Fit

The fraction fits performed in Section 4 and 5 use the ROOT TFractionFitter method [23] based on [60]. It suggests a method for fitting several binned distributions of finite MC samples to a binned data distribution. Only the main aspects are outline here.
Given is a histogram with n bins. The variable d_i is the number of data events in bin i. The variable f_i is the expected number of MC events, where a_{ji} events originate from the MC sample j. The total number of data events (MC events from sample j) is denoted by N_D (N_j). Then:

$$f_i = N_D \sum_j \frac{F_j a_{ji}}{N_j}, \tag{A.1}$$

with F_j being the fraction of the normalized sample j contributing to f_i for all bins n. F_j is the quantity determined in the fraction fit.
The probability relation between the expected number of events f_i and the number of data events d_i in bin i is described by a Poisson distribution, taking into account bins with a very small value of d_i.

$$P(d_i) = e^{-f_i} \frac{f_i^{d_i}}{d_i!} \tag{A.2}$$

An estimate for the fractions F_j is retrieved by maximising the total likelihood, i.e. the Poisson probabilities summed over all bins. Often it is more practical to maximize its logarithm:

$$\ln \mathcal{L} = \sum_{i=1}^{n} d_i \ln f_i - f_i \tag{A.3}$$

This typical fitting technique is denoted as "binned maximum likelihood" fit. Unfortunately, this fit accounts for the finite statistics of the data sample but ignores the finite size of the MC samples. This issue can be solved by replacing a_{ji} in Equation (A.1) by A_{ji}:

$$f_i = N_D \sum_j \frac{F_j A_{ji}}{N_j}, \tag{A.4}$$

where A_{ji} represents a Poisson distribution with outcome a_{ji}:

$$P(a_{ji}) = e^{-A_{ji}} \frac{A_{ji}^{a_{ji}}}{a_{ji}!} \tag{A.5}$$

Equation (A.5) is valid as long as the number of events per bin a_{ji} is small compared to the total number of events N_j. By incorporating the statistical uncertainties due to the limited size of the MC samples into the maximum likelihood approach using Equation A.5, a modified likelihood has to be maximised:

$$\ln \mathcal{L} = \sum_{i=1}^{n} d_i \ \ln f_i - f_i + \sum_{i=1}^{n} \sum_{j=1}^{m} a_{ji} \ \ln A_{ji} - A_{ji} \tag{A.6}$$

The solution of (A.6) conserves the normalisation of the fractions F_j:

$$\sum_{i=j}^{m} F_j = 1 \tag{A.7}$$

Bibliography

[1] ATLAS Collaboration, *Observation of a new particle in the search for the Standard Model Higgs boson with the ATLAS detector at the LHC*, Physics Letters B 716 (2012) 1-29.

[2] The CMS Collaboration, *Observation of a new boson at a mass of 125 GeV with the CMS experiment at the LHC*, Physics Letters B 716 (2012) 30-61.

[3] F. Englert, R. Brout, *BROKEN SYMMETRY AND THE MASS OF GAUGE VECTOR MESONS**, Phys. Rev. Lett. 13, 321-323 (1964).

[4] P. W. Higgs, *BROKEN SYMMETRIES AND THE MASSES OF GAUGE BOSONS*, Phys. Rev. Lett. 13, 508-509 (1964).

[5] G. S. Guralnik, C. R. Hagen, T. W. B. Kibble, *GLOBAL CONSERVATION LAWS AND MASSLESS PARTICLES**, Phys. Rev. Lett. 13, 585-587 (1964).

[6] D. Griffiths, *Introduction to Elementary Particles*. John Wiley & Sons, Second, Revised Edition, 2008

[7] L. D. Landau, J. M. Lifschitz, *Lehrbuch der theoretischen Physik I - Mechanik*, Akademie-Verlag Berlin (1987).

[8] T. Sjostrand, S. Mrenna, P. Skands, *PYTHIA 6.4 Physics and Manual*, arXiv:hep-ph/0603175, JHEP 0605:026 (2006).

[9] J. Gunion, H. E. Haber, G. Kane, S. Dawson, *The Higgs Hunter's Guide*, Perseus Books, 1990.

[10] J. Beringer et al. (Particle Data Group), *HIGGS BOSONS: THEORY AND SEARCHES*, http://pdg.lbl.gov, PR D86, 010001 (2012).

[11] The CDF Collaboration, the D0 Collaboration, the Tevatron New Physics, Higgs Working Group, *Updated Combination of CDF and D0 Searches for Standard Model Higgs Boson Production with up to 10.0 fb-1 of Data*, arXiv:1207.0449 [hep-ex] (2012).

[12] ATLAS Collaboration, *Search for the Standard Model Higgs boson produced in association with a vector boson and decaying to a b-quark pair with the ATLAS detector at the LHC*, ATLAS-CONF-2011-103 (2011).

[13] ATLAS Collaboration, *Search for the Standard Model Higgs boson produced in association with a vector boson and decaying to a b-quark pair with the ATLAS detector*, arXiv:1207.0210v1 [hep-ex] (2012).

[14] LHC Higgs Cross Section Working Group S. Dittmaier, C. Mariotti, G. Passarino, R. Tanaka (Eds.), *Handbook of LHC Higgs cross sections: 1. Inclusive observables*, CERN-2011-002 (CERN, Geneva, 2011) , arXiv:1101.0593 [hep-ph].

[15] *European Organization for Nuclear Research CERN*, http://public.web.cern.ch/public/, 18.09.2012.

[16] *DELPHI Experiment*, http://delphiwww.cern.ch/Welcome.html, 18.09.2012.

[17] L. Evans, P. Bryant (editors), *LHC Machine*, JINST 3 (2008).

[18] ATLAS Collaboration, *Luminosity Determination in pp Collisions at* $\sqrt{s} = 7$ *TeV Using the ATLAS Detector at the LHC*, arXiv:1101.2185v1 [hep-ex], Eur. Phys. J. C 71 (2011) 1630.

[19] ATLAS Collaboration, *Luminosity Public Results*, https://twiki.cern.ch/twiki/bin/view/AtlasPublic/LuminosityPublicResults, 14.09.2012.

[20] ATLAS Collaboration, *ATLAS Stand-Alone Event Displays*, https://twiki.cern.ch/twiki/bin/view/AtlasPublic/EventDisplayStandAlone/, 14.09.2012.

[21] D. Perkins, *Hochenergiephysik*, Addison-Wesley (1990).

[22] ATLAS Collaboration, *ATLAS Experiment at the CERN Large Hadron Collider*, JINST 3 (2008).

[23] R. Brun, F. Rademakers, *ROOT - An Object-Oriented Data Analysis Framework*, Nucl.Instrum.Meth. A389 (1997) 81-86

[24] ATLAS Collaboration, *ATLAS Computing - Technical Design Report*, ATLAS TDR–017, CERN-LHCC-2005-022 (2005).

[25] S. Weinzierl, *Introduction to Monte Carlo methods*, arXiv:hep-ph/0006269 (2000).

[26] S. Agostinelli et al., *Geant4: A simulation toolkit*, Nucl. Instrum. Meth. A506:250-303 (2003).

[27] J. M. Butterworth, J. R. Forshaw, M. H. Seymour, *Multiparton Interactions in Photoproduction at HERA*, Z.Phys.C72:637-646 (1996).

[28] ATLAS Collaboration, *Expected performance of the ATLAS experiment : detector, trigger and physics*, CERN-OPEN-2008-020.

[29] ATLAS Collaboration, *Muon reconstruction efficiency in reprocessed 2010 LHC proton-proton collision data recorded with the ATLAS detector*, ATLAS-CONF-2011-063 (2011).

[30] ATLAS Collaboration, *ATLAS Muon Combined Performance: Guidelines for Analyses of 2011 Data in Release 17*, `https://twiki.cern.ch/twiki/bin/viewauth/AtlasProtected/MCPAnalysisGuidelinesRel17MC11a`, 18.04.2012 (ATLAS internal documentation).

[31] ATLAS Collaboration, *Expected electron performance in the ATLAS experiment*, ATLAS-PHYS-PUB-2011-006 (2011).

[32] ATLAS Collaboration, *Electron IsEMIdentification*, `https://twiki.cern.ch/twiki/bin/viewauth/AtlasProtected/IsEMIdentification`, 15.09.2012 (ATLAS internal documentation).

[33] M. Cacciari, G. P. Salam, G. Soyez, *The anti-kt jet clustering algorithm*, JHEP 04 (2008) 063.

[34] ATLAS Collaboration, *Measurement of inclusive jet and dijet cross sections in proton-proton collisions at 7 TeV centre-of-mass energy with the ATLAS detector*, Eur. Phys. J. C 71 (2011) 1512,arXiv:1009.5908 [hep-ex].

[35] ATLAS Collaboration, *Jet energy measurement with the ATLAS detector in proton-proton collisions at* $\sqrt{7} = 7$ *TeV*, CERN-PH-EP-2011-191.

[36] ATLAS Collaboration, *Pile-up jet energy scale corrections using the jet-vertex fraction method*, ATL-PHYS-INT-2009-090 (ATLAS internal documentation).

[37] ATLAS Collaboration, *Performance of missing transverse momentum reconstruction in proton-proton collisions at 7 TeV with ATLAS*, Eur.Phys.J.C 72 (2012) 1844.

[38] ATLAS Collaboration, *Recommendations for the 2011 Muon Trigger*, `https://twiki.cern.ch/twiki/bin/viewauth/Atlas/MuonTriggerPhysicsTriggerRecommendations2011`, 10.07.2012 (ATLAS internal documentation).

[39] ATLAS Collaboration, *Recommendations for the 2011 Egamma Trigger*, `https://twiki.cern.ch/twiki/bin/viewauth/Atlas/TrigEgammaRecommendedTriggers2011`, 10.07.2012 (ATLAS internal documentation).

[40] ATLAS Collaboration, *Measurement of the b-tag Efficiency in a Sample of Jets Containing Muons with* 5 fb^{-1} *of Data from the ATLAS Detector*, ATLAS-CONF-2012-043 (2012).

[41] ATLAS Collaboration, *Commissioning of the ATLAS high-performance b-tagging algorithms in the* $\sqrt{s} = 7$ *TeV collision data*, ATLAS-CONF-2011-102 (2011).

[42] ATLAS Collaboration, *ATLAS Pileup Reweighting Tool*, `https://twiki.cern.ch/twiki/bin/viewauth/AtlasProtected/ExtendedPileupReweighting`, 02.07.2012 (ATLAS internal documentation).

[43] ATLAS Collaboration, *Good Run Lists for Analysis*, `https://twiki.cern.ch/twiki/bin/viewauth/AtlasProtected/GoodRunListsForAnalysis`, 15.09.2012 (ATLAS internal documentation).

[44] ATLAS Collaboration, *Performance of the ATLAS muon trigger in 2011*, ATLAS-CONF-2012-099 (2012).

[45] ATLAS Collaboration, *Measurement of muon momentum resolution of the ATLAS detector*, ATL-PHYS-PROC-2012-013 (2012).

[46] ATLAS Collaboration, *Combined Muon Performance Public Results*, `https://twiki.cern.ch/twiki/bin/view/AtlasPublic/MuonPerformancePublicPlots`, 14.08.2012.

[47] ATLAS Collaboration, *Electron performance measurements with the ATLAS detector using the 2010 LHC proton-proton collision data*, Eur. Phys. J. C72 (2012) 1909.

[48] ATLAS Collaboration, *Performance of the ATLAS Electron and Photon Trigger in p-p Collisions at* $\sqrt{7} = 7$ *TeV in 2011*, ATLAS-CONF-2012-048 (2012).

[49] ATLAS Collaboration, *Electron/Gamma Public Results*, `https://twiki.cern.ch/twiki/bin/view/AtlasPublic/ElectronGammaPublicCollisionResults`, 14.08.2012.

[50] M. L. Mangano, M. Moretti, F. Piccinini, R. Pittau, A. D. Polosa, *ALPGEN, a generator for hard multiparton processes in hadronic collisions*, arXiv:hep-ph/0206293v2, JHEP 0307 (2003) 001.

[51] ATLAS Collaboration, *Heavy Flavor Overlap Removal Tool*, `https://twiki.cern.ch/twiki/bin/viewauth/AtlasProtected/HforTool`, 16.07.2012 (ATLAS internal documentation).

[52] F. Febres Cordero, L. Reina, D. Wackeroth, *W- and Z-boson production with a massive bottom-quark pair at the Large Hadron Collider*, arXiv:0906.1923v3 [hep-ph], Phys.Rev.D80:034015 (2009).

[53] G. Corcella, I. G. Knowles, G. Marchesini, S. Moretti, K. Odagiri, P. Richardson, M. H. Seymour, B. R. Webber, *HERWIG 6.5: an event generator for Hadron Emission Reactions With Interfering Gluons (including supersymmetric processes)*, arXiv:hep-ph/0011363v3, JHEP 0101:010 (2001).

[54] S. Frixione, F. Stoeckli, P. Torrielli, B. R. Webber, C. D. White, *The MC@NLO 4.0 Event Generator*, arXiv:1010.0819v1 [hep-ph].

[55] B. P. Kersevan, E. Richter-Was, *The Monte Carlo Event Generator AcerMC 2.0 with Interfaces to PYTHIA 6.2 and HERWIG 6.5*, arXiv:hep-ph/0405247v2 (2012).

[56] ATLAS Collaboration, *Top group's MC11 Samples For 2011 Data Analyses*, `https://twiki.cern.ch/twiki/bin/viewauth/AtlasProtected/TopMC11`, 16.07.2012 (ATLAS internal documentation).

[57] ATLAS Collaboration, *Single Boson and Diboson Production Cross Sections in pp Collisions at* $\sqrt{s} = 7$ *TeV*, ATL-COM-PHYS-2010-695 (2010) (ATLAS internal documentation).

[58] ATLAS Collaboration, *Atlas Production Group*, `https://twiki.cern.ch/twiki/bin/viewauth/AtlasProtected/AtlasProductionGroup`, 17.07.2012 (ATLAS internal documentation).

[59] ATLAS Collaboration, *A data-driven method to estimate the QCD contribution in the cross-section measurement of the* $W \to \mu\nu_\mu$ *production in association with jets*, ATL-COM-PHYS-2011-298 (2011) (ATLAS internal documentation).

[60] R. Barlow, C. Beeston, *Fitting using finite Monte Carlo samples*, Computer Physics Communications77 (1993) 219-228.

[61] ATLAS Collaboration, *Jet Energy Resolution and Selection Efficiency Relative to Track Jets from In-situ Techniques with the ATLAS Detector Using Proton-Proton Collisions at a Center of Mass Energy* $\sqrt{7} = 7$ *TeV*, ATLAS-CONF-2010-054 (2010).

[62] ATLAS Collaboration, *ATLAS Jet/*$\not{E}_T$ *working group: Preliminary and Final Results from Collision Data*, `https://twiki.cern.ch/twiki/bin/view/AtlasPublic/JetEtMissPublicCollisionResults`, 14.08.2012.

[63] ATLAS Collaboration, *Measurement of the production cross section for Z/gamma* in association with jets in pp collisions at* $\sqrt{s} = 7$ *TeV with the ATLAS detector*, arXiv:1111.2690v1 [hep-ex] (2011), Phys. Rev. D85 (2012) 032009.

[64] ATLAS Collaboration, *Measurement of the WW cross section in $\sqrt{s} = 7$ TeV pp collisions with the ATLAS detector and limits on anomalous gauge couplings*, arXiv:1203.6232v2 [hep-ex] (2012), Phys. Lett. B712 (2012) 289-308.

[65] ATLAS Collaboration, *Measurement of WZ production in proton-proton collisions at $\sqrt{s} = 7$ TeV with the ATLAS detector*, arXiv:1208.1390v2 [hep-ex] (2012).

[66] ATLAS Collaboration, *Search for the Standard Model Higgs boson produced in association with a vector boson and decaying to a b-quark pair using up to 4.7 fb^{-1} of pp collision data at $\sqrt{7} = 7$ TeV with the ATLAS detector at the LHC*, ATLAS-COM-PHYS-2011-1648 (2012) (ATLAS internal documentation).

[67] G. Cowan, K. Cranmer, E. Gross, O. Vitells, *Asymptotic formulae for likelihood-based tests of new physics*, arXiv:1007.1727v2 [physics.data-an] (2010), Eur.Phys.J.C71:1554,2011.

[68] A. L. Read, *Modified frequentist analysis of search results (the CL_s method)*, CERN-OPEN-2000-205 (2000).

[69] L. Moneta, K. Belasco, K. Cranmer, S. Kreiss, A. Lazzaro, D. Piparo, G. Schott, W. Verkerke, M. Wolf, *The RooStats Project*, arXiv:1009.1003v2 [physics.data-an] (2010).